Experimental Aspects of Quantum Criticality in the Quantum Hall Regime

Promotiecommissie

Promotor:	Prof. dr. A.M.M. Pruisken
Co-promotor:	Dr. A.de Visser
Overige leden:	Dr. M.A. Baranov
	Prof. dr. M.S. Golden
	Prof. dr. T. Gregorkiewicz
	Dr. P.M. Koenraad
	Prof. dr. V.A. Kulbachinskii
	Prof. dr. J.C. Maan

Cover
front: dilution refrigerator (WZI, room K.85)
back: find your own way to recovery; puzzle for first year PhD students (WZI, room K.82)

ISBN 90-5776-144-0

The work described in this thesis was carried out at the Van der Waals-Zeeman Institute of the University of Amsterdam, Valckenierstraat 65, 1018 XE Amsterdam, The Netherlands.
The work is part of the research program of the Foundation for Fundamental Research on Matter [Stichting voor Fundamenteel Onderzoek der Materie (FOM)] and was made possible by financial support from the Netherlands Organization for Scientific Research [Nederlandse Organisatie voor Wetenschappelijk Onderzoek (NWO)].
A digital version of this thesis can be downloaded from
`http://www.science.uva.nl/research/wzi/cmp/devisser`

Experimental Aspects of Quantum Criticality in the Quantum Hall Regime

ACADEMISCH PROEFSCHRIFT

TER VERKRIJGING VAN DE GRAAD VAN DOCTOR
AAN DE UNIVERSITEIT VAN AMSTERDAM
OP GEZAG VAN DE RECTOR MAGNIFICUS
PROF. MR. P.F. VAN DER HEIJDEN
TEN OVERSTAAN VAN EEN DOOR HET COLLEGE VOOR PROMOTIES
INGESTELDE COMMISSIE, IN HET OPENBAAR TE VERDEDIGEN
IN DE AULA DER UNIVERSITEIT
OP DONDERDAG 22 SEPTEMBER 2005, TE 14.00 UUR

DOOR

Leonid Alexandrovich Ponomarenko

geboren te Lviv (Oekraine)

Promotor: Prof. dr. A. M. M. Pruisken
Co-promotor: Dr. A. de Visser

Faculteit der Natuurwetenschappen, Wiskunde en Informatica

in memory of my father

Contents

1

INTRODUCTION

1.1. The quantum Hall effect

The quantum Hall effect (QHE) was discovered by von Klitzing *et al.* [1] now 25 years ago. It is a macroscopic quantum phenomenon, which takes place in a two-dimensional electron or hole system exposed to a strong perpendicular magnetic field at low temperatures ($T \lesssim 1$ K). Under these conditions, the Hall (transverse) resistance R_H is quantized and exhibits plateaus at the values:

$$R_H = \frac{h}{i\,e^2} \approx \frac{25.8128}{i}\ \mathrm{k}\Omega, \tag{1.1}$$

where i is an integer, h is Planck's constant, and e is the charge of the electron. A striking observation is the accuracy of the quantization (better than one part in ten million), and its independence on the geometrical details of the sample, the type of material used to make the two-dimensional system *etc*. Each plateau in the Hall resistance is accompanied by a region of vanishing longitudinal resistance as shown in Fig. 1.1.

The QHE is regarded as one of the most prominent discoveries in solid state physics in the twentieth century. It gives direct access to quantum phenomena by measuring a macroscopic quantity - electrical resistance. For this discovery, Klaus von Klitzing was awarded the Nobel prize in physics in 1985. This was in part due to the importance of the QHE in metrology: in 1988 the International Committee for Weights and Measures (CIPM) adopted the value of the transverse resistance in the quantum Hall effect as a new reference standard of resistance [2].

A variety of models have been proposed to explain the quantized be-

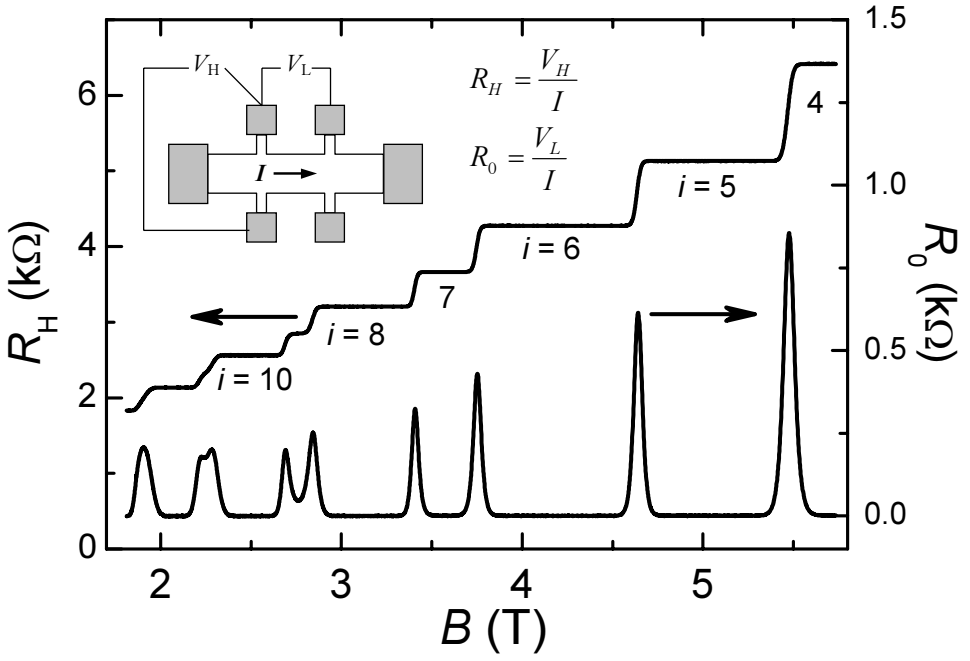

Figure 1.1: An example of the quantum Hall effect measured on a sample with Hall bar geometry. The Hall resistance R_H as a function of the magnetic field B displays a sequence of plateaus with indices i in the range between 4 and 12 as indicated. Plateaus in R_H are accompanied by regions of vanishing longitudinal resistance R_0 (sample used: #659, GaAs/AlGaAs quantum well, $T \approx 60$ mK).

havior of the Hall resistance. The most popular among these are the Landauer-Buttiker edge states picture [3], the gauge invariance approach proposed by Laughlin [4] and the explanation based on the Kubo formula [5] developed by Aoki and Ando [6].

Among the necessary requirements for observation of the QHE are two-dimensionality of the electron system (in the following we will refer to electrons rather than holes as charge carriers) and the presence of disorder. At zero magnetic field, the electrons can be considered as a gas of free particles confined to two dimensions. For such a system the density of states (DOS) is:

$$N(E) = \frac{m^*}{\pi\hbar^2} \quad , \tag{1.2}$$

where m^* is the effective mass of the electron. States are occupied up to the Fermi energy E_F:

$$E_F = \frac{\pi n_e h}{m^*} \quad , \tag{1.3}$$

where n_e is the electron density of the 2DEG. The Fermi energy determines the temperature scale of the problem $T \sim E_F/k_B$ (k_B is Boltzmann's constant). For a typical value $n_e = 2 \times 10^{11}$ cm^{-2} and an effective electron mass $m^* = 0.067m_e$ (value for bulk GaAs, m_e is the free electron mass), the Fermi energy E_F according to Eq. (1.3) is of the order of 0.06 meV or $T = E_F/k_B \sim 80$ K. To study the quantum Hall transitions experimentally, the working temperature should be much lower than this estimated value. Therefore, cryogenic equipment necessarily forms an essential part of the experimental setup for studying the QHE.

In a strong magnetic field the DOS function of the 2DEG transforms into a discrete set of highly degenerate Landau levels with energies [7]:

$$E_{n,s} = (n + \frac{1}{2})\hbar\omega_c + m_s g^* \mu_B B, \quad n = 0, 1, 2, ..., \tag{1.4}$$

where $m_s = \pm\frac{1}{2}$ is the spin quantum number, μ_B is the Bohr magneton, g^* is the effective g-factor and ω_c is the cyclotron frequency:

$$\omega_c = \frac{eB}{m^* c} \ , \tag{1.5}$$

These equations show, that the energy of the Landau levels is proportional to the applied magnetic field B. By changing B one can control the number of occupied Landau levels (*i.e.* the Landau levels below the Fermi energy). The transitions between the plateaus in the Hall resistance and the peaks in the longitudinal resistance (see Fig. 1.1) take place when the centers of Landau levels cross the Fermi surface.

The number of occupied Landau levels is called the filling factor ν. If the highest Landau level is only partially filled, the filling factor attains non-integer values. With the Fermi level at the center of a Landau level the filling factor is half-integer. Therefore, in a somewhat simplified picture of the QHE[1], the transitions between plateaus take place at $\nu = \frac{3}{2}, \frac{5}{2}, \frac{7}{2}$ *etc*. A special case is $\nu = \frac{1}{2}$, where the 2DEG, instead of undergoing a transition between two plateaus, becomes an insulator, as described in Section 1.3.

It can be shown (see [7] or any other textbook on QHE), that the magnetic field B is related to the filling factor ν as:

$$\nu = \frac{hn_e}{eB} \ . \tag{1.6}$$

The filling factor is a very important parameter and, in fact, has a more fundamental meaning in the theory of the QHE than the magnetic field.

[1] Without overlap of Landau levels

At the plateaus not only the longitudinal resistivity $\rho_{xx} = \frac{W}{L} R_0$ (where W is the width of the Hall bar and L the distance between the potential contacts), but also the longitudinal conductivity σ_{xx} is zero:

$$\rho_{xx} = \sigma_{xx} = 0. \tag{1.7}$$

This unusual and surprising behavior follows from the equations for inverting the resistivity tensor to the conductivity tensor:

$$\sigma_{xx} = \frac{\rho_{xx}}{\rho_{xx}^2 + \rho_{xy}^2}, \quad \sigma_{xy} = \frac{\rho_{xy}}{\rho_{xx}^2 + \rho_{xy}^2} \ . \tag{1.8}$$

With $\rho_{xx} = 0$ and $\rho_{xy} \neq 0$, we immediately arrive at $\sigma_{xx} = 0$. The simultaneous disappearing of conductivity and resistivity has led to confusing terminology. The quantum Hall state is often referred to as "insulator" meaning that $\sigma_{xx} = 0$, although the current flows in the sample without dissipation.

1.2. Scaling in the quantum Hall effect

The rich physics of the QHE goes significantly further than exact quantization of the Hall resistance and dissipationless flow of the electrical current. The QHE is also an excellent playground for studying quantum phase transitions.

By definition, a quantum phase transition (QPT) takes place at $T = 0$ under change of some external control parameter (such as pressure, magnetic field, doping concentration *etc*). Compared to a classical phase transition, which take place at a finite temperature and is governed by thermal fluctuations, the critical fluctuations in the QPT are of quantum origin and therefore exist even at $T = 0$.

In case of the quantum Hall effect, the control parameter is the magnetic field. It has been realized shortly after the discovery of the QHE that the transitions between adjacent plateaus become extremely narrow upon decreasing the temperature [8]. Therefore, it was natural to assume that in the limit $T \to 0$ the transitions between the plateaus became infinitely sharp, *i.e.* represent a sequence of QPT's at the critical fields $B_{c,i}$. Although the experimental papers which addressed this problem in the last 15 years often gave rise to lively disputes, the dominant point of view in the quantum Hall community at the moment is that the transitions between plateaus are indeed examples of QPT.

A simple relation between the magnetic field B and the filling factor ν given by Eq.(1.6), allows one to consider ν as a control parameter as well (with corresponding critical values $\nu_{c,i}$).

The concept of scaling implies a data collapse near the critical point, achieved by rescaling the axes of the original data plots in an appropriate way [9]. This is a rather general concept, applicable to a wide range of critical phenomena. In many cases, scaling presents merely a phenomenological law deduced from the experiment. The renormalization group theory, however, provides a solid foundation for understanding scaling. More specifically, for the QHE, scaling implies [10] that the components of the conductivity tensor, σ_{xx} and σ_{xy}, which are functions of both the magnetic field and temperature, are in fact functions of a single scaling variable X:

$$X = \frac{\nu - \nu_{c,i}}{(T/T_0)^{\kappa}}, \tag{1.9}$$

where κ is the (transport) critical exponent and T_0 is a phenomenological temperature, which depends, in general, on the Landau level index. This results in a power-law temperature dependence of quantities extracted from the transport data. For instance, the width $\Delta\nu$ of the peak in the $\rho_{xx}(\nu)$ dependence and the maximum slope of the Hall resistance $d\rho_{xy}/d\nu$ should both obey power-law T-dependence:

$$\Delta\nu \propto \left(\frac{d\rho_{xy}}{d\nu}\right)_{max} \propto T^{\kappa}, \tag{1.10}$$

The scaling theory of the QHE is based on the renormalization group approach and has been developed by Pruisken [10, 11, 12, 13]. Although the theory does not give the numerical value for κ, it states that the critical exponent should be universal in a sense that it does not depend on the Landau level index. Values for κ have been obtained by means of numerical calculations in various models. A brief overview of relevant results is given in Section 3.2

The first experimental evidence of scaling behavior in the QHE was reported by Wei *et al.* [14]. Despite the large amount of experimental data obtained by various groups and more than 15 years of history of the subject, consensus about the exact value of the critical exponent κ and its universality is still lacking at present.

The primary goal of this thesis is to investigate scaling behavior in the quantum Hall effect. It is important to realize, that the numerical value of κ is not just a number, which characterizes a certain type of semiconductor structure. In fact, κ has a fundamental meaning. In the renormalization group theory,

systems with the same set of critical exponents and scaling functions are said to belong to the same universality class [15]. The usefulness of this concept lies in the fact that, in general, members of a universality class have only three things in common: the symmetry group of the Hamiltonian, the dimensionality, and whether or not the forces are short-ranged [16]. Strictly speaking, this is true for classical phase transitions. The question whether it can be applied to the quantum case or not, is still under debate. Nevertheless, since the numerical value of the critical exponent depends on such a fundamental property like the symmetry of the Hamiltonian, measuring κ provides a very important tool for testing different theoretical models (at least if these are developed deep enough to give an estimate for κ).

1.3. The plateau-insulator transition

The plateau-insulator (PI) transition terminates the sequence of plateau-plateau (PP) transitions in high magnetic field. Although the experimental manifestation of the PI transition is absolutely different from the transitions between adjacent plateaus, the underlying physics, at least from the theoretical point of view, in both cases is very much the same.

An example of the PI transition, as measured on an InGaAs/InP heterostructure, is shown in Fig. 1.2. The distinguishing feature of the PI transition is a temperature independent crossing point in the $\rho_{xx}(B)$ data, which defines the critical field B_c. Below the critical field the longitudinal resistance decreases with decreasing temperature, so the temperature dependence of ρ_{xx} is metallic like. In contrast, above B_c the 2DEG behaves like an insulator, *i.e.* the resistance increases with decreasing T.

Both the PP and PI transition are the result of a Landau level crossing the Fermi energy upon increasing the magnetic field. The crucial difference between the two types of transitions is that at the PI transition the *lowest* Landau level crosses the Fermi energy. In this case, at $B > B_c$ all states below the Fermi level are localized (in the $T \to 0$ limit) and cannot contribute to the electrical current. In contrast, at the PP transition there are always one or more Landau levels below E_F which are able to carry the current.

The study of PI transitions requires in general substantially stronger magnetic fields than for the investigation of the PP transitions. The PI transition takes place at a filling factor $\nu = \frac{1}{2}$, while the closest PP transition occurs at $\nu = \frac{3}{2}$. Since the magnetic field is inversely proportional to the filling factor (see

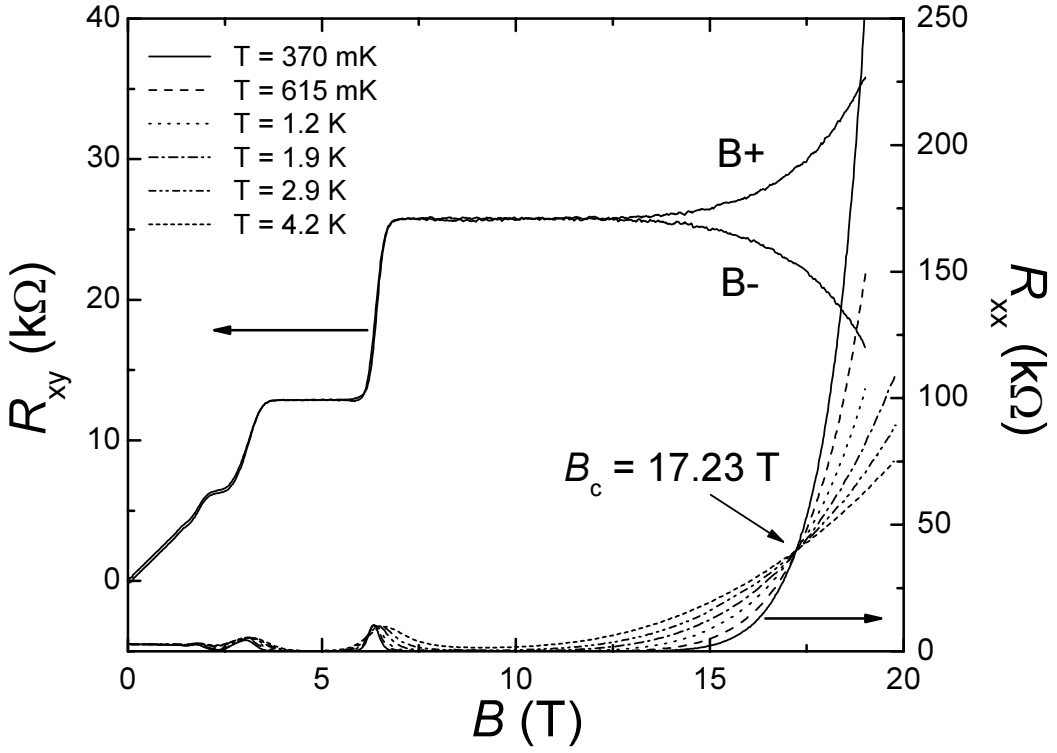

Figure 1.2: An example of the plateau-insulator transition ($B_c = 17.2$ T) in an InGaAs/InP hetorostructure [17]. The crossing point observed for the longitudinal resistance (right axis) gives the location of the critical point B_c. On this scale the nearest PP transition is observed as the small peak near 7 T. Two curves R_{xy}(B) (left axis) denoted by $B+$ and $B-$ represent the Hall resistances measured for both polarities of the magnetic field at $T = 1.2$ K. The Hall resistance stays quantized through the PI transition, however, due to contact misalignment averaging over both field polarities is needed to prove the quantization.

Eq. (1.6)), the PI transition takes place at a magnetic field about 3 times larger than the field for the highest PP transition. This often renders experiments on the PI transition difficult to realize, especially for samples with a high carrier concentration.

Although the first experiment on the PI transition was reported in 1984 [18], our knowledge of this phenomenon is still far from complete. The main problem here, from our point of view, is the lack of high quality samples with low carrier concentration. Nevertheless, the available data show that the transport properties of the 2DEG at the PI transition fit much better into the framework of existing theoretical and numerical results, than the data for the PP transitions. As an example of a good match between theory and experiment

as regard the PI transition, we mention the semicircle in the $\sigma_{xx}(\sigma_{xy})$ plane [19]. Coincidence of the measured values of the components of the conductivity tensor $\sigma_{xx} = \sigma_{xy} = e^2/(2h)$ at the critical field B_c with the results of numerical simulations of Ref. [20] is another example of such a matching.

From the perspective of this thesis, the most important property of the PI transition is its *quantum critical behavior* in a broad temperature range, with a well defined (and possibly universal) scaling exponent κ, as predicted by the renormalization group analysis of the QHE [10].

As we shall show in this thesis, the reason for the perfect match between experiment and theory in the case of the PI transition, is its immunity to macroscopic inhomogeneities, which are inherently present in two-dimensional semiconductor structures. The PP transitions, in contrast, turn out to be very sensitive to inhomogeneities, which hamper the observation of true critical behavior.

1.4. Scope of this thesis

This thesis is organized as follows. In Chapter 2 we describe the experimental setups and techniques used for studying transport properties of the 2DEG in strong magnetic field. Much attention is payed to issues that are not properly described in textbooks, like the magnetoresistance of thermometers and AC measurements near a metal-insulator transition, where the resistance changes by a few orders of magnitude. Sample selection is also described in detail.

In Chapter 3, we introduce the main theoretical concepts used in this thesis. Besides the main results of the scaling theory of the QHE, we also cover (albeit on a rather simple level) topics like the flow diagram, universality class and strong localization. The last two sections of Chapter 3 are dedicated to a quantitative description of magnetotransport properties of quantum Hall systems.

In the next three chapters the experimental results are presented. In Chapter 4 we report our investigations of transport properties of the 2DEG at the transitions between adjacent plateaus (PP transitions). The main result here is the observation of reflection symmetry, which is a key for understanding the dramatic influence of macroscopic inhomogeneities on magnetotransport data taken in the quantum Hall regime.

The transition through the lowest Landau level from the quantum Hall to insulating state is the topic of Chapter 5. This plateau-insulator (PI) transi-

tion provides direct access to the critical behavior. The sample employed in this study is the same InGaAs/InP heterostructure as used in the pioneering and widely cited work [14] on scaling at the PP transitions. We extract a critical exponent $\kappa = 0.58$, which differs from the value $\kappa = 0.42$ reported in Ref. [14] for PP transitions. The difference is attributed to macroscopic sample inhomogeneities.

Further magnetotransport studies of the PI transition were carried out on an InGaAs/GaAs quantum well and are reported in Chapter 6. A nice feature of this sample is that the carrier density can be tuned in a convenient range by making use of persistent photoconductivity. In this way we are able to investigate universality of the critical exponent κ, for different carrier concentrations in one and the same structure.

Finally, in Chapter 7 we present the results of numerical simulations for the 4-point resistance in the quantum Hall case. Our simulations reveal a dramatic effect of carrier density gradients on the behavior of the PP transition. From this we conclude that in the presence of carrier density gradients only the PI transition can be used for the proper investigation of critical behavior.

2

EXPERIMENTAL

2.1. Introduction

The entire experimental work of this thesis is based on measuring the electrical resistivity, which is often referred to in the literature as "transport measurements". For those not involved in studying the quantum Hall effect, it may sound like an easy and trivial experiment. Indeed, even high school students are familiar with a multimeter, *i.e.* a small device with two probes able to measure resistance in a range between a few mΩ and tens of MΩ. If such a cheap instrument can measure resistance in an impressive range, covering more than six orders of magnitude, one can ask the question: What is the experimental challenge in measuring magnetotransport in the quantum Hall effect?

In this chapter we describe the experimental techniques and discuss most significant difficulties, which the experimentalist has to overcome in order to extract reliable data from the quantum Hall measurement. The most significant features of a typical quantum Hall experiment, which require great care and/or special instruments are the following:

• The quantum Hall effect takes place at low temperatures ($T \lesssim 4.2$ K), which evokes the need for sophisticated cooling machines and should preferably be studied at dilution refrigerator temperatures (5 mK - 1 K);

• In order to prevent Joule heating at subkelvin temperatures, the measuring current has to be quite small, in order of a few nA, which implies that only lock-in techniques allow one to measure the resistance with an acceptable signal-to-noise ratio;

• The study of the quantum Hall effect requires in general large magnetic fields, which are often not accessible with standard superconducting solenoids.

Therefore, a significant part of the experiments was carried out outside the van der Waals-Zeeman Institute (WZI), in dedicated laboratories capable of producing the strongest magnetic fields: the Nijmegen High Field Magnet Laboratory (NHFML, Netherlands) and the Grenoble High Magnetic Field Laboratory (GHMFL, France).

Special attention in this chapter is paid to thermometry at subkelvin temperatures in the presence of high magnetic fields. We also discuss the significance of out-of-phase control in quasi-DC transport measurements as an important indicator of data reliability, especially in experiments probing the plateau-insulator transition.

2.2. Brief description of experimental setups

A home-made ^{3}He insert with base temperature $T = 0.3$ K [21] was mainly used for test purposes and selection of samples. The principles of cooling with ^{3}He can be found in many low-temperature textbooks (see for example Ref. [22]). To provide magnetic fields necessary for observation of the quantum Hall effect, the ^{3}He system was used in combination with an 8 T superconducting magnet. The advantage of the ^{3}He system compared to more sophisticated and bulky dilution refrigerators is its relatively short cooling time to base temperature. The design of our ^{3}He insert allows changing of samples, while the cryostat and superconducting magnet stay at low temperatures. This makes the ^{3}He system a perfect tool for sample selection. However, the base temperature (0.3 K) is still relatively high. Extension of the low temperature limit to ~ 5 mK (at zero magnetic field) is possible with dilution refrigerators.

In the course of the preparation of this thesis four different dilution refrigerators were used. Again, we refer to dedicated literature [22, 23] for a description of the principles of operation and construction of dilution refrigerators. Here, we only point out the differences between the different setups. In Table 2.1 the main parameters of all refrigerators are listed, together with information about the magnets used. Three out of four refrigerators have a quite similar design, but are located in different laboratories, where they are used as low temperature inserts for dedicated high field magnets. The common feature of these fridges is a plastic mixing chamber. Since plastic is an insulating material, eddy current heating is absent. Therefore, magnetotransport measurements can be carried out with a higher field ramp rate than in the case of a metallic mixing chamber. Increasing the ramp rate reduces the total time of the

Laboratory (location)	Max. field, T (magnet type)	Refrigerator (manufacturer)	Base T, mK	Mixing chamber
NHFML (Nijmegen)	33 (Bitter)	Home made	70	plastic
GHMFL (Grenoble, France)	23 (Bitter)	Kelvinox (Oxford Instr.)	19	plastic
WZI (Amsterdam)	17 (SC)	Minikelvin (Leiden Cryog.)	< 50	plastic
WZI (Amsterdam)	9 (SC)	200S (Oxford Instr.)	< 20	metal

Table 2.1: Various magnets and dilution refrigerators used in the experiments reported in this thesis. The abbreviations for the laboratory names are explained in the text.

experiment, which is usually limited at national high field facilities.

The fourth refrigerator has a dilution unit made out of copper, but the mixing chamber is located above the superconducting magnet. In addition, the magnet is equipped with special compensation coils, which cancel the field around the mixing chamber to values below a few mT. The sample is placed in the center of the magnetic field at the end of an H-shaped bar made of pure copper, which provided the thermal coupling to the mixing chamber. Although the sweep rate is strongly restricted by eddy currents occurring in the H-bar, such a system has some advantage compared to plastic dilution refrigerators. The most significant one is the possibility to measure the correct temperature at high magnetic fields. With plastic fridges thermometry in field is much more difficult. The reason for this is the rather poor thermal conductivity of insulating materials out of from which the plastic mixing chamber is made. Therefore, the thermometer has to be mounted close to the sample, which means that both the sample and the thermometer are exposed to the magnetic field. Unfortunately, up to now, there is no commercially available thermometer with negligible magnetoresistance and suitable for subkelvin temperatures[1]. In Section 2.3 we will discuss this problem in detail. Here we only mention that a field compensated region around the mixing chamber allows us to solve the problem of

[1]Thermometers based on the coulomb blockade effect, called CBT sensors [24], show good performance below 1 K and at high magnetic field [25]. However, commercial temperature controllers working with CBT sensors are not available yet.

the magnetoresistance of the thermometers.

Another distinction between the different models of the plastic refrigerators is the location of the sample with respect to the mixing chamber. In the Nijmegen refrigerator (the first entry in Table 2.1) the sample support is located outside the dilution unit, while in the other models the samples are mounted inside the mixing chamber. The latter arrangement, at least in theory, provides better cooling since the sample is in direct contact with the cryogenic liquid. However, an extremely good coupling between the sample and mixture turns into a drawback above 1 K. Temperature regulation becomes a difficult task, since it requires evaporation of a substantial part of the mixture. On the other hand, if the sample is mounted outside the mixing chamber, it has to be thermally coupled to the mixture. Two thin silver strips were used for this purpose in Nijmegen. However, since silver is a good conductor, eddy currents become again an important issue. In the Nijmegen fridge they result in an increase of the base temperature by 20-30 mK at a ramp rate of 0.5 T/min.

Two different type of magnets were used for creating strong magnetic fields: superconducting (SC) and Bitter magnets. Both are properly described in numerous textbooks. The first type is commercially available and much cheaper to run. The highest field that such a magnet can offer is about 20 T. Bitter magnets can reach higher fields (33 T), however they require megawatts of power and a large-scale cooling system.

The resistance was measured by a low frequency AC method using several lock-in amplifiers (EG&G 7265) in combination with preamplifiers (EG&G 5186). The working frequency was between 0.5 and 13 Hz, depending on the sample resistance. For studying the insulating state the lowest frequencies were used (0.5-2 Hz). A detailed description of the measuring technique is given in Section 2.4.

In all setups, except the one in the GHMFL, the temperature was regulated by an ORPX-1 controller (Barras Provence) equipped with a multiplexer, which allows reading of up to 8 different thermometers. A mini-computer Epson PX-4 was used in combination with the ORPX-1 as display and input-output device. A dedicated Oxford Instruments Intelligent Temperature Controller (ITC), which was part of the Kelvinox system, was used for regulation of the temperature in the GHMFL. However, even there the ORPX-1 was used to monitor the temperature from an extra thermometer mounted next to the sample.

A personal computer (PC) with home written software was used for data

acquisition. The communication between instruments and PC was mainly accomplished via an IEEE 488 interface (also known as HPIB), except for the temperature controller, which was not equipped with this type of interface. Therefore, communication with the ORPX-1 was made through a rather slow RS-232 interface.

2.3. Subkelvin thermometry in high magnetic field

Thermometry at low temperatures is an important issue. In general, thermometers can be divided into primary and secondary ones. Primary thermometers do not require calibration and the temperature can be determined by measuring some physical parameter (pressure, magnetic susceptibility etc.), which has a well known theoretical dependence on T. Secondary thermometers require calibration against primary ones, but are more convenient to use. The best-known example of a secondary thermometer is the resistance thermometer. Commercial refrigerators usually are equipped with such thermometers calibrated at $B = 0$. However, primary and secondary thermometers offer not much choice, when it comes to measurements at high magnetic field. From this perspective a resistance thermometer based on a RuO_2 thick film is, perhaps, the only suitable sensor for magnetotransport measurements below 1 K. In this Section we describe the calibration of a RuO_2 thermometer in magnetic field up to 8.5 T. The same calibrated sensor was used in all dilution refrigerators as the main or as a spare thermometer. It allowed us to have a common reference and keep systematic errors due to magnetoresistance under control.

RuO_2 thick film resistors are prepared from RuO_2 grains mixed and fired with glass powder [26]. Thick film resistors are known for more than 20 years as thermometers suitable for measurement below 1 K [27]. The advantages of RuO_2 based sensors are: small size, high sensitivity, excellent reproducibility after hundreds of thermal cycles and, most important for our research, a relatively weak magnetic field dependence. Thick film RuO_2 resistors are commonly used in industry in the production of hybrid microcircuits. Therefore, many types of RuO_2 based resistors from different manufactures are available. In our case Dale resistors (type RCWP-575, with a room temperature value is 1.5 kOhm) were used. The details of the construction of Dale resistors can be found in Ref. [28].

We start with the calibration in zero magnetic field. In Fig. 2.1a we show the temperature dependence for two RuO_2 thick film resistors measured in the

Oxford 200S system. For historical reasons these particular sensors are called R3 and R4. The temperature was determined by a calibrated Lake Shore Ge thermometer (Model GR-200A-30, serial no. 22656). Each point in Fig. 2.1a is the result of averaging 50 readings taken by the ORPX-1 with a 10 sec interval, with at least 10 minutes stabilization after each change of temperature. The whole experiment was programmed and run overnight.

The temperature dependencies $R3(T)$ and $R4(T)$ have been used for calculating calibration functions. Due to the smooth and monotonic behavior of the data points a fourth-order polynomial fit on a double logarithm plot provides an accuracy better than 1 %. Although this precision is accurate enough for our practical use, it is worth looking at the data in Fig. 2.1 from a more general point of view.

The conductivity of RuO_2 based thick film resistors is believed to be due to variable range hoping (VRH) [29, 30], and at low enough temperatures we expect the resistance R to diverge according to:

$$R(T) = R_0 \exp\left(T_0/T\right)^{\alpha}, \tag{2.1}$$

where R_0 and T_0 are sample dependent parameters and α is determined by the dimensionality of the system and the structure of the density of states at the Fermi level [31]. For bulk material with a constant density of states α is $1/4$. Although this particular value of the parameter α has been reported several times in the literature [32, 33, 34], other values ranging between 0.14 and 0.71 were observed in experiment as well [29, 35, 36]. To prove $\alpha = 1/4$, authors usually plot $\log(R)$ vs $T^{-1/4}$, and thus the experimental data points should fall on a straight line. From our point of view this method is not very reliable. A more consistent method to extract α was used by authors who fitted the data to Eq. (2.1) using α, R_0 and T_0 as fit parameters. This method can be improved further. It is easy to derive from Eq. (2.1) that

$$\frac{d(\ln R)}{dT} = -\alpha \left(\frac{T}{T_0}\right)^{-\alpha-1}. \tag{2.2}$$

This formula has two advantages compared to the previous equation: it does not contain R_0 and it represents power law behavior. Therefore, if the experimental data are accurate enough to take the derivative $d \ln R/dT$ we should obtain a straight line on a double logarithmic plot $\frac{d(\ln R)}{dT}$ vs T. The slope of this line is given by $-1-\alpha$. Fig. 2.1b presents data plotted in this way. Numerical differentiation was made on the raw experimental data using the graphing

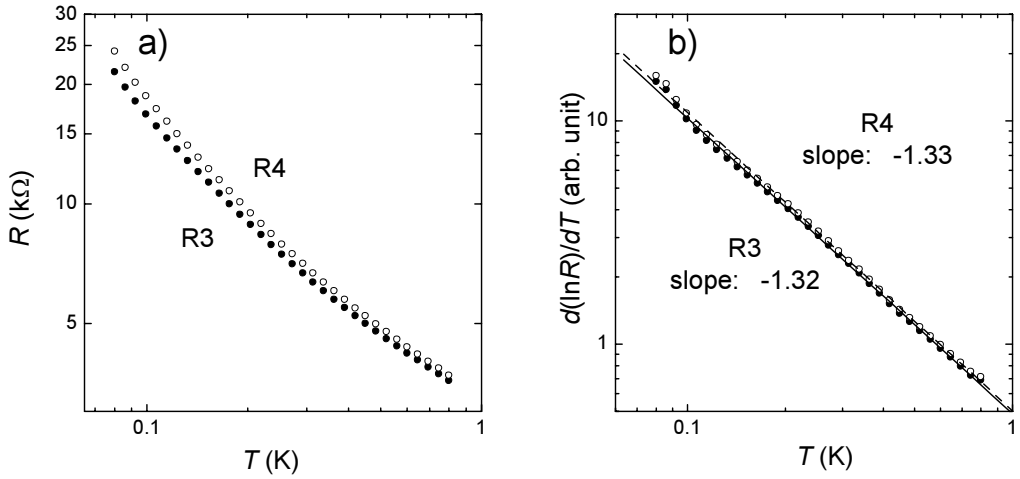

Figure 2.1: (a) The temperature dependencies of the resistance of RuO_2 thick film resistors (Dale, type RCWP-575) below 1 K. (b) $d \ln R/dT$ obtained from the sets shown in (a) plotted on a double logarithmic scale in order to verify the validity of Eq. (2.2).

package Origin 7. A linear behavior is obvious, suggesting $\alpha = 1/3$ for both data sets, which is significantly different from the value $1/4$ expected for bulk material and rather corresponds to VRH in two dimensions.

Now consider what happens at $B \neq 0$. As we already mentioned, RuO_2 sensors are rather insensitive to an external magnetic field. However, even for this type of thermometers the magnetoresistance is not negligible. The change of the apparent temperature due to an external field 8 T can be of the order of 7-8 % [37] and the sign of the magnetoresistance can be both positive [37] or negative [38] depending on the film composition. For studying critical phenomena such an uncertainty can have crucial consequences. The point is that the ordinary temperature controller cannot account for the magnetic field. It regulates the temperature in order to stabilize the resistance of the thermometer, but not the temperature itself. Therefore, any temperature dependence measured in high magnetic fields has systematic errors caused by the magnetoresistance of the sensor. A typical example is the temperature dependence of the width of the peak in the longitudinal magnetoresistance at plateau-plateau quantum Hall transitions. This width is used to extract the critical exponent for the PP transition, κ. Obviously, if the temperature is not measured properly, the extracted value of the critical exponent can be simply wrong.

Therefore, the magnetoresistance of our thermometers was investigated in a separate project in order to estimate the error in the extracted values of the

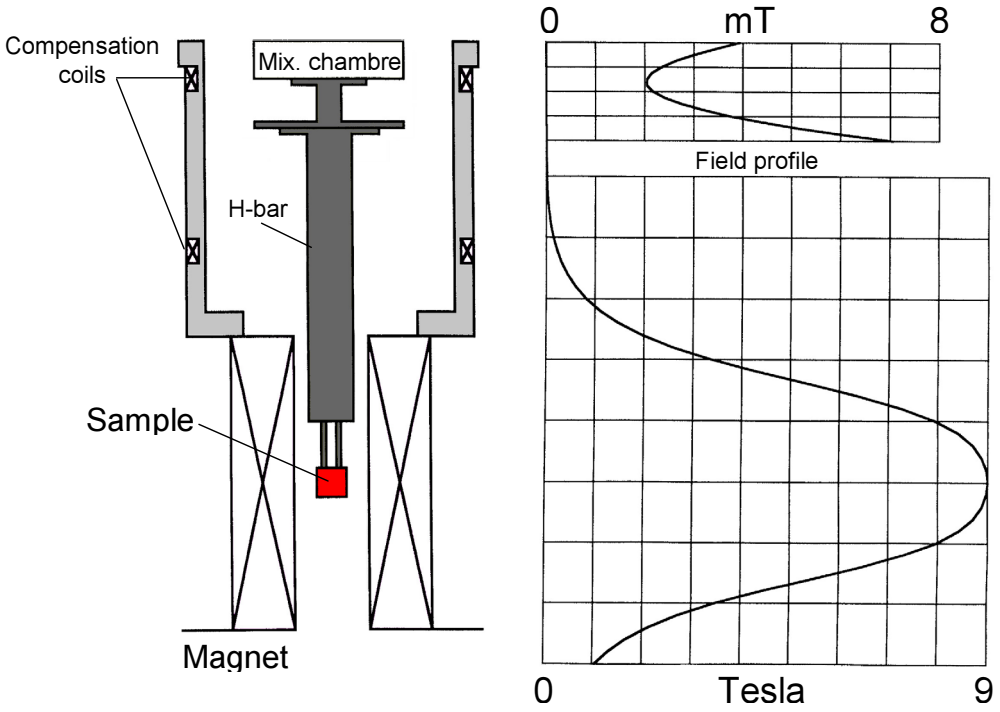

Figure 2.2: The arrangement of the magnet, mixing chamber and sample for the dilution refrigerator 200S (Oxford Instruments). The plot on the right side shows the field profile. Due to compensation coils the stray field around the mixing chamber does not exceed a few mT.

critical exponent due to the uncertainty in T. We have calibrated thermometer R3 at several values of the magnetic field using a dilution refrigerator with field compensated region (fridge #4 in Table 2.1). In Fig. 2.2 we schematically show the arrangement of the thermometers with respect to the mixing chamber and the sample. The magnetic field profile is shown too. The RuO_2 thermometer which requires calibration in magnetic field is mounted in the center of the field, next to the sample. The calibrated Ge thermometer was attached and thermally anchored to the mixing chamber. Therefore, the Ge thermometer was always at "zero" field. When taking data, the superconducting magnet was switched to persistent mode in order to exclude eddy current heating in the H-bar. For several fixed values of the magnetic field the temperature dependence $R3$ vs T was measured according to a preprogrammed procedure similar to the one used at zero field. The only difference was a longer stabilization period, which has to be chosen properly taking into account the decreasing thermal conductivity of the copper H-bar at high fields.

To illustrate the possible problems with the thermal conductivity (which

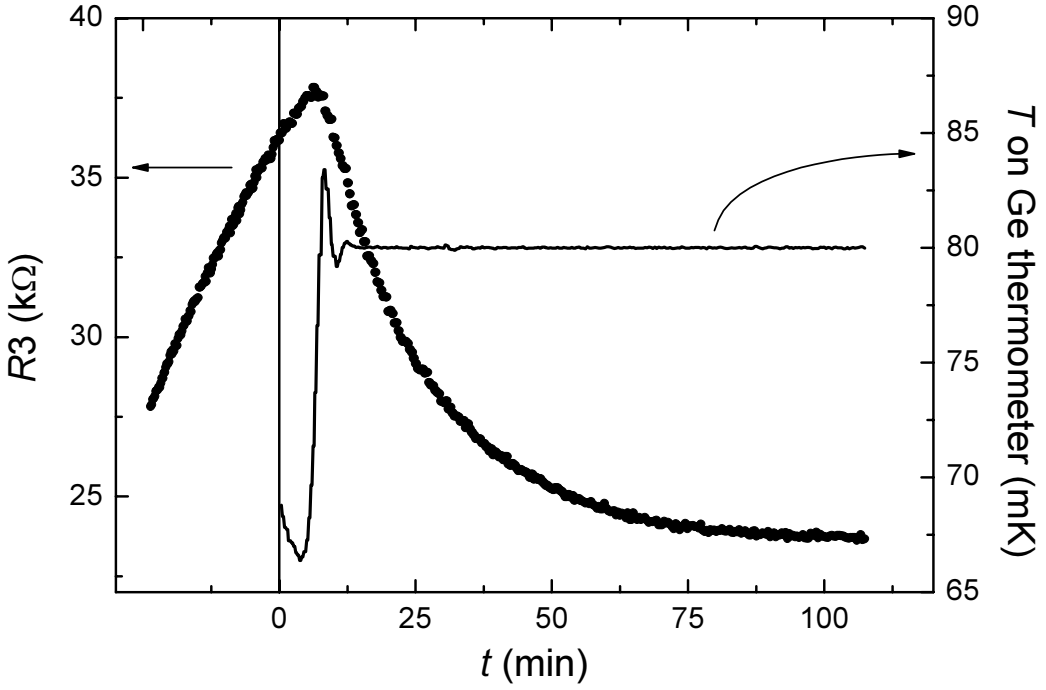

Figure 2.3: Relaxation of the resistivity of thermometer $R3$ after the temperature controller starts to regulate temperature.

were avoided in our experiments) we show in Fig. 2.3 the relaxation of resistance $R3$ after the ORPX-1 starts to regulate the temperature to reach $T = 80$ mK at an external field of 8.5 T. Before $t = 0$ no heater was switched on and the refrigerator was cooling to base temperature, as can be seen from the increasing value of $R3$. The time when regulation started corresponds to $t = 0$ on the time axis. In about 15 minutes the Ge thermometer reaches a stable temperature. The sensor $R3$, however, needs more than one hour to achieve a stable value. Such a long relaxation is due to the poor thermal conductivity of the H-bar. After several experiments similar to the one shown in Fig. 2.3 a minimum relaxation time was determined for each value of temperature and magnetic field.

In Fig. 2.4a we show the relative change of the resistivity for several selected temperatures. The magnetoresistance was found to be positive in the entire studied temperature range 80 mK - 0.8 K. Using the calibration function obtained at zero field, we can calculate the apparent temperature T_a ignoring the effect of magnetoresistance. Since the real temperature T is known as well, it is possible to find a systematic error $\Delta T = T_a - T$ at each field and temperature. Fig. 2.4b shows the relative error in the temperature reading $\Delta T/T$ vs B. Despite one order of difference between the lowest and highest temperatures all

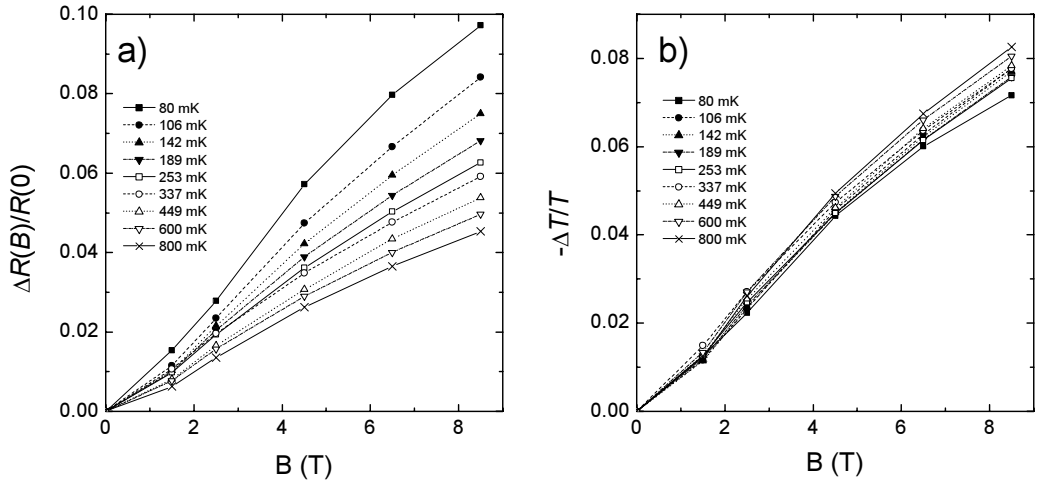

Figure 2.4: Magnetoresistance (a) and relative change of apparent temperature (b) of a RuO_2 thick film resistor. The data shown are for sensor $R3$.

curves in Fig. 2.4b stay very close together suggesting that the systematic error $\Delta T/T$ is a function of the magnetic field, and not of temperature. This rather surprising result turns out to be of much practical use when studying quantum criticality. It means that by measuring the temperature at some magnetic field, let say 8 T, we always have the same error of about 7%, regardless the actual value of T. Plots, where critical behavior is analyzed, usually show the temperature on a logarithmic scale. The temperature error will produce a shift of the entire curve, but not a change of the curve itself or the value of the exponent. The small differences, which can be seen between the different curves in Fig. 2.4b, could affect the critical exponent only in the third significant digit, which is well beyond the experimental accuracy.

Unfortunately, the highest field up to which calibration can be done in this way is 9 T - the upper limit of the superconducting magnet used with the 200S dilution refrigerator. Extension of the magnetic field range, however, is possible at higher temperatures. The magnetoresistance of the same thermometer was measured in a conventional ^{4}He bath cryostat where the temperature was regulated by pumping helium gas at constant vapor pressure. Since the vapor pressure of ^{4}He does not depend on the magnetic field it gives us the true temperature. This experiment was done at the Nijmegen HFML in fields up to 30 T. The results are shown in Fig. 2.5.

Again all curves are close to each other, although at 30 T the systematic error reaches an impressive 18%.

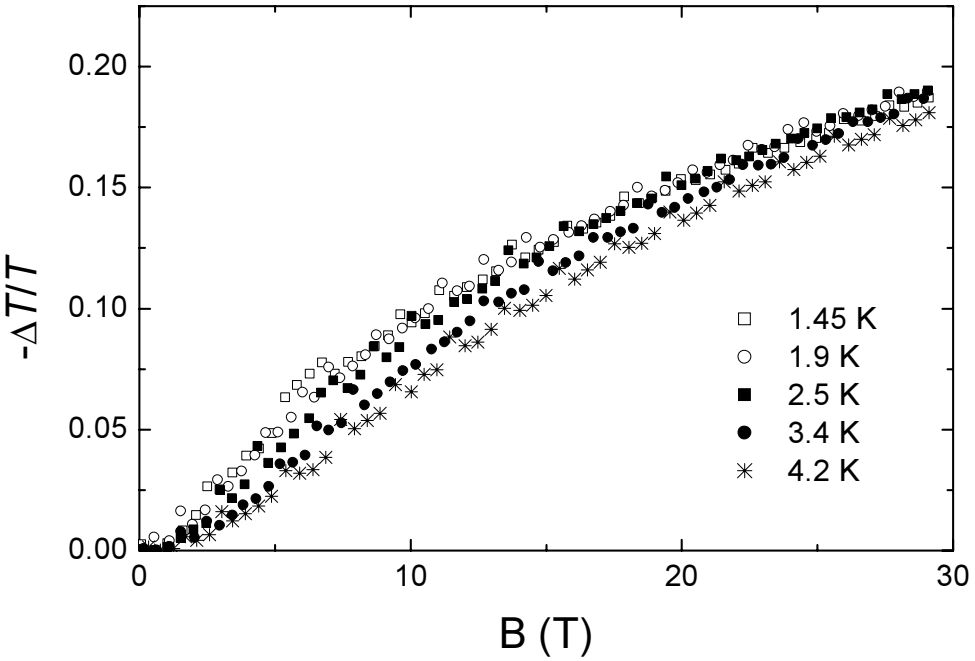

Figure 2.5: Magnetoresistance of RuO_2 sensor $R3$ at very high magnetic field.

2.4. Measurements of resistance

In this Section we describe the application of the 4-probe resistance method at low temperatures and at high magnetic field.

As regards resistivity measurements at milliKelvin temperatures, a most important parameter to consider carefully is the value of the measuring current I. The current should be relatively low to prevent Joule heating of the sample, but at the same time it should be high enough to provide reasonable signal-to-noise ratio. The easiest way to check if the sample temperature is affected by the current is to measure the resistance with different values of I keeping the other parameters unchanged. Assuming that the $V - I$ characteristic is linear, a resistance change can then only be due to heating of the sample. In this case, the current should be decreased accordingly until no further change is observed. In most cases, the proper value of the current in quantum Hall experiments is so small that a satisfactory signal-to-noise ratio can be achieved only by the low frequency AC method, also known as the lock-in technique.

The scheme in Fig. 2.6 illustrates this method and at the same time shows some features of our experimental setup. The internal oscillator of one of the lock-in amplifier is used to create a current through the sample. Since the oscil-

lator is a voltage source, and not a current source, the value of I is kept approximately constant with help of the 100 MOhm resistor connected in series with the sample. An additional 100 kOhm resistor is used to monitor the value of the current. All voltage leads on the sample are led to preamplifiers installed on top of the cryostat. The preamplifiers serve several purposes. Besides the obvious role of amplifier, they allow to keep the connecting cables short, and thus the capacitances between wires and ground as small as possible. In the following paragraph we show that these capacitances play a crucial role when the sample undergoes a transition to the insulating state. Another reason for using preamplifiers is their high input resistance. According to a general rule, the contact resistances should be much smaller than the input resistance of the detecting device. For our preamplifiers the input resistance is 100 MOhm, which is 10 times larger than the input resistance of the lock-in amplifier. Finally, due to the low output impedance of the preamplifiers the cables connecting them with the lock-in amplifiers can be rather long. In our setup the length of the cables is about 6 m. This length allows us to keep sensitive and complex devices like lock-in amplifiers at some distance from the magnet in order to reduce the possible disturbing effect of stray magnetic field. The preamplifiers are proven to be immune to stray field[2]. Additional noise unavoidably occurring in the long cables is not an issue. The amplification factor of the preamplifiers ($\times 1000$) is high enough to keep the signal-to-noise ratio almost as good as it is right at the preamplifier input.

For simplicity we show in Fig. 2.6 only three preamplifiers and three lock-in amplifiers. The most left preamplifier is used to record the current, while the other two serve for measuring the longitudinal and Hall voltages, respectively. In a real experiment, however, we use five lock-in amplifiers (each in combination with a preamplifier) to record the current, two longitudinal and two Hall resistances at the same time. In Chapter 4 we discuss the need for such simultaneous measurements and show how data obtained from different pairs of contacts can be used to extract crucial information about sample inhomogeneities.

Experiments on the plateau-insulator transition, which are presented in Chapters 5 and 6 require measurements of the resistance in a very broad range, ideally, from 0 to ∞. The lock-in technique, however, like any other method, has its limitations. The lowest value of the resistivity which can be measured

[2]Perhaps the easiest way to prove this is to measure the quantum Hall effect and make sure that R_H is quantized at proper value.

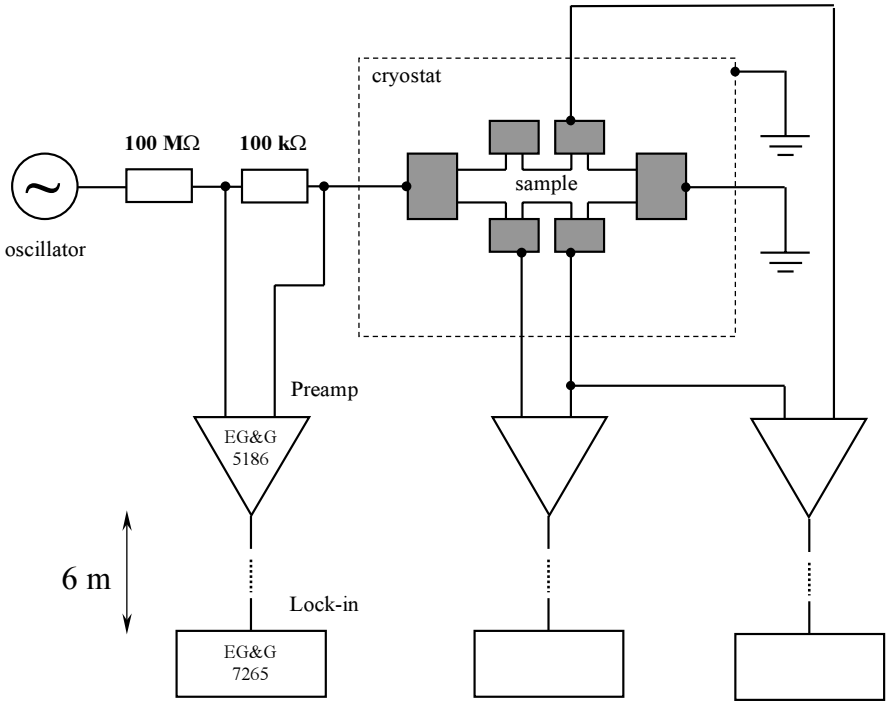

Figure 2.6: Scheme of the 4-point resistance measurements on a Hall bar by the lock-in technique.

by the lock-in technique in a dilution refrigerator depends on the noise level and the maximum current that can be applied without warming up the sample. In practice, this limit is often below 1 Ohm and the experimental error is related to random noise. The upper limit depends mostly on the capacitance between cryostat and wires. The experimental error in this case is systematic. Therefore it is very important to have a tool for recognizing reliable data and to be able to cope with this problem during measurements.

Due to the relatively large size of dilution refrigerators, the wires, which go from the sample to the top of the cryostat, are about 2-3 m long. At several places the wires are thermally anchored to cold fingers. Because of that, the capacitance between the wires and the cryostat ground is of the order of several hundred picofarad. Coaxial cables, which connect the top of the cryostat to the preamplifiers, have a capacitance of 50 pF/m. Though these are kept as short as possible, coaxial cables do contribute to the total capacitance as well. Additional problems can be created by RF filters often used to prevent heating of the dilution refrigerator from radio frequency radiation.

The lock-in technique is essentially an AC method. For a typical capacitance between the wires of $C = 700$ pF and a working frequency $f = 13$ Hz,

which is a rather usual value for the lock-in method, a simple estimate of the impedance is $X = 1/(\omega C) = 1/(2\pi f C) \approx 17$ MOhm. Except for the insulating phase at the plateau-insulator transition, the typical resistance values measured in the quantum Hall effect are three orders of magnitude smaller. Therefore, the capacitance between the wires and the common ground does not play a role as long as transitions between plateaux are considered. However, the situation changes when the sample undergoes a transition to the insulating phase. Once the sample resistance becomes comparable to the impedance of the wiring circuit a part of the current can run from the oscillator to the drain avoiding the sample or at least some parts of it. In other words, not all the current flows from one current contact to the other. In Fig. 2.7a we show the results of a simple calculation for two different frequencies, which illustrates the deviation of the apparent (measured) resistance R^* from its real value R as a function of R. The sample is assumed to be connected in the same way as in Fig. 2.6, with $C = 700$ pF for all six wires and with all contact resistances equal to the resistance of the sample. These calculations were made with help of the Mathematica 5 package using only Kirchhoff equations. To simplify the model we did not take into account Hall voltages V_H occurring in the sample, because in the insulating state V_H is small compared to the potential differences occurring due to Ohm's law. The apparent resistance turns out to be smaller than the real one. Unfortunately, the result presented in Fig. 2.7a is qualitative only and cannot be used to correct the data. This is because, firstly, the calculations do not take into account the mutual capacitances between the wires, which makes the overall effect much stronger, and secondly, because all capacitances in the real experimental setup have different values. The only way to reduce the leakage current through the capacitances, is to decrease the working frequency f, which will make the impedance higher. Fig. 2.7b shows the longitudinal resistance $R(B)$ of sample 21232-#3 at the transition to the insulating phase measured at different frequencies. The $R(B)$ dependence is expected to be almost linear in a plot of $\log R$ vs $1/B$ as indicated by the dotted line (note the reciprocal scale along the B-axis). Above a certain value of R, the experimental curves start to deviate from the linear behavior, but the lower frequency curve deviates less and at higher resistances. Further decreasing of the frequency can solve the problem related to the capacitance of the wires. However, decreasing of f requires proportional increase of the time constant of the lock-in amplifier and the whole experiment becomes slower. Use of a frequency below 1 Hz was found unprac-

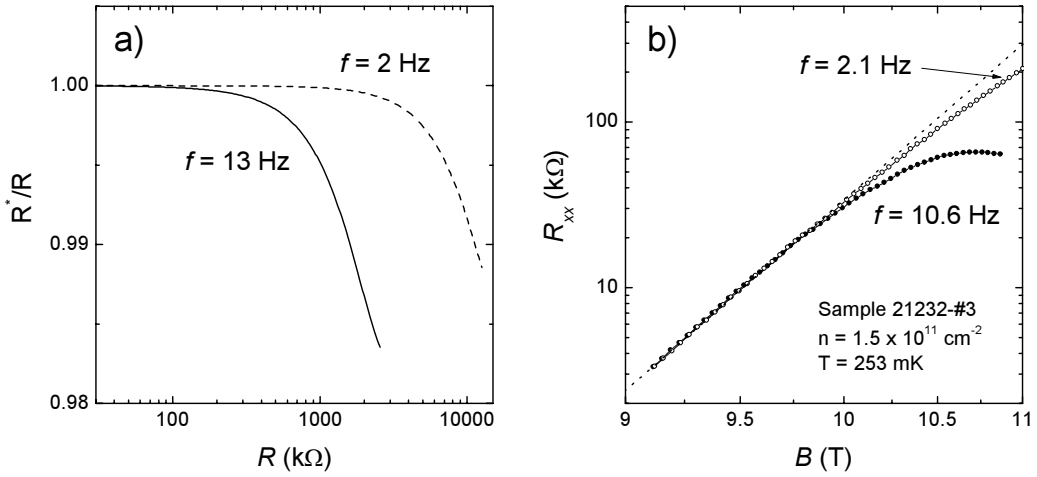

Figure 2.7: Illustration of systematic errors occurring in AC transport measurements due to the large resistance of the sample and a finite capacitance between wires and cryostat. (a) Simulation of the apparent (measured) resistance as a function of the sample resistance for different values of the measuring frequency. (b) Experimental data confirming the results of the simulations.

tical. The measurements become very time consuming and require staying at a high magnetic field for a long time, which is financially non attractive.

In this situation the experimentalist has to be able to determine which data can be trusted. The easiest way is measuring the out-of-phase signal. The capacitive circuit creates a phase shift between the oscillator and the measured voltages, which can be easily detected by the lock-in amplifiers. We determined that the systematic error in $R(B)$ stays within a few percents if the out-of-phase signal (with phase shifted by 90°) does not exceed 10% of the in-phase component.

2.5. Sample selection

The preparation of samples suitable for our research, *i.e.* with a low density but still a high degree of homogeneity, is not a straight-forward task. In the sample preparation process many growth conditions are involved, and they should be optimized by repeatedly preparing and subsequently testing of the samples.

For this thesis work we investigated a large number of two-dimensional structures from different sources and then selected those, which suited our needs. In total more than 70 samples have been tested. Only a handful turned

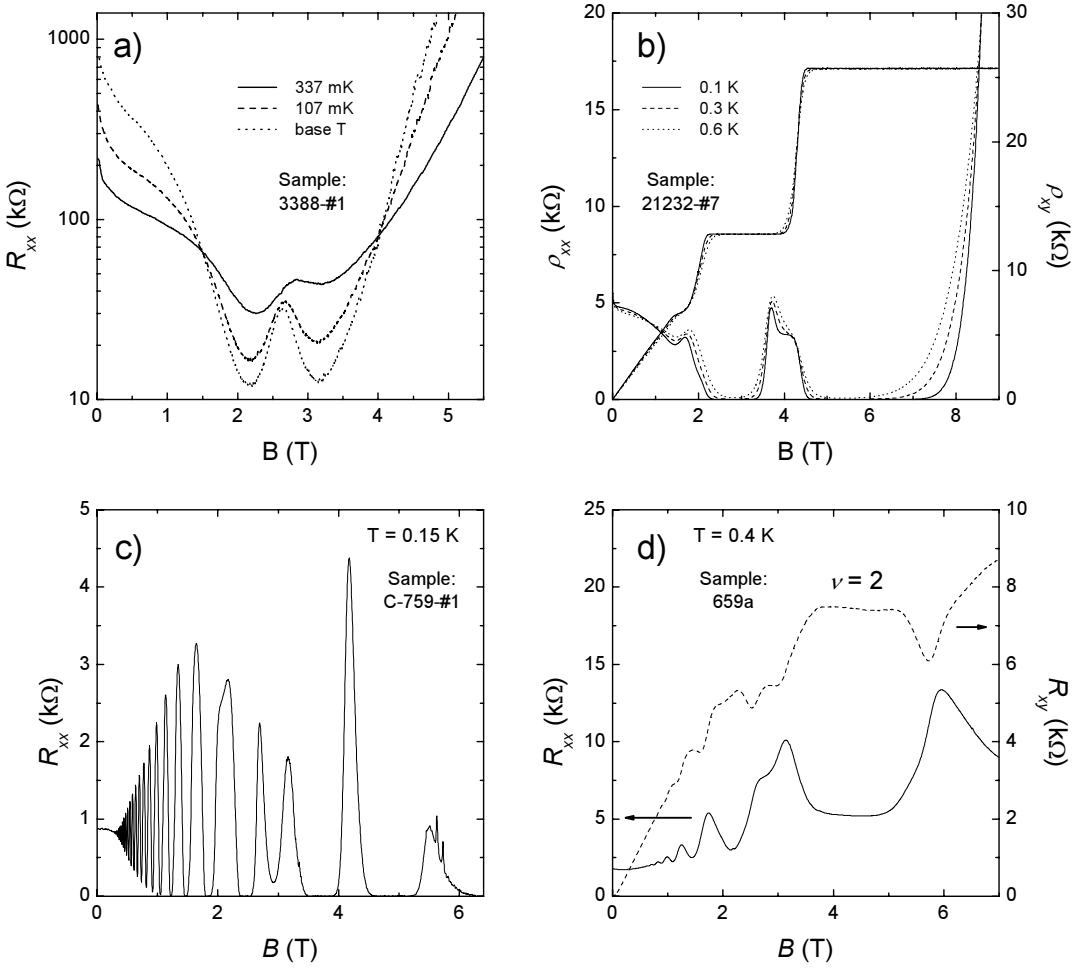

Figure 2.8: Quantum Hall data taken on samples with different types of material problems: a) too low mobility; b) macroscopic inhomogeneities; c)"quantum fluctuations"; d) parallel conductivity.

out to be suitable for studying critical behavior of the QHE. In this Section we discuss the requirements that samples have to fulfil in order to be considered as good candidates for scaling. We also show general examples of data sets obtained on "bad" samples.

The most obvious parameters that determine the sample choice are the carrier density and transport mobility. The electron density of the 2DEG determines the values of the magnetic field at which the PP and PI transitions take place. The highest field is obviously attained for the PI transition: $B_c^{PI} \approx 2hn/e$. Since the strongest continuous (resistive) magnets nowadays provide fields of the order of 30 T, the above relation gives a maximum density $n_{max} = 3.6 \times 10^{11}$ cm^{-2}, at which both the PI and PP transitions can be observed. Although from

the physical point of view there is no lower limit for the density, in practice, it is difficult to obtain samples with $n < 10^{11}$ cm^{-2} which at the same time shows the QHE with well resolved PP transitions. This is because of the poor mobility in such samples. Considering the problem on the microscopic level, a low mobility is caused by intrinsic disorder, which cannot be sufficiently screened if the density is too low. This in turn makes the Landau levels very broad and quantization becomes hardly visible in transport measurements. From a practical point of view, the zero field mobility μ should be $\sim 10\,000$ Vs/cm^2 or higher, in order to study at least one properly separated PP transition in a broad temperature range. In Fig. 2.8a we show the magnetoresistance of a GaAs/InGaAs quantum well (sample 3388-#1) at several temperatures. The peak around 2.5 T on the curve measured at base temperature is the $2 \rightarrow 1$ PP transition. With increasing T, the peak quickly disappears rendering the analysis of critical behavior impossible. The electron density and zero field mobility (estimated at 4.2 K) for the sample used in Fig. 2.8a are $n \approx 1.0 \times 10^{11}$ cm^{-2} and $\mu \approx 3300$ Vs/cm^2, respectively.

An upper limit for the mobility is $\sim 10^6$ V s/cm^2, above which fractional rather than the integer quantum Hall effect is observed.

Low density samples can be studied with rather moderate magnetic fields, however, they often suffer from macroscopic inhomogeneities. To illustrate the problem, we show in Fig. 2.8b magnetoresistance data from sample 21232-#7, where the inhomogeneities are so strong that their effect can be seen directly in the experimental data. The peak on the curve $\rho_{xx}(B)$ at 4 T corresponds to the $2 \rightarrow 1$ PP transition, but at low temperatures it has a "double" structure, which looks like partial spin splitting. However, the $2 \rightarrow 1$ transition is already spin separated and the additional structure can only be due to different densities in two parts of the sample, as was confirmed by data taken from different pairs of Hall contacts. Otherwise, the curves in Fig. 2.8b represent a perfect quantum Hall effect with broad plateaux in $\rho_{xy}(B)$ and zero resistance for $\rho_{xx}(B)$. In the case of the data shown in Fig. 2.8b, it is obvious that the sample contains two regions with distinct electron densities. If the carrier concentration were to change smoothly across the sample, the transition would not show such a structure, but rather its width would be affected. The influence of carrier density distributions is especially pronounced at low temperatures. In Chapter 4 we pay much attention to this problem and discuss the effects of inhomogeneities on the critical exponents extracted from the experimental data.

Another type of problem often present in measurements on the quantum

Hall effect is reported in Fig. 2.8c. Here we show the magnetoresistance of a rather high mobility ($\mu = 85\ 000$ cm^2/Vs) InGaAs/InP heterostructure. Peaks at 4.2 T and 5.6 T represent the $4 \rightarrow 3$ and $3 \rightarrow 2$ PP transitions, respectively. Both transitions belong to the same Landau level split by the magnetic field. The peak at 4.2 T is smooth and its shape is close to the one expected from theory. In contrast, the peak at higher field is much smaller and has a reproducible fine structure, unique for each pair of contacts. Such a behavior is similar to that observed for mesoscopic structures (see, for example [39]), but in our case the sample has quite macroscopic dimensions and it is hard to imagine that the localization length approaches the sample size. The effect is clearly spin dependent: a closer look at the next set of spin-resolved PP transitions at 2.7 T and 3.2 T reveals fluctuations in ρ_{xx} of the $5 \rightarrow 4$ peak, while the $6 \rightarrow 5$ transition is again absolutely smooth. Although the origin of the fine structure is not clear, the $3 \rightarrow 2$ PP transition surely is not suitable for studying critical behavior.

The last common problem we would like to mention here is parallel conductivity, illustrated in Fig. 2.8d. In this case the 2DEG is not the only medium, which carries the current in the sample. Part of the current flows through another layer, presumably those with doping atoms. The conductivity of this layer is of a three-dimensional nature and this results in a distortion of the $\rho_{xy}(B)$ and $\rho_{xx}(B)$ curves. The plateaux are not strictly quantized and appear at lower resistance values than expected. At the same time the longitudinal resistance never reaches zero.

The curves shown in Fig. 2.8b-d were selected as extreme examples. Usually the unwanted effects are much smaller, but it does not mean that their interference with critical behavior is negligible. Ignoring the fact that the shape of the magnetoresistance curve depends on many factors (some of which may not be completely understood) can lead to wrong conclusions. Some historical examples of work on improper samples will be given in the next chapters.

3

THEORETICAL BACKGROUND

3.1. Strong localization and quantum Hall effect

Currently, there is number of - quite different - models which offer an explanation for the formation of plateaus in the Hall resistance over a finite range of magnetic fields. Without going into details of these theories we stress that all of them have the same basic ingredient: the quantization of the Hall resistance is derived from the coexistence of the localized and extended states in the band structure of the 2DEG exposed to a strong perpendicular magnetic field.

Localization of electrons in the 2DEG has its origin in disorder, inherently present in semiconductor materials. The sources of disorder can be quite different. In principle, one can distinguish short-ranged and long-ranged disorder depending on the ratio of the magnetic length $l_B = \sqrt{\hbar/(eB)}$ and the correlation length of the disorder potential λ. For a magnetic field of 10 T, which is a rather typical value for the QHE experiments, the magnetic length is of the order of 8 nm. Hence, alloy scattering in InGaAs, where disorder appears on the interatomic scale, is short-ranged. On the contrary, scattering by the Coulomb potential of charged doping ions, separated *e.g.* by a 100 nm thick spacer from the 2DEG, is long-ranged. The short-ranged disorder potential can be treated in the Hamiltonian by δ-functions, which facilitates the calculations. In the case of long-ranged disorder, however, the details of the potential distribution come into play and render the calculation difficult. For instance, scattering on the interface between two semiconductors (which can be both long- and short-ranged) may have a different effect than scattering on charged ions in the

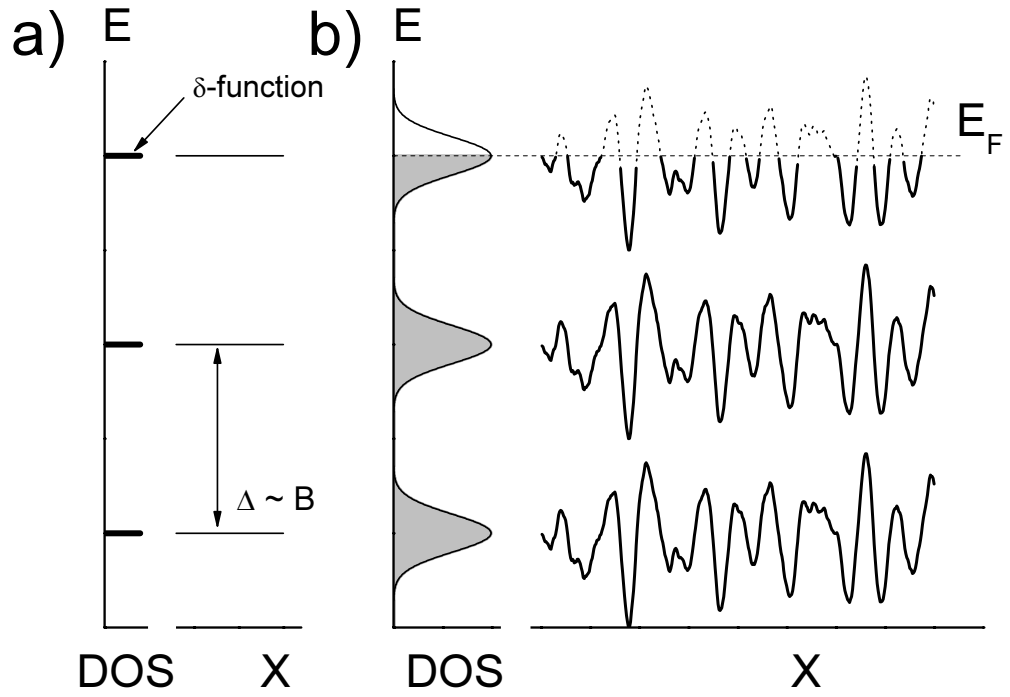

Figure 3.1: The Landau level structure of the 2DEG without (a) and with (b) disorder. X is the real space position.

dopant layer.

The necessity of disorder for observing the QHE can be demonstrated using Lorentz's covariance argument [40]. In the absence of impurities the 2DEG is translationally invariant and there is no preferred frame of reference. Choosing a reference frame which moves with arbitrary velocity $\mathbf{v}$, one "generates" a current with density $\mathbf{J} = n_e e\mathbf{v}$ in the 2DEG. At the same time the electric field $\mathbf{E} = \mathbf{v} \times \mathbf{B}$ exists in the moving reference frame due to the Lorentz transformation. Note, that the electric field $\mathbf{E}$ is perpendicular to both vectors $\mathbf{B}$ and $\mathbf{J}$ and proportional to their absolute values. From this we can find non-diagonal elements of the resistivity tensor $\rho_{xy} = E/J = B/(n_e e)$, which is just the classical result for the Hall resistivity with linear dependence in B. Hence, to observe quantization in ρ_{xy} translational symmetry of the system has to be destroyed. This is realized by including disorder.

In the case of long-ranged disorder, a quasi-classical picture can be used to explain the localization of charge carriers on spatial fluctuations of the disorder potential. The basic ideas are illustrated in Figs. 3.1 and 3.2. We start with a comparison of the 2DEG without (Fig. 3.1a) and with disorder (Fig. 3.1b). In the former case, the energy of each Landau level has the same value everywhere in

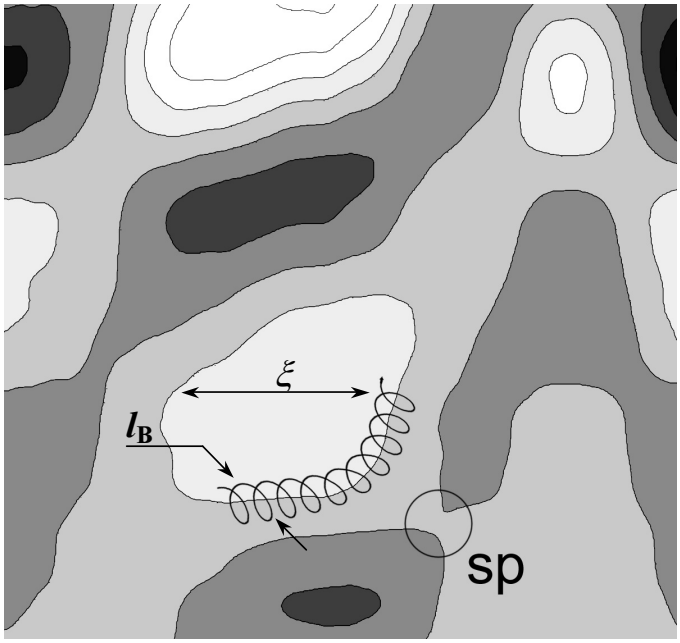

Figure 3.2: Semiclassical picture of localization of the electron on the long-ranged disorder potential. The grayscale represents regions with different potential energies. The electron drifts along a line of constant potential, although the actual trajectory is spiral-like. The circle indicates the position of a saddle point (SP).

the sample, so the density of states (DOS) is represented by δ-functions at the energies given by Eq. (1.4). In the latter case, disorder causes the energy of the Landau level to change across the sample, so the averaged DOS function has a finite width and the Landau levels become broader. In Fig. 3.1b we also show the Fermi level E_F. The number of Landau levels below the Fermi level is given by the filling factor ν. Fig. 3.1b depicts the situation with $\nu = 2.5$.

Next consider a long-ranged disorder potential assumed to be smooth on the scale of the magnetic length l_B. The motion of the carriers in such a system is then determined by drift along the lines of constant potential. In the particular example shown in Fig. 3.2, the carrier's drift path is closed. The classical electron at $T = 0$ is not able to leave such a trajectory. Hence, it cannot travel from one current contact to another (unless the trajectory line connects both contacts). Such an electron is localized. Depending on the energy, different trajectories have different sizes, which can be associated with the localization length ξ. If the sample size is smaller than the localization length, the electron, obviously, is delocalized. Determination of the localization length is one of the important tasks in any theory of the QHE.

Various numerical calculations [41, 42, 43, 44, 45, 46] using a free electron approximation suggest surprisingly similar results for the energy dependence of the localization length ξ. Namely, near the center of the Landau level $E_{n,s}$ the parameter ξ diverges as:

$$\xi \propto |E - E_{n,s}|^{\chi}, \tag{3.1}$$

where the localization length exponent χ is of the order of 2.3. Within the accuracy of these calculations (which varies between 2% and 20%) the results agree with each other and are close to the recent analytical estimate $\chi = 2.8 \pm 0.4$ obtained in the renormalization group framework [47]. Therefore, in an infinitely large sample with random potential fluctuations all electrons are localized ($\xi < \infty$), except those with energies exactly in the middle of the Landau levels: $E = E_{n,s}$, where $E_{n,s}$ is given by Eq. (1.4).

Dissipative transport (*i.e.* a non-zero longitudinal resistance) is provided by the extended electrons on the Fermi surface. Hence, at $T = 0$ dissipation takes place only when $E_F = E_{n,s}$, which holds under the condition of a half-integer value for the filling factor ν (like the case depicted in Fig. 3.1b, with $\nu = 2.5$). Since dissipation at $T = 0$ is possible only at discrete values of ν, the peaks in the longitudinal resistance ρ_{xx} as a function of ν (or B, since $B \propto \nu^{-1}$) are infinitely narrow and the transitions between plateaus in ρ_{xy} are infinitely steep. The filling factor at which the transition takes place is called the critical filling factor ν_c. As follows from above, ideally, ν_c is a half-integer number.

At finite temperature, the electrons can be transferred from one closed trajectory to another. In the semiclassical case, such events are likely to take place at the saddle points (Fig. 3.2) where two equipotential lines with the same energy approach each other. This leads to delocalization of some part of the electrons at finite T. The probability of delocalization is higher for the electrons with energies closer to $E_{n,s}$. As a result, at $T > 0$ a band of extended states with finite width ΔE appears around the center of each Landau level (in contrast with the $T = 0$ situation, where the width of extended states is infinitely narrow).

The finite width of the extended states ΔE at $T > 0$ explains the non-zero longitudinal resistance ρ_{xx} over a finite range of the magnetic field and filling factor in the transition region between two plateaus.

3.2. Scaling theory of the quantum Hall effect

The short discussion of scaling in Section 1.2 refers only to the methodology how to extract the critical exponent κ from the magnetotransport data. In this Section we describe a few basic ingredients of the scaling theory and discuss the meaning and numerical value of the exponent κ.

We start with some introductory remarks about the renormalization group theory (RGT). RGT has been developed in the sixties of the last century in order to examine and model phase transitions. The RGT turns out to be extremely useful when the initial problem is too complicated to be solved from first principles, which is the case for most phase transitions. The idea of renormalization is due to Wilson, who put forward that in the vicinity of the critical point the system can be effectively mapped onto itself, but on a different scale and for different values of external parameters (temperature, magnetic field *etc*). The critical point always transforms into itself and is therefore called the fixed point. Perhaps, the most difficult part of the analysis is to prove that renormalization indeed can be applied to the particular system. In the case of the quantum Hall effect, this was successfully demonstrated by Pruisken [12, 13] for the non-interactive case in 1987, and more recently for systems which include interactions [48]. Once the system is proven renormalizable, determination of the appropriate scaling functions becomes a technical problem.

It is beyond the scope of this thesis to enter in details of the RGT model of the QHE, which is often referred in literature as the "scaling theory of the quantum Hall effect". Here we only focus on the main concepts and results. We first define a fixed point in the conductivity plane σ_{xx}-σ_{xy}. At the quantum critical points the components of the conductivity tensor attain the values [20] (in units e^2/h):

$$\sigma_{xx,c} = \frac{1}{2}, \quad \sigma_{xy,c} = n + \frac{1}{2}, \;\; n = 0, 1, 2... \tag{3.2}$$

The next step is to define the scaling variables (*i.e.* variables which are transformed upon renormalization):

$$\sigma = \sigma_{xx} - \frac{1}{2}, \quad \theta = \sigma_{xy} - n - \frac{1}{2} \tag{3.3}$$

The scaling variables, σ and θ, are called the irrelevant and relevant variables, respectively. At the fixed point $\sigma = \theta = 0$.

Under renormalization the effective size of the system is changed: $L \rightarrow bL$ (a procedure called finite-size scaling). Note, that the parameter L should not

be taken literally as the sample size, because making the sample smaller than the localization length ξ affects the transport coefficients in an unpredictable way due to conductance fluctuations. In the scaling theory L is associated with the phase coherence length L_φ (or Thouless length [49]), which is a function of temperature:

$$L_\varphi \propto T^{-p/2}, \tag{3.4}$$

where p is the dynamical critical exponent. Note, that the last expression is not a result of the renormalization. This relation just establishes a link between the characteristic length scale (a "knob" in the renormalization group theory) and the temperature, which can be set in the experiment (a "knob" in the experiment). The exact value of the exponent p still has to be clarified. The only theory available at the moment [50] was developed for the zero magnetic field case and gives a value of p bounded between 1 and 2.

The change of the effective system size transforms the scaling variables according to $\theta \to b^{y_\theta}\theta$ and $\sigma \to b^{-y_\sigma}\sigma$, where y_θ and y_σ are the relevant and irrelevant exponents, respectively.

One of the goals of the scaling theory is to identify the exponents y_θ and y_σ with experimentally measurable quantities. It has been shown that the relevant exponent y_θ is just the inverse of the localization length exponent χ, which enters into the leading term (dominant at low temperatures) of the expression for the components of the conductivity tensor:

$$\sigma_{\alpha\beta}(L_\varphi, B) = f_{\alpha\beta}(L_\varphi^{1/\chi}(B - B_c)) + O(L_\varphi^{1/\chi}(B - B_c)^2, L_\varphi^{-y_\sigma}) \tag{3.5}$$

where B_c is the critical field and $\alpha\beta$ stands for the arbitrary combination of x and y. The last expression is considered to be one of the most important results of the scaling theory of the QHE. First of all it shows that both components of the conductivity (to leading order) depend on a single variable $L_\varphi^{1/\chi}(B - B_c)$ rather than two separate variables L_φ and B. Then, according to Eq. (3.5) at low temperatures only the localization length exponent plays a role, so the irrelevant exponent y_σ can be neglected. And finally, taking into account Eq. (3.4) we can now explain the meaning of the exponent κ introduced in Section 1.2. Since near the critical point $B - B_c \propto \nu - \nu_c$ (first term of the Taylor expansion near ν_c), it becomes clear that:

$$\kappa = \frac{p}{2\chi}. \tag{3.6}$$

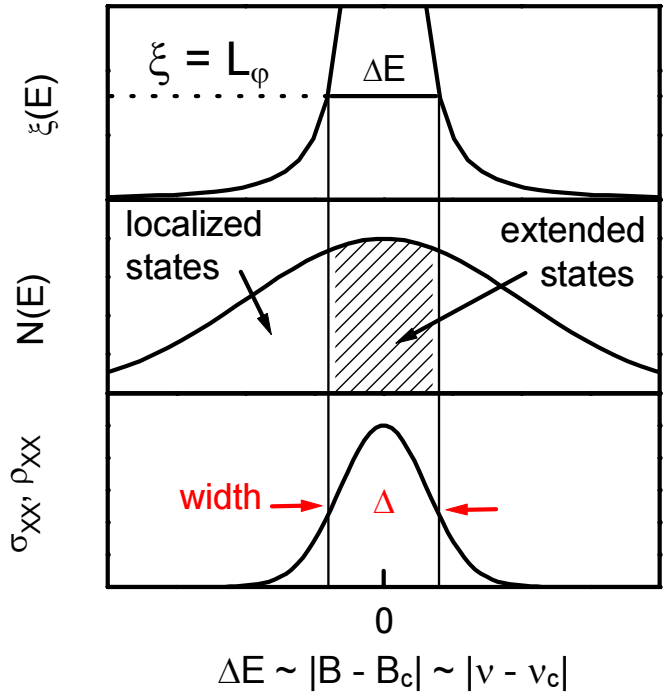

Figure 3.3: Sketch of the localization length ξ, the density of states function N and the longitudinal conductivity σ_{xx} near the center of the Landau level at finite temperature.

Scaling theory in its initial form [10] does not give any estimates for κ, but predicts it to be universal. More recent theoretical work [47] yields the non-interacting case estimates $\chi = 2.8 \pm 0.4$ and $y_\sigma = -0.17 \pm 0.02$, which are in good agreement with results of numerical calculations [41, 42, 43, 44, 45, 46]. Developing theory, which includes the electron-electron interaction is a tedious task and is in progress [48].

Implications of the scaling theory can be qualitatively illustrated with help of Fig. 3.3. Each transition between two plateaus can be regarded as an insulator-metal-insulator transition[1]. Whether the sample is in the insulating state or not, depends on the ratio of the localization length ξ and the phase coherence length L_φ. The condition for metallic behavior can be expressed as $L_\varphi(T)/\xi(B) \leq 1$, which means that the localization length is larger than the effective size of the system and the electron states are extended. The condition $L_\varphi(T)/\xi(B) \gg 1$, in contrast, stands for localized electrons and results in insu-

[1]It may not sound appropriate to call the sample, which carries dissipationless current an insulator. Nevertheless, this is a common name due to the fact that $\sigma_{xx} = 0$ and the Fermi level lies in the band of the localized states.

lating behavior (for which the plateau is observed). According to Eq. (3.1), the localization length ξ diverges at the critical point as shown by the solid line in the upper panel in Fig. 3.3. With decreasing T the phase coherence length L_φ increases (see Eq. (3.4)), so the level $\xi = L_\varphi$ indicated by the dotted line in the upper panel also moves up. This leads to shrinking of the band of the extended states (middle panel). The extended states are responsible for finite resistance and conductance of the system (lower panel). Such a qualitative description alone suffices to explain the temperature dependence of the transition width $\Delta B \sim T^{p/2\chi}$, however it does not give all the results following from Eq. (3.5). For example, it does not predict existence of the scaling functions $f_{\alpha\beta}$.

Existing theories and numerical work allow one to make estimates for the value of κ. As mentioned in the previous Section, the most quoted value of the localization length exponent χ obtained from the quantum percolation network model [41, 46] and numerical calculations within the Fermi-liquid model [41, 42, 43, 44, 45, 46] is $\chi \approx 2.3$. Since the dynamical exponent p is bounded between 1 and 2, the exponent κ according to Eq. (3.6) is expected to be in the range between 0.22 (for $p = 1$) and 0.43 (for $p = 2$). The last value is in perfect agreement with the experimental result $\kappa = 0.42 \pm 0.04$ obtained in Ref. [14], which is up to now one of the most cited papers on scaling in the QHE. The problem, however, is that $\chi \approx 2.3$ is derived within the Fermi-liquid approach, hence electron-electron interactions are neglected. On the other hand, the value $p = 2$ was obtained in the clean limit for the two-dimensional model in zero magnetic field, where the main scattering is due to electron-electron interaction [51]. Clearly, the basic assumptions of the two models are in obvious conflict with each other. The calculation of the phase coherence length L_φ in the diffusive limit (strong disorder, small electron-electron interaction) gives $p = 1$ and, respectively $\kappa = 0.22$, which disagrees with the vast majority of existing experimental data. Moreover, there are experimental papers, which report the exponent κ to be of the order of 0.6, which is significantly higher than the forementioned upper limit of 0.43. The data presented in this thesis also suggest $\kappa = 0.58 \pm 0.02$. Referring to the concept of universality class, introduced in Section 1.2, this may indicate that the problem of the PI and PP transitions in the QHE and the Fermi-liquid model belong to different universality classes.

Near the critical point, both σ_{xx} and σ_{xy} depend on $X = (\nu - \nu_c)/T^\kappa \propto (B - B_c)/T^\kappa$, which means that both components of the resistivity tensor, ρ_{xx} and ρ_{xy}, are also functions of the same variable X.

Scaling behavior implies the collapse of all experimental data on a single

curve ρ_{xx} *vs* X (for the longitudinal resistivity) or ρ_{xy} *vs* X (for the Hall resistivity). This way of demonstrating scaling, however, is not practical because of several reasons. First of all, one has to plot the data assuming a certain value of κ and critical field B_c (or critical filling factor ν_c). Even if the data do collapse within the error bar, it is not obvious at all, that the chosen values of κ and B_c (ν_c) are the best ones. The second reason is the error bar itself. The data collapse is hardly ever ideal and when several curves are plotted on top of each other it is very difficult to recognize qualitatively (by eye) if deviations are of random nature or have a systematic origin. In this situation, data with larger error bars often look "more convincing" and will sooner be taken as "prove" for scaling.

A way to avoid these uncertainties, and obtain the value of κ from the PP transition, is to plot the width of the peak $\Delta\nu$ extracted from the $\rho_{xx}(\nu)$ dependence as a function of temperature on a double logarithmic scale. If scaling indeed takes place, the plot $\log(\Delta\nu)$ *vs* $\log(T)$ should follow a straight line, the slope of which gives the value of κ. The same holds for the temperature dependence of the maximum of the derivative $d\rho_{xy}(\nu)/d\nu$. This method of extracting κ was successfully used in Ref. [14] and later publications, with the difference that the transition width was determined in terms of the magnetic field (ΔB instead of $\Delta\nu$). In the course of this thesis, we use several ways of extracting κ, described in corresponding experimental chapters.

The second term in Eq. (3.5) describes the corrections to scaling, which become significant at relatively high temperature ($\gtrsim 1$ K in InGaAs/InP heterostructures [52]). Studying corrections to scaling is the only way to determine the irrelevant exponent y_σ because this exponent does not enter the leading term. It was shown recently [52], that the irrelevant exponent controls the deviation of the Hall resistance from the quantized value at the PI transition:

$$\rho_{xy} = 1 + \eta(T)e^{-X}, \quad \eta(T) = (T/T_1)^{\tilde{y}_\sigma}. \tag{3.7}$$

where $\tilde{y}_\sigma = py_\sigma/2$, ρ_{xy} is given in units h/e^2 and T_1 is a phenomenological parameter. The importance of the irrelevant exponent for the complete picture of the QHE in the renormalization group theory is clarified in the following Section.

3.3. Flow diagram and semicircle relation

A flow diagram is a very useful graphical means to illustrate the renormalization group analysis. It locates the fixed points and shows how the scal-

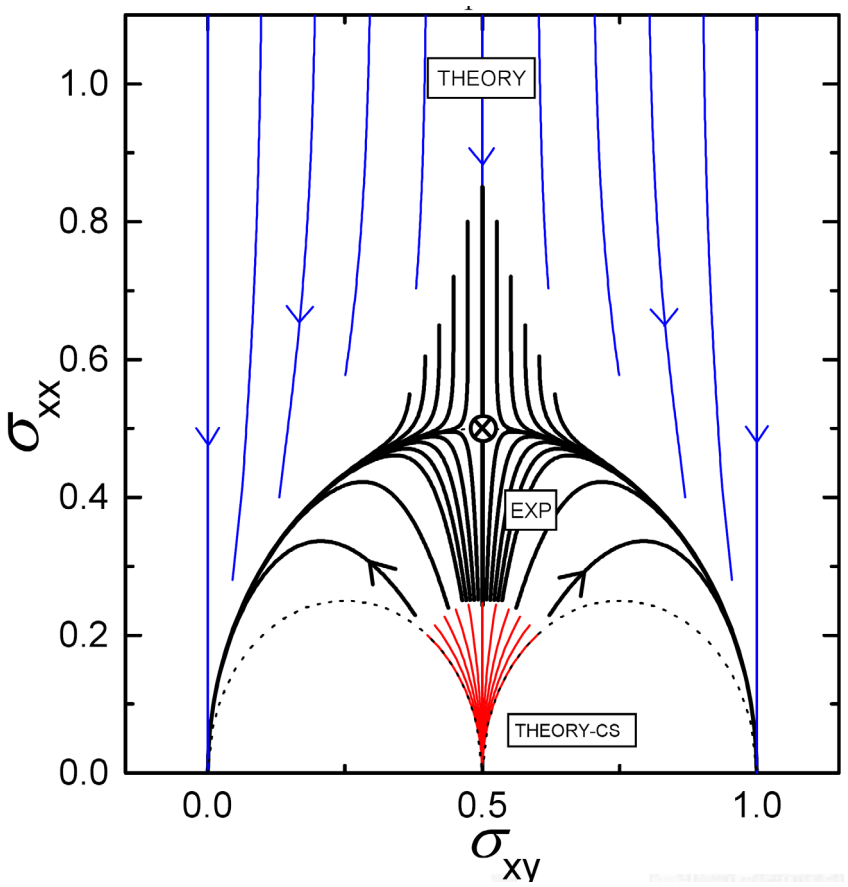

Figure 3.4: Example of the flow diagram of the PI transition taken from Ref. [53]. See text for an explanation.

ing variables change under renormalization group transformation. In general, a flow diagram can be constructed for any renormalizable system. However, the flow diagram for the QHE takes a vary special place when compared to those constructed for other phase transitions, like for instance, magnetic phase transitions in Ising or Heisenberg models. Namely, in the QHE the flow lines can be determined directly from the experimental data, which implies that one can "measure" the flow diagram. In all other models one has no direct access to the flow diagram, as the scaling variables are no directly measurable quantities. An example of a flow diagram for the QHE (PI transition) is shown in Fig. 3.4. The components of the conductivity tensor, which coincide up to an additive constant with the scaling variables θ and σ (see Eq. (3.3)), defines the axes. Each flow line represents the evolution of σ_{xx} and σ_{xy} under finite-size scaling (equivalent to the change of temperature) for fixed value of the magnetic field B.

In this Section we present an up to date point of view on the flow dia-

gram in the QHE, based on recent results of the scaling theory [47, 48].

Characteristic features of the flow diagram for the QHE are the fixed points at $(\sigma_{xy}, \sigma_{xx}) = (i, 0)$ and $(\sigma_{xy}, \sigma_{xx}) = (i + \frac{1}{2}, \frac{1}{2})$. The first point is called the stable fixed point, because all flow lines, except those at $\sigma_{xy} = i + 1/2$, terminate here. Despite of being just a "point", each stable fixed point contains a whole plateau region. The second fixed point, often referred as unstable[2] and indicated as $\otimes$ in Fig. 3.4, represents the critical point of the PP or PI transitions. Existence of this fixed point follows from the fact that the system is renormalizable. The number of flow lines which go to or leave the unstable point is limited to four: there are two vertical lines directed towards the fixed point (vertical flow) and two flow lines which go from the unstable to the stable fixed points (horizontal flow). These last two flow lines form a semicircle:

$$\sigma_{xx}^2 + (\sigma_{xy} - i - 1/2)^2 = 1/4 \tag{3.8}$$

which establishes the relation between the components of the conductivity tensor in the limit $T = 0$.

The flow diagram of the QHE possesses two fundamental symmetries. The first symmetry is particle-hole symmetry, which for the lowest Landau level can be expressed as:

$$\sigma_{xx}(\sigma_{xy}) = \sigma_{xx}(1 - \sigma_{xy}) \tag{3.9}$$

The second symmetry is translational symmetry, which requires σ_{xx} to be a periodic function of σ_{xy}:

$$\sigma_{xx}(\sigma_{xy} + i) = \sigma_{xx}(\sigma_{xy}) \tag{3.10}$$

The flow has a certain "speed" at each point of the diagram. In the neighborhood of the unstable fixed point, the flow speed is determined by the values of the critical exponents. The vertical flow is controlled by y_σ, while the horizontal flow depends on the value of χ.

The positions of the fixed points, the semicircle relation and the two fundamental symmetries are the universal aspects of the flow diagram. Details of the flow, the expressions for the scaling functions and the values of the relevant and irrelevant critical exponents may depend on the strength of the electron-electron interaction, but they are independent on the Landau level index and can be considered "universal within one diagram".

[2]Not to be confused with the point $(\sigma_{xy}, \sigma_{xx}) = (1/2, 0)$ which is also often called unstable.

The first sketches of the flow diagram based on the scaling theory appeared in the literature more than 20 years ago [54, 55] and differ quite a bit from the modern picture shown in Fig. 3.4. The only certainty at that time was the presence of the fixed points at $(\sigma_{xy}, \sigma_{xx}) = (i, 0)$. Neither the exact position of the unstable fixed point, nor the flow line for the limit $T = 0$ were known. Important contributions to establish the final form of the diagram came from numerical work. For instance, while considering five different random potentials, Huo *et al.* [20] found that in all cases the critical point for the lowest Landau level is located at $\sigma_{xx,c} = \sigma_{xy,c} = 1/2$. The semicircle relation between the components of the conductivity tensor at $T = 0$ was obtained for the first time in the two liquid model [19]. Notice that this model presents a very different approach which has no relation to scaling and flow diagrams. The semicircle law was also derived [56] from consistency of two-dimensional scaling flow with the law of corresponding states [57]. A quite interesting result, which stresses the fundamental role of the semicircle, was obtained in Ref. [58]. Here the author showed that the semicircle maps on itself under the Chern-Simons transformation [59], which is used to link the integer and fractional quantum Hall effects.

From the experimental point of view, the semicircle law for the PI transition (lowest Landau level) is now properly established [17, 60]. It follows from the fact that the Hall resistance stays quantized ($\rho_{xy} = h/e^2$) through the PI transition. Indeed, in this case:

$$\sigma_{xx} = \frac{\rho_{xx}}{\rho_{xx}^2 + 1}, \quad \sigma_{xy} = \frac{1}{\rho_{xx}^2 + 1} \tag{3.11}$$

which are the parametric expressions for the semicircle in the σ_{xy}-σ_{xx} plane, provided that ρ_{xx} changes from 0 to ∞.

Corrections to scaling and vertical flow near the PI transition can be observed only when the Hall resistance deviates from h/e^2 [52]. Otherwise all data points are located on the semicircle, where the flow near the critical point is totally horizontal and therefore independent on y_σ.

In case of the PP transition, to the best of our knowledge, true semicircle behavior (with a maximum of σ_{xx} at $1/2$) was not experimentally demonstrated yet.

3.4. Landau level addition transformation

The Landau level addition transformation (LLAT) suggested by Kivelson, Lee and Zhang [57] provides a tool for mapping the PI transition on the

PP transitions. It can be represented by the simple equations:

$$\sigma_{xx}(\nu+1) = \sigma_{xx}(\nu), \quad \sigma_{xy}(\nu+1) = \sigma_{xy}(\nu) + e^2/h. \tag{3.12}$$

These allow to extend the analysis of the universality of PI and PP transitions much further than comparison of the critical exponents.

The idea of transformation was further developed by Oswald, Span and Kuchar [61], who combined LLAT with the Landauer-Büttiker formalism [3] in order to obtain explicit analytical expressions for the components of the resistivity tensor:

$$\rho_{xx} = \frac{h}{e^2} \frac{P}{(\overline{\nu}+1)^2 + (\overline{\nu}P)^2}, \tag{3.13}$$

$$\rho_{xy} = \frac{h}{e^2} \left[\overline{\nu} + \frac{1}{1+P^2}\right] \left[\overline{\nu}^2 + \frac{2\overline{\nu}+1}{1+P^2}\right]^{-1} \tag{3.14}$$

where $\overline{\nu}$ is the number of completely filled Landau levels and the parameter P is a function, which depends on the filling factor of the partially filled Landau level. The dependence:

$$P(\nu, T) = \exp(-(\nu - \nu_c)/\nu_0(T)) \tag{3.15}$$

was chosen as the simplest dependence which fulfills the condition of particle-hole symmetry [57]. In the last equation ν_c is the critical filling factor and $\nu_0(T)$ is a temperature dependent phenomenological parameter. Another important assumption of the model is a quantized value of the Hall resistance at the PI transition.

The critical filling factor ν_c is expected to be half-integer:

$$\nu_c = \overline{\nu} + 1/2 \tag{3.16}$$

It corresponds to a filling factor at which the PI ($\overline{\nu} = 0$) or PP ($\overline{\nu} > 0$) transitions take place in the limit $T \to 0$. The temperature behavior of the quantum Hall effect within the discussed model is determined completely by the temperature dependence of the parameter ν_0 (for which the authors use the notation k). Fig. 3.5 is reproduced from Ref. [61] and shows the traces of the longitudinal and Hall resistances as a function of the magnetic field calculated at several different values of ν_0. The curves properly imitate all characteristic features of the quantum Hall effect, although the model does not take into account sample inhomogeneities or overlapping of the Landau levels (*i.e.* all Landau level, including spin-split levels, are completely separated).

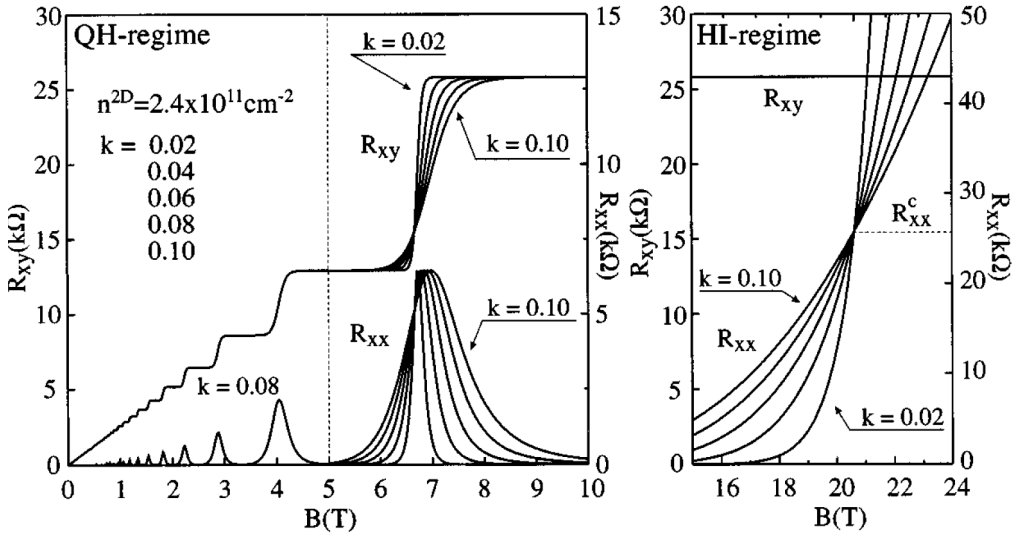

Figure 3.5: The longitudinal and Hall resistances as a function of the magnetic field for a homogeneous 2DEG with carrier density $n = 2.4 \times 10^{11}$ cm^{-2}. Curves are reproduced from Ref. [61]. The parameter k in the figure has the same meaning as ν_0 in the text.

The authors of Ref. [61] do not demonstrate how the parameter ν_0 is related to experimentally measurable quantities like the width of the peak in the $\rho_{xx}(\nu)$ dependence or the maximum slope of the Hall resistance, which are traditionally used for scaling analysis. Having at hand the analytical expressions Eqs. (3.13)-(3.14), it is relatively easy to find these quantities using a software for finding analytical solutions of algebraical equations, such as for example, Mathematica [62]. Here we present a number of relations for practical use. First of all, the full width $\delta\nu$ at the half-maximum in $\rho_{xx}(\nu)$ dependence at an arbitrary PP transition is:

$$\delta\nu = \nu_0 \ln(7 + 4\sqrt{3}) \approx 2.63\nu_0 \tag{3.17}$$

Therefore, the width of all PP transitions at a certain fixed temperature is expected to be the same (independent on the Landau level index). In contrast, the maximum slope of the Hall resistance $(\partial\rho_{xy}/\partial\nu)_{max}$ depends on the number of completely filled Landau levels $\overline{\nu}$:

$$\left(\frac{\partial\rho_{xy}}{\partial\nu}\right)_{max} = -\frac{h}{e^2}\,\frac{1}{2\overline{\nu}(\overline{\nu}+1)\nu_0} \tag{3.18}$$

The peak height in the longitudinal resistivity ρ_{xx}^{max} also depends on the Landau

level, but does not depend on ν_0 and, therefore, is independent on temperature:

$$\rho_{xx}^{max} = \frac{h}{e^2} \frac{1}{2\overline{\nu}(\overline{\nu}+1)} \tag{3.19}$$

Finally, the explicit analytical expressions for $\rho_{xx}(\nu)$ and $\rho_{xy}(\nu)$ allow one to establish a simple relation between the derivative of the Hall resistivity $\partial\rho_{xy}/\partial\nu$ and the longitudinal resistivity ρ_{xx}:

$$\frac{h}{e^2} \frac{\partial\rho_{xy}}{\partial\nu} = -\frac{2\overline{\nu}(\overline{\nu}+1)}{\nu_0}\rho_{xx}^2 \tag{3.20}$$

which turns out to be quite different from the famous "resistivity law" [63, 64, 65, 66]:

$$\rho_{xx} = \alpha B \frac{\partial\rho_{xy}}{\partial B} \tag{3.21}$$

where α is a sample dependent parameter.

It is important to stress that the presented model on itself has nothing to do with scaling, since the temperature dependence of the parameter ν_0 is not specified. However, explicit expressions for the components of the resistivity tensor give us a convenient tool for fitting the experimental data and extract the $\nu_0(T)$ dependence. In case of scaling one expects:

$$\nu_0(T) = \left(\frac{T}{T_0}\right)^{\kappa} \tag{3.22}$$

where κ is the (transport) critical exponent and T_0 a phenomenological fit parameter.

3.5. Exactly solvable problem

For an absolutely homogeneous sample, the 4-probe resistance can be calculated by solving the Laplace equation imposing boundary conditions, which follow from the geometry of the sample and the positions of the contacts. Significant progress in this direction was achieved in the fifties of the previous century [67, 68, 69, 70].

In general, the transport properties of inhomogeneous samples are much more difficult to analyze. This is mainly due to the spatial dependence of coefficients in the corresponding partial differential equation, which is not of the Laplace type anymore. A straightforward way to deal with inhomogeneities is

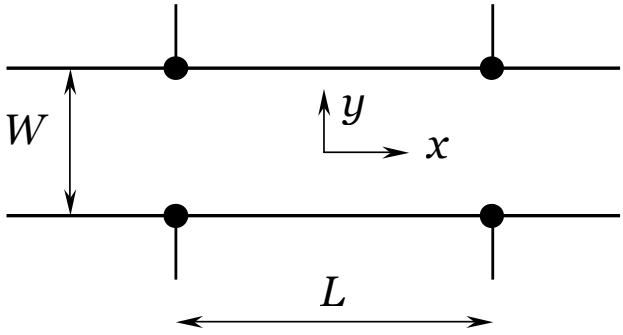

Figure 3.6: Sketch of the sample in the form of an infinite strip, used for the exact calculation of the 4-point resistance at the PI transition.

to solve the problem numerically, as is done in Chapter 7. Although numerical results are very useful in practice, they certainly do not give the same level of confidence as regards generality, as the analytical solution of the problem. The PI transition, however, represents a unique situation, where the analytical solution still can be obtained for one particular sort of inhomogeneities, namely a gradient of the electron density in an arbitrary direction. This is possible, because of the very specific dependence of the longitudinal and Hall resistivities on the filling factor. According to Eqs. (3.13)-(3.15) at $\overline{\nu} = 0$ (the PI transition):

$$\rho_{xx} = \frac{h}{e^2} \exp[-\frac{\nu - \nu_c}{\nu_0(T)}], \quad \rho_{xy} = \frac{h}{e^2} \tag{3.23}$$

Qualitatively, the advantages of such dependencies can be explained in the following way. The spatially dependent terms in the differential equation are proportional to the derivatives $d\rho_{xy}/d\nu$ and $d\rho_{xx}/d\nu$ divided by ρ_{xx}. Since at the PI transition, ρ_{xy} does not depend on ν and $d\rho_{xx}/d\nu \propto \rho_{xx}$, all spatially dependent terms turn out to be zero or a constant. This simplifies the problem in a crucial way. Although the final equation is still not as simple as the Laplace equation, the analytical solution can be obtained for certain boundary conditions [71].

Now let us consider the problem in more details. As sample we take an infinitely long conducting strip of width W with four potential point contacts as shown in Fig. 3.6. The distance between the two contacts on the top or bottom side of the sample is L. The strip carries a current J. In general, due to inhomogeneities, the values of the longitudinal 4-point resistances measured at the top and bottom pair of contacts, R^t_{xx} and R^b_{xx}, can be different. The same is true for the Hall resistances R^l_{xy} and R^r_{xy} measured at the left and right pair of Hall contacts.

To derive the 4-point resistance for the Hall bar with a density gradient, we start with the condition for having a stationary state $\partial\mathbf{B}/\partial t = \nabla \times \mathbf{E} = 0$ and the equation for charge conservation $\nabla \cdot \mathbf{j} = 0$ in 2-dimensional space (x-y plane). In order to satisfy the charge conservation law, we search a solution in the form of a current potential ϕ, such that $(j_x, j_y) = (\partial_y\phi, -\partial_x\phi)$ or, equivalently, $\mathbf{j} = \nabla \times (\mathbf{z}\,\phi)$, where $\mathbf{z}$ is the unit vector perpendicular to the x-y plane. Since $\boldsymbol{E = \rho j}$, where $\boldsymbol{\rho}$ is the resistivity tensor, the condition for a stationary state leads to the partial differential equation:

$$\Delta\phi = -\frac{1}{\rho_{xx}}\left[(\partial_x\rho_{xx} - \partial_y\rho_{xy})\partial_x + (\partial_y\rho_{xx} + \partial_y\rho_{xy})\partial_y\right]\phi \tag{3.24}$$

According to Eq. (3.23) ρ_{xx} is a function of the local filling factor ν only (if T is fixed), while ρ_{xy} is a constant. The spatial dependence of the longitudinal resistivity therefore, enters the problem via a spatial dependence of ν, which, in case of a gradient, varies linearly across the sample as:

$$\nu(x,y) = \nu_{aver}\left(1 + x\frac{\Delta n_x}{nL} + y\frac{\Delta n_y}{nW}\right) \tag{3.25}$$

where ν_{aver} and n are the averaged filling factor and averaged carrier density, respectively, Δn_x is the density difference between top and bottom edges of the sample and Δn_y is the density difference between potential contacts on the same edge. The last two expressions allow us to find all partial derivatives in Eq. (3.24):

$$\partial_x\rho_{xy} = \partial_y\rho_{xy} = 0, \tag{3.26}$$

$$\partial_x\rho_{xx} = -\frac{\nu_{aver}}{\nu_0(T)}\frac{\Delta n_x}{nL}\rho_{xx}, \tag{3.27}$$

$$\partial_y\rho_{xx} = -\frac{\nu_{aver}}{\nu_0(T)}\frac{\Delta n_y}{nW}\rho_{xx}, \tag{3.28}$$

which after substitution bring us to the much simpler differential equation with all coefficients constant:

$$\Delta\phi = \frac{\nu_{aver}}{n\nu_0(T)}\left[\frac{\Delta n_x}{L}\partial_x + \frac{\Delta n_y}{W}\partial_y\right]\phi \tag{3.29}$$

The boundary conditions require $j_y = 0$ at the edges, implying that the current can not cross the edge. In terms of the current potential, it can be expressed as:

$$\partial_x\phi = 0, \quad y = \pm W/2 \tag{3.30}$$

The solution of Eq. (3.29) with boundary conditions given by Eq. (3.30) is an exponential function:

$$\phi(x,y) = \phi_0 \exp(\alpha_y y), \quad \alpha_y = \frac{\nu_{aver}\Delta n_y}{nW\nu_0(T)} \tag{3.31}$$

where ϕ_0 is proportional to the total current through the sample. The current density is:

$$j_x = \partial_y \phi = \phi_0 \alpha_y \exp(\alpha_y y), \;\; j_y = -\partial_x \phi = 0 \tag{3.32}$$

This last expression shows that the current flows parallel to the edges. The current density does not depend on Δn_x, which means that the density gradient in the x-direction does not create inhomogeneities in the current distribution at the PI transition[3]. The remaining part of the calculations is straightforward. The electric field is the product of the resistivity tensor and the current density:

$$E_x = \rho_{xx} j_x + \rho_{xy} j_y, \quad E_y = -\rho_{xy} j_x + \rho_{xx} j_y. \tag{3.33}$$

The voltage between the two potential contacts can be obtained by integrating the electric field along the line connecting the contacts:

$$V^{t,b} = \int_{-L/2}^{L/2} E_x(x, \pm W/2) dx, \tag{3.34}$$

$$V^{r,l} = \int_{-W/2}^{W/2} E_y(\pm L/2, y) dy \tag{3.35}$$

where the superscripts t, b, r and l stand for top, bottom, right and left pair of contacts, respectively. After dividing the voltage by the total current $J = \int_{-W/2}^{W/2} j_x dy = 2\phi_0 \sinh(\alpha_y W/2)$ one can obtain the corresponding 4-point resistances:

$$R_{xx}^{t,b} = \frac{L}{W} \rho_{xx}(\nu_{aver}) N(\nu_{aver}), \quad R_{xy}^{r,l} = \frac{h}{e^2} \tag{3.36}$$

where the function $N(\nu_{aver})$ can be considered as a correction to the well-known formula $R_{xx} = (L/W)\rho_{xx}$ for an homogeneous Hall bar. The exact expression for $N(\nu_{aver})$ is:

$$N(\nu_{aver}) = \frac{\sinh(g_x)}{g_x} \cdot \frac{g_y}{\sinh(g_y)}, \tag{3.37}$$

[3]This last statement is true *only* for the PI transition. At the PP transition, a small density gradient in the x-direction is responsible for a variation of j_x in the y-direction (see Section 4.2).

where the parameters g_x and g_y are proportional to the averaged filling factor and density gradient along the corresponding axis:

$$g_x = \frac{1}{2}\frac{\Delta n_x}{n} \cdot \frac{\nu_{aver}}{\nu_0(T)}, \qquad g_y = \frac{1}{2}\frac{\Delta n_y}{n} \cdot \frac{\nu_{aver}}{\nu_0(T)}. \tag{3.38}$$

4

PLATEAU-PLATEAU TRANSITIONS AND DENSITY GRADIENTS

Even 25 years after the discovery of the quantum Hall effect (QHE) by von Klitzing *et al.* [1], the nature of the transitions between adjacent plateaus in the QHE is still a subject of intense debates. In the early days of the QHE, the main obstacle for systematic studies of inter-plateaux transitions was the poor quality of the samples. However, already two years after von Klitzing's discovery, measurements on GaAs/AlGaAs heterostructures revealed an impressive sharpness of plateau-plateau (PP) transitions at low temperatures [8]. This led theoreticians to consider the QHE as an example of a quantum phase transition (QPT) [10]. The first experimental evidence in support of the idea of a QPT was given by Wei *et al.* [14], who studied the temperature dependence of several PP transitions in an InGaAs/InP heterostructure. The experimental paper of Wei and co-workers triggered an enormous activity in the field, although it was not clear at that time whether the investigated sample was homogeneous enough to assure a correct value of the critical exponent κ. Doubts were raised by several groups [72], [73], [74],[75] who tried to reproduce the results of Wei *et al.*on different samples, but obtained a whole range of sample dependent exponents $\kappa = 0.3 - 0.9$ instead of the "universal" $\kappa = 0.42$ proposed by Wei *et al.*.

In parallel with the experimental investigations of quantum Hall systems, significant progress was achieved in modelling of the QHE. Here, we would like to mention only those theoretical results, which are related to ex-

periments described in this chapter, namely, (i) the universal semicircle relation between components of the local conductivity tensor [19] and (ii) the scaling theory of the quantum Hall effect [10]. Furthermore we make use of the work of Oswald, Span and Kuchar, who put forward explicit expressions for the components of the resistivity tensor as a function of the filling factor [61], as given in Eqs. (3.13)-(3.15)

A common mistake (or rather a crude approximation) made in the vast majority of experimental papers dealing with critical behavior of the QHE is the use of the standard equation:

$$\rho_{xx} = \frac{W}{L} R_{xx} \tag{4.1}$$

where ρ_{xx} and R_{xx} are longitudinal resistivity and 4-point resistance respectively, W is the width of the Hall bar and L is the distance between the voltage contacts. The point we would like to stress here is that Eq. (4.1) can be used only if the sample is completely homogeneous, *i.e.* with the same value of ρ_{xx} at each point. In real samples, as we will show in this chapter, this is rarely the case. The situation is worse at lower temperatures, because in the limit $T \to 0$ the components of the resistivity tensor are discontinuous functions of the magnetic field and the carrier density. Associating the experimentally measured quantity $\frac{W}{L} R_{xx}$ with the theoretically calculated local resistivity ρ_{xx}, leads to mistakes, which in the end may give rise to a wrong value of the critical exponent (see Chapter 7).

In this chapter, we present results of experiments on PP transitions measured on various 2-dimensional semiconductor structures. Special attention is given to the importance of inhomogeneities. The most significant experimental finding is the "reflection symmetry" of the longitudinal resistance, described in Section 4.1.

A qualitative explanation of this phenomenon is given in Section 4.2, where the reflection symmetry is attributed to a gradient of the electron density along the Hall bar and therefore related to sample inhomogeneities.

In Section 4.3, we show that illumination of the sample enhances homogeneity of the sample. We also demonstrate how to treat the transport data in order to decrease the influence of inhomogeneities and, if possible, how to disentangle the effects of density gradients from the intrinsic behavior . It is also demonstrated how an almost ideal semicircle on the $\sigma_{xx}(\sigma_{xy})$ plot can be recovered from transport data using a proper averaging procedure.

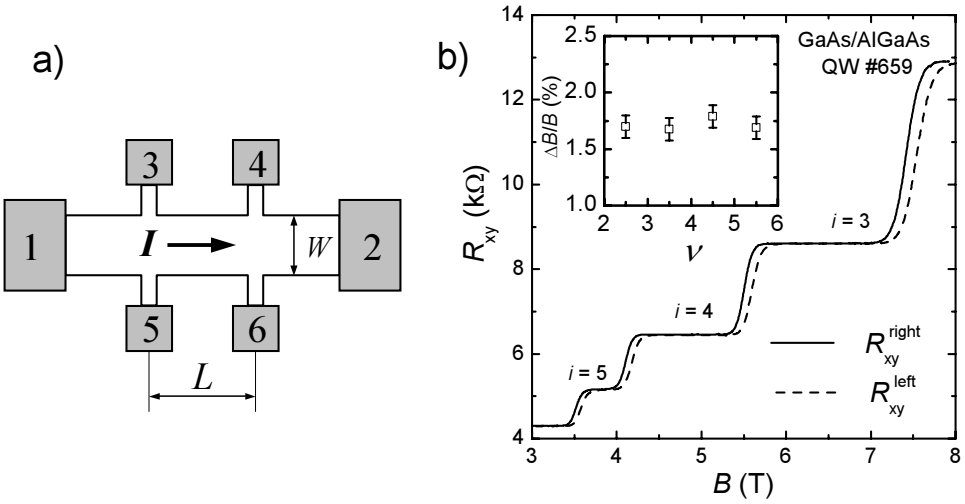

Figure 4.1: a) Schematic picture of a Hall bar. L denotes the distance between the longitudinal voltage contacts and W is the channel width. b) Two Hall resistances $R_{xy}^{right}(B)$ and $R_{xy}^{left}(B)$ measured simultaneously on the right and left pairs of contacts on sample #659 (GaAs/AlGaAs QW) at $T = 0.4K$. Inset shows the relative distance $\Delta B/B$ between two curves in the main figure *versus* filling factor ν, from which the density difference $\Delta n/n = \Delta B/B \approx 1.7\%$ was extracted.

4.1. Experimental observation of reflection symmetry

Most of the time magnetotransport measurements are performed on samples in the form of a Hall bar, which is schematically shown in Fig. 4.1. For a homogeneous sample two current and three voltage contacts are sufficient to determine the longitudinal and transverse resistivities. If L and W are the sample dimensions as shown in Fig. 4.1 and I is the current flowing between contacts 1 and 2, then the components of the resistivity tensor can be calculated from:

$$\rho_{xx} = \frac{W}{L}\frac{V_{xx}}{I}, \quad \rho_{xy} = \frac{V_{xy}}{I} \tag{4.2}$$

where V_{xx} and V_{xy} are the longitudinal and transverse (Hall) voltages, measured at the corresponding contacts. V_{xx} is measured at the contact pairs 3-4 or 5-6, while V_{xy} is measured at 3-5 or 4-6. If the sample is completely homogeneous, there is no reason to expect any difference between V_{34} and V_{56}, where the subscripts indicate the contacts at which voltage is measured. In contrast, if inhomogeneities are present on a scale comparable or larger than the sample

Sample	$L \times W$, $(\mu m)^2$	Illumination	n (10^{11} cm^{-2})	$\Delta n/n$
GaAs/AlGaAs	1260×1000	before	4.7	0.017
#659		after	6.1	0.0025
GaInAs/AlInAs	387×75	before	1.8	0.014
31232-#3		after	3.6	0.006
GaInAs/AlInAs	387×75	before	2.2	0.018
31232-#2				

Table 4.1: Transport parameters of Hall bars, prepared from different semiconductor structures, before and after illumination: L and W are sample dimensions according to Fig. 4.1a, n is the electron density and $\Delta n/n$ is the density difference measured at different pairs of Hall contacts.

size, the voltages at the top and bottom pairs of contacts are likely different. This difference can be used for extracting information about the inhomogeneities.

Magnetotransport experiments have been performed on two different semiconductor structures: a high-mobility ($\mu \sim 300000$ cm^2/Vs) GaAs/AlGaAs quantum well and a low-mobility ($\mu \sim 20000$ cm^2/Vs) GaInAs/AlInAs quantum well. The electron densities for our samples were fairly low ($n = 1.8 - 6.1 \times 10^{11}$ cm^{-2}), such that all samples showed distinct quantum Hall features within the magnetic field range $B \leq 8$ T. The sizes and electron densities of the samples are listed in Table 4.1. In some cases the electron density was increased by illumination with a LED at $T = 4.2$ K. The samples were selected such that no carrier relaxation occurred during the measurements. All longitudinal and transverse resistances were measured simultaneously, using standard lock-in techniques at a frequency of 13 Hz. The excitation current ranged from 5 to 50 nA to avoid Joule heating. The data presented in this Section were all taken at $T = 0.4$ K.

In Fig. 4.1b we show the Hall resistance between 3 and 8 T, before illumination, of the GaAs/AlGaAs quantum well (sample #659) measured at the left (3-5) and right (4-6) contact pairs across the Hall bar: $R_{xy}^{left} = V_{35}/I$ and $R_{xy}^{right} = V_{46}/I$. Upon reversing the magnetic field, R_{xy}^{left} and R_{xy}^{right} stay identical, except for the change of sign as it should:

$$R_{xy}^{left}(B) = -R_{xy}^{left}(-B), \quad R_{xy}^{right}(B) = -R_{xy}^{right}(-B), \tag{4.3}$$

This implies that misalignment of the Hall contacts is negligible, otherwise

we should see in the R_{xy} data an additional contribution from ρ_{xx}, which is even function of magnetic field and, therefore, has to violate Eq. (4.3). The PP transitions measured at contacts 4-6 are shifted along the field axis with respect to those at contacts 3-5. This is due to different local filling factors, $\nu(x,y) = \frac{he}{B} n(x,y)$. Assuming a constant magnetic field B over the sample, the spatial distribution of filling factors matches that of the electron density $n(x,y)$. Hence the filling factor between contacts 3-5 is always larger than the one between 4-6. However, their ratio is field independent and equal to the ratio of local densities. This is corroborated by the insert in Fig. 4.1b, where we have traced the experimental values of the shift $\Delta B/B$, measured halfway the PP transitions, versus filling factor $2 < \nu < 6$. The extracted carrier density difference is $\Delta n/n = \Delta B/B \approx 0.017$. We use here the words "local" density, or "local" filling factor, in the sense that the Hall contacts probe a sample region with dimension W, which is smaller than the distance L between the two pairs of Hall contacts. In contrast, the longitudinal resistance measured between contacts 3-4 or 5-6 is an "averaged" one. This does not mean that in real samples the concentration of carriers between contacts 3 and 5 is a constant. However for simplicity of our model at this stage, we assume that the electron density $n(x,y)$ is a smooth function of position and that all changes can be adequately described by a small gradient along the Hall bar.

From the simple experiment presented in Fig. 4.1b we conclude: a) even samples with broad plateaux may contain carrier inhomogeneities of the order of 1-2%; b) a smooth spatial variation of the electron density can be detected in transport measurements.

Next, in Fig. 4.2 we present the longitudinal resistances $R_{xx}^{top} = V_{34}/I$ and $R_{xx}^{bot} = V_{56}/I$ of the same sample #659, measured at top and bottom sides of the Hall bar. Data are taken for both positive ($B \uparrow$) and negative ($B \downarrow$) field polarities ($|B| \leq 8$ T). The curves show the familiar Shubnikov-de Haas oscillations at low fields and the resistance peaks associated with the PP transitions in the quantum Hall regime at higher fields. For a homogeneous Hall bar we expect $R_{xx}^{bot} = R_{xx}^{top}$, which is clearly not the case here. Instead there is a large difference in the peak values R_{xx}^{bot} and R_{xx}^{top}, which amounts up to 50% for the $3 \rightarrow 2$ PP transition. Moreover, a close inspection of Fig. 4.2 shows that R_{xx}^{top} for $B \uparrow$ equals R_{xx}^{bot} for $B \downarrow$ and *vice versa* to within 1%. We conclude that the longitudinal resistance when measured on both sides of the Hall bar shows a remarkable *reflection symmetry*:

$$R_{xx}^{top}(\pm B) = R_{xx}^{bot}(\mp B). \tag{4.4}$$

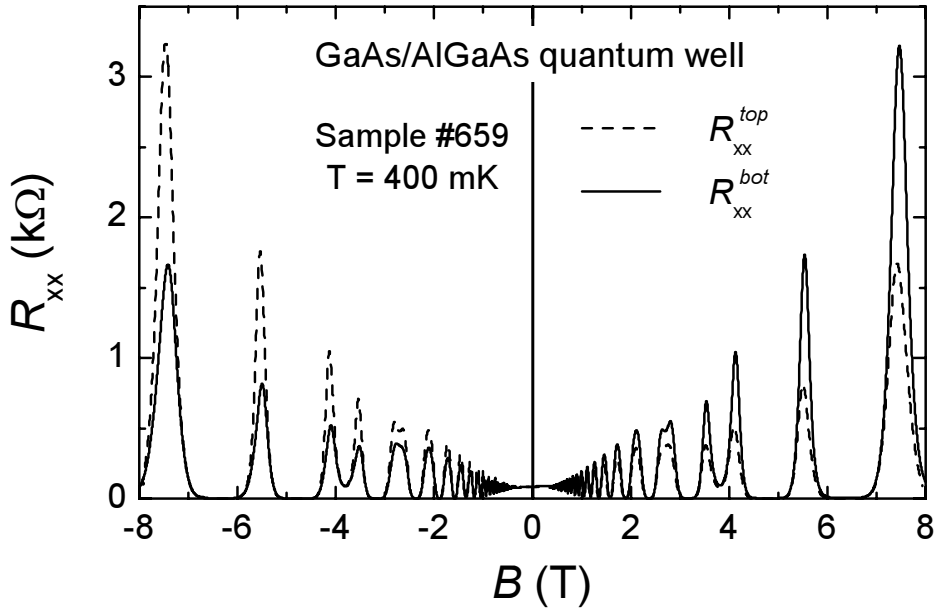

Figure 4.2: The longitudinal resistances $R_{xx}^{top}(B)$ (dashed line) and $R_{xx}^{bot}(B)$ (solid line) of sample #659 for positive and negative polarities of the magnetic field. One curve can be transformed into the other by reversing the magnetic field polarity.

Magnetotransport data for another sample - the GaInAs/AlInAs quantum well - are shown in Fig. 4.3. From the Hall measurements we extract $\Delta n/n = 0.014$. The difference between R_{xx}^{top} and R_{xx}^{bot} is not as pronounced as for the GaAs/AlGaAs quantum well, but nevertheless significant.

4.2. Explanation of reflection symmetry

In the previous Section we showed that upon reversing the polarity of the magnetic field, the longitudinal resistances measured at the top and bottom sides of the Hall bar, R_{xx}^{top} and R_{xx}^{bot}, interchange. A difference in resistances measured at opposite contact pairs is not an unusual phenomenon and is generally attributed to sample inhomogeneities. However, the interchange of R_{xx}^{top} and R_{xx}^{bot} upon field reversal cannot be accidental and requires a non-trivial explanation.

In the following, we show that the observed symmetry can be accounted for by a small carrier density gradient, which is present in general in any sample and can be determined from measurements of the Hall resistances. We start with a qualitative explanation. The derivation of the reflection symmetry (for a special case and with some additional assumptions) is presented at the end of

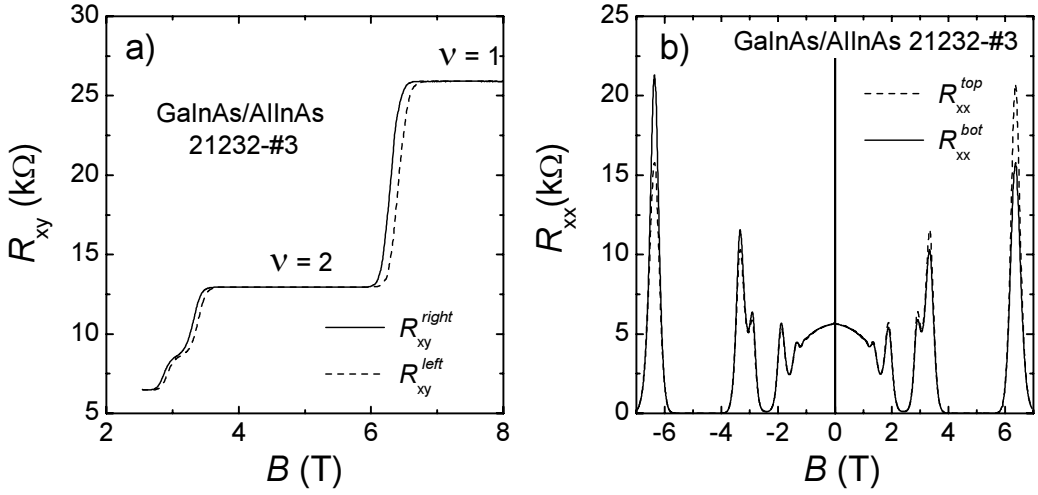

Figure 4.3: a) Hall resistance as a function of magnetic field for the GaInAs/AlInAs quantum well (21232-#3 - no illumination) between plateaux $\nu = 1$ and $\nu = 4$ at $T = 0.4$ K. The solid and dashed lines show data taken at the right and left Hall contact pairs; b) Longitudinal resistivity as a function of magnetic field ($B \uparrow$ and $B \downarrow$) for the GaInAs/AlInAs quantum well (21232-#3 - no illumination) at $T = 0.4$ K. The solid and dashed lines show data taken at contact pairs located at the top and bottom side of the Hall bar.

the Section.

Let us assume that the carrier density gradient points from the left current contact to the right one. In this case, R_{xy}^{left} and R_{xy}^{right} are slightly different. We define:

$$\Delta R_{xy} = R_{xy}^{right} - R_{xy}^{left}, \tag{4.5}$$

and for the difference in the longitudinal resistances measured at both sides of the Hall bar:

$$\Delta R_{xx} = R_{xx}^{top} - R_{xx}^{bot}. \tag{4.6}$$

For a perfect homogeneous Hall bar $\Delta R_{xy} = 0$ and $\Delta R_{xx} = 0$. However, since

$$\begin{aligned} \Delta R_{xy} = ((\varphi_3 - \varphi_5) - (\varphi_4 - \varphi_6))/I = \\ ((\varphi_3 - \varphi_4) - (\varphi_5 - \varphi_6))/I = \Delta R_{xx}, \end{aligned} \tag{4.7}$$

where φ_i is the potential at contact i, a finite ΔR_{xy} immediately implies a difference between the longitudinal resistances measured at the top and bottom side of the Hall bar, $\Delta R_{xx} \neq 0$. Because the Hall voltage is an odd function of B, reversing the field polarity changes the sign of ΔR_{xy} and subsequently ΔR_{xx}:

$$\Delta R_{xy}(-B) = -\Delta R_{xy}(B), \tag{4.8}$$

and

$$\Delta R_{xx}(-B) = -\Delta R_{xx}(B). \tag{4.9}$$

Thus ΔR_{xx} is an odd function of B, which holds under the conditions of Eq. (4.4).

A second qualitative explanation of Eq. (4.4) can be given considering the symmetry of the problem. The Hall bar with a gradient along the direction of the current flow has an axis of symmetry parallel to the direction of the gradient. Therefore, reversing the polarity of the magnetic field is equivalent to flipping the sample: the top pair of contacts becomes the bottom pair and *vice versa*, which is exactly what Eq. (4.4) is about.

With some simplifications of the initial problem the reflection symmetry in the QHE can be derived analytically. We start from the usual equations for transport coefficients of an infinitely long homogeneous conducting strip along the x-axis, where an uniform current density j_x results in the electric field:

$$E_x = \rho_{xx} j_x, \quad E_y = \rho_{xy} j_x. \tag{4.10}$$

Here $j_y = 0$ and ρ_{xx} and ρ_{xy} are the longitudinal and Hall resistivity for a perfectly homogeneous sample. Now consider what happens if we add a small gradient parallel to the x-axis in the electron density. In this case the filling factor ν also changes linearly in x due to a gradient: $\nu(x, y) = \frac{he}{B} n(x, y)$. At the PP transition the Hall resistivity slopes from one Hall plateau to the other, while the longitudinal resistivity forms a peak, so that $|\partial\rho_{xy}/\partial B| \gg |\partial\rho_{xx}/\partial B|$ near the maximum of ρ_{xx}. As such, an x-dependence of the local filling factor $\nu(x)$ therefore mainly affects the electric field component E_y:

$$E_x = \rho_{xx} j_x, \quad E_y = (\rho_{xy} + \alpha x) j_x, \quad \alpha = \frac{\partial\rho_{xy}}{\partial\nu}\frac{\partial\nu}{\partial x}. \tag{4.11}$$

This result, however, violates an important condition for having a stationary state, *i.e.* the electric field must be rotation free $\nabla \times \mathbf{E} = 0$. To satisfy this condition we proceed by inserting a y-dependent current density:

$$j_x(y) = j_{x0}(1 + \alpha y/\rho_{xx}). \tag{4.12}$$

Working to linear order in the coordinates x and y we can write

$$E_x = (\rho_{xx} + \alpha y) j_{x0}, \quad E_y = (\rho_{xy} + \alpha x + \alpha\tfrac{\rho_{xy}}{\rho_{xx}} y) j_{x0}, \tag{4.13}$$

which are the appropriate equations for the PP transition. Notice that the stationary state condition $\nabla \times \mathbf{E} = 0$ and charge conservation $\nabla \cdot \mathbf{j} = 0$ are satisfied.

With a width of the strip W and distance between the potential contacts L, the longitudinal resistance at the top and bottom and the Hall resistance at the left and right contacts of the Hall bar are given by

$$R_{xx}^{top} = V_{34}/I_x = \frac{L}{W}(\rho_{xx} + \alpha\frac{W}{2}), \tag{4.14}$$

$$R_{xx}^{bot} = V_{56}/I_x = \frac{L}{W}(\rho_{xx} - \alpha\frac{W}{2}), \tag{4.15}$$

$$R_{xy}^{left} = V_{35}/I_x = (\rho_{xy} - \alpha\frac{L}{2}), \tag{4.16}$$

$$R_{xy}^{right} = V_{46}/I_x = (\rho_{xy} + \alpha\frac{L}{2}), \tag{4.17}$$

where we take zero coordinates (x, y) in the center of the strip between the potential contacts. When $B \to -B$, ρ_{xy} and α change sign, but ρ_{xx} remains unchanged. The results therefore explain the observed symmetry at the PP transition, $R_{xx}^{bot}(\pm B) = R_{xx}^{top}(\mp B)$. Notice that with this specific form of α, Eqs. (4.16)-(4.17) can be regarded as a Taylor expansion of the local Hall resistance ρ_{xy} at values $x = \pm L/2$. It is also important to stress, that Eqs. (4.14)-(4.17) are obtained in the linear approximation and are valid only around the maximum of ρ_{xx}.

4.3. Dealing with inhomogeneities and recovery of semicircle

In the course of this work we realized through discussions with other experimentalists working in this field that the reflection symmetry reported in Section 4.1 is a rather common feature often seen in measurements of QHE on Hall bars. However, there is a certain confusion in the community about the origin of the symmetry. Quite similar result compared to those presented in Section 4.1 were reported in connection with edge currents [76, 77]. The Hall bar used for the experiment in Ref. [76] had a very special geometry and a symmetry in the magnetoresistance was attributed to a non-equilibrium population of edge states due to the proximity of potential and current contacts. This is clearly not the case for the Hall bars used in our experiments. To the best of our knowledge there is only one publication were reflection symmetry is linked to the gradient of the carrier density [78]. In this paper, a fairly large gradient, which results in a 10 % density difference between the potential contacts, produces an effect similar to that shown in Fig. 4.2. However, strictly speaking the

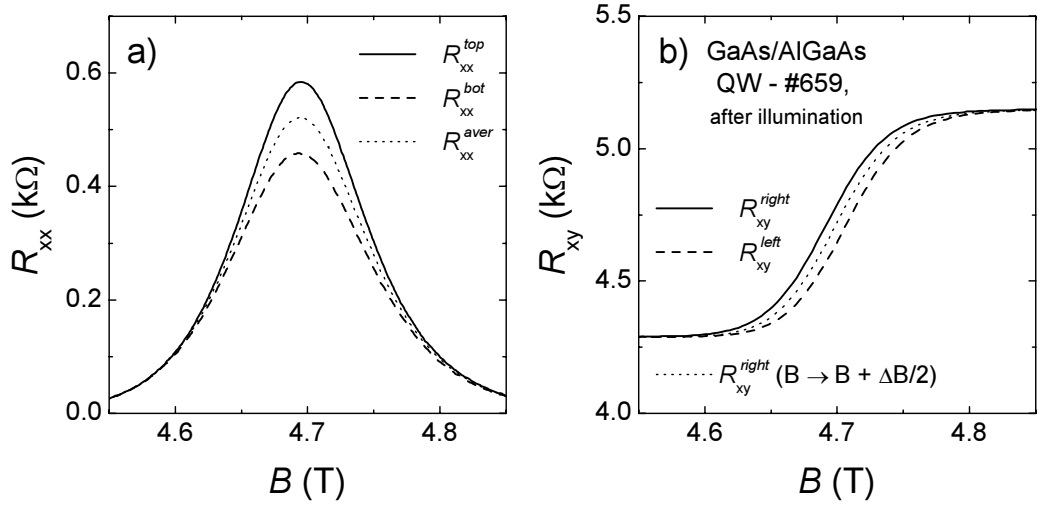

Figure 4.4: Longitudinal resistivity (a) and Hall resistance (b) of the GaAs/AlGaAs quantum well (#659) after illumination ($T = 0.4$ K). Data are shown for the $i = 6 \rightarrow 5$ plateau-plateau transition.

curves in Ref. [78] are not really symmetric, perhaps, due to other imperfections in the sample. In any case, this idea was not further worked out and the effect of density gradients was not taken into account by researchers who studied critical behavior in quantum Hall systems.

In this Section, we demonstrate how the disturbing effect of a density gradient can be reduced and even in some cases be eliminated, thereby, revealing the fundamental properties of the quantum Hall effect, such as the semicircle in the $\sigma_{xx}(\sigma_{xy})$ diagram.

To reduce the carrier gradient we illuminate the sample with an infra-red LED. Illumination is a well known method for increasing the carrier density of the 2DEG. Although not all semiconductor structures are light sensitive and in some cases illumination may cause parallel conductivity, this method is much easier to implement than making high quality gates. The initial purpose of this experiment was to study the (in)dependence of the critical exponent on the carrier concentration. We found, however, that illumination not just increases the electron density of the 2DEG, but also makes the sample more homogeneous. Magnetotransport data, after illumination, near the $6 \rightarrow 5$ PP transition are shown in Fig. 4.4. The carrier density increases from 4.7 to 6.1×10^{11} cm^{-2}, while the carrier difference decreases to $\Delta n/n \approx 0.003$. The longitudinal resistance still remains antisymmetric, but the effect is now much smaller and amounts to only 20% for the $6 \rightarrow 5$ PP transition. A decrease of the density gra-

dient upon illumination was also found in the GaInAs/AlInAs quantum well (see Table 4.1).

Next we compare the data before and after illumination with some of the theoretical predictions for transport coefficients. First, we consider the relationship between σ_{xx} and σ_{xy}, which should obey a universal semicircle law according to the model developed in Ref. [19]. The conductivities can be obtained from the resistivities in the standard manner:

$$\sigma_{xx} = \frac{\rho_{xx}}{\rho_{xx}^2 + \rho_{xy}^2}, \quad \sigma_{xy} = \frac{\rho_{xy}}{\rho_{xx}^2 + \rho_{xy}^2}. \tag{4.18}$$

The experiment gives us two different "longitudinal resistivities" $\rho_{xx}^{top} = \frac{W}{L} R_{xx}^{top}$ and $\rho_{xx}^{bot} = \frac{W}{L} R_{xx}^{bot}$ and two different "Hall resistivities" $\rho_{xy}^{left} = R_{xy}^{left}$ and $\rho_{xy}^{right} = R_{xy}^{right}$. Combining these, four different $\sigma_{xx}(\sigma_{xy})$ curves can be obtained, see Fig. 4.5. Clearly, none of these is a true semicircle. Especially, the data measured before illumination suffer from huge distortions (Fig. 4.5a). After illumination the sample becomes more homogeneous and the difference between the $\sigma_{xx}(\sigma_{xy})$ curves decreases (Fig. 4.5b), revealing a clear tendency towards the expected theoretical behavior. Since the origin of the deviations is known, we can try to eliminate the effect of the density gradient on the $\sigma_{xx}(\sigma_{xy})$ diagram. To do so, we first calculate the average longitudinal resistance:

$$R_{xx}^{ave} = \frac{1}{2}(R_{xx}^{top} + R_{xx}^{bot}), \tag{4.19}$$

which is now an even function of the magnetic field:

$$R_{xx}^{ave}(B) = R_{xx}^{ave}(-B). \tag{4.20}$$

The averaged curve is shown as the dotted line in Fig. 4.4a. Next, we obtain the corrected Hall resistivity. Simple averaging will not give the best result, because this affects the slope of the transition. To keep the same slope we shift the experimental curve $R_{xy}^{left}(B)$ to the right along the B-axis by $\Delta B/2$, where ΔB is the distance between $R_{xy}^{left}(B)$ and $R_{xy}^{right}(B)$. Shifting can be considered as averaging of the electron density rather than the resistance values. The corrected data are shown as the dotted line in Fig. 4.4b. Basically, the same result can be obtained by shifting the curve $R_{xy}^{right}(B)$ to the left by the same amount $\Delta B/2$. After averaging, a new $\sigma_{xx}(\sigma_{xy})$ diagram was constructed. The result is presented in Fig. 4.5c together with the theoretical semicircle. The agreement is almost perfect. To the best of our knowledge, such a coincidence of theory and

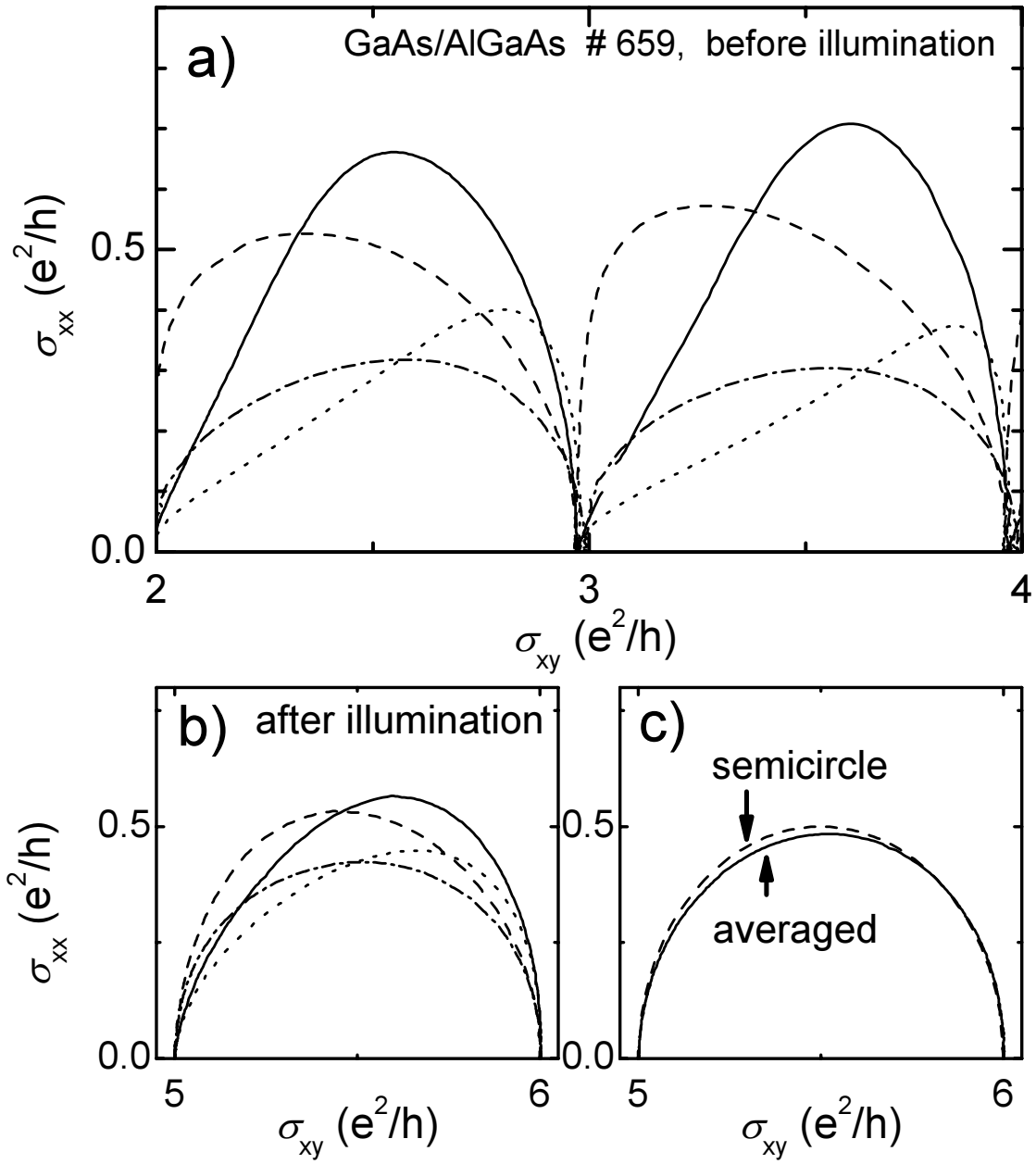

Figure 4.5: (a) The longitudinal conductance σ_{xx} as a function of the Hall conductance σ_{xy} for the $4 \rightarrow 3$ and $3 \rightarrow 2$ PP transitions of the GaAs/AlGaAs quantum well before illumination ($T = 0.4$ K). The four different lines are obtained by using all possible combinations of ρ_{xx} and R_{xy} (b) Change of $\sigma_{xx}(\sigma_{xy})$ plot after illumination for the $5 \rightarrow 6$ PP transition. (c) The solid line represents the σ_{xx}, σ_{xy} data after averaging. The dashed line shows the "ideal" semicircle relation.

experiment has never been reported before for PP transitions. It is important to stress that by semicircle we mean not only the general shape of the diagram, but a true semicircle with the peak value of σ_{xx} exactly at $e^2/(2h)$.

To demonstrate that the semicircle behavior is universal and holds for other transitions, Fig. 4.6 shows the magnetoresistance data for the same sample #659 taken at base temperature of our dilution refrigerator. The lowest temperature was chosen in order to obtain as many resolved PP transition as possible. The distortions caused by the gradient become stronger at low temperatures, therefore the sample was intensively illuminated to reach a maximum possible carrier density ($n_e = 6.2 \times 10^{11}$ cm^{-2}). Each curve in Fig. 4.6a was taken from one pair of contacts for positive field only. From these, the $\sigma_{xx}(\sigma_{xy})$ diagram in Fig. 4.6b was constructed. It shows periodicity in σ_{xy} for all spin resolved PP transitions from $\nu = 4$ to $\nu = 10$. The "semicircles" are somewhat distorted to the left, all in the same fashion, due to inhomogeneities. Nevertheless, universality of the PP transitions is obvious. Even the fact that for the spin unresolved transition between $\nu = 12$ and $\nu = 14$ a semicircle is observed with a maximum of σ_{xx} twice higher than for the spin separated transitions is consistent with theory.

Illumination, however, cannot solve all inhomogeneity related problems. In case of the GaInAs/AlInAs quantum well, the peak value of the conductivity σ_{xx}^{max} at the $2 \rightarrow 1$ PP transition is about 0.35 e^2/h after illumination and averaging. It is not clear at present whether the smaller value of σ_{xx}^{max} in the GaInAs/AlInAs QW is related to inhomogeneities or has another physical reason. There is, however, a clear qualitative difference between the shapes of the PP transitions in the above-mentioned sample and the GaAs/AlGaAs QW discussed in the previous paragraphs. In the latter case, the curves $R_{xx}(B)$ are absolutely smooth at any T, while in the former case the magnetoresistance data reveal a reproducible fine structure (see also Chapter 2), which becomes stronger at low temperatures and might be related to quantum conductance fluctuations [79]. On the other hand, the data in Table 4.1 indicate that illumination is more effective in the case of the GaAs/AlGaAs QW. Therefore, the lower value of σ_{xx}^{max} for the InGaAs/InAlAs can be related to a higher remanent gradient (and other sorts of macroscopic inhomogeneities) after illumination.

The next step in understanding the PP transitions can be made by analyzing the shape of the transverse and longitudinal resistance as a function of filling factor. An explicit parameterization for $\rho_{xx}(\nu)$ and $\rho_{xy}(\nu)$ was proposed several years ago [61]. Expressions reproduced from the original paper [61] for

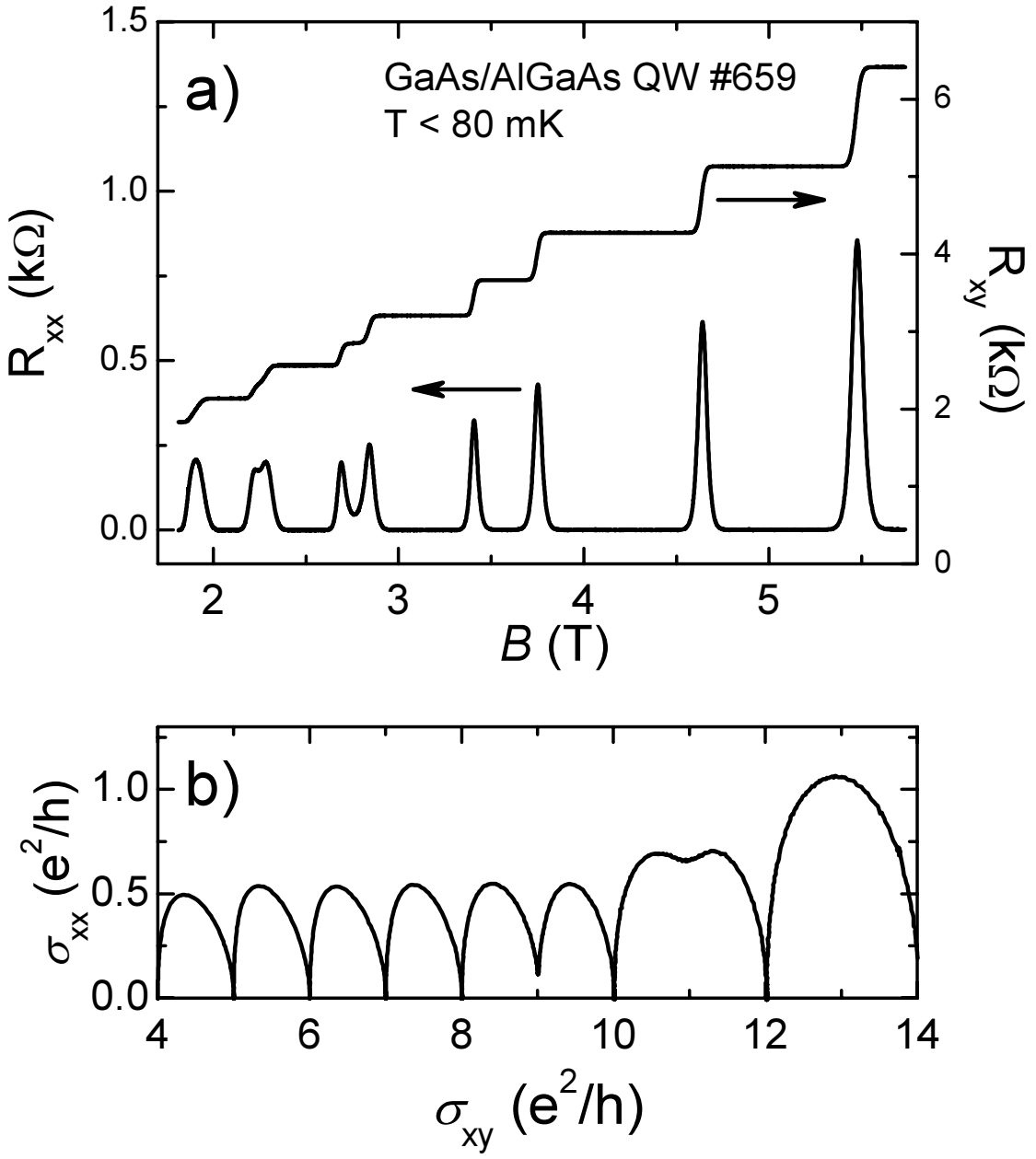

Figure 4.6: (a) The longitudinal and Hall resistances of a GaAs/AlGaAs quantum well after illumination at base temperature of the dilution refrigerator. (b) The diagram $\sigma_{xx}(\sigma_{xy})$ obtained from data shown in (a). Despite of distortions caused by inhomogeneities, σ_{xx} is a periodic function of σ_{xy} for all spin-resolved transitions. The peak value σ_{xx}^{max} is close to 0.5 e^2/h.

$\rho_{xx}(\nu)$ and $\rho_{xy}(\nu)$ are given in Eqs.(3.13)-(3.15). Besides ν, the equations contain the variable parameter $\nu_0(T)$, which is proportional to the PP transition width. The other parameters, ν_c and $\bar{\nu}$, are fixed. It is expected that the critical filling factor $\nu_c = \bar{\nu} + 1/2$, where $\bar{\nu}$ is the number of completely filled Landau levels. Therefore, in the ideal situation the experimental data can be fitted using only one fit parameter $\nu_0(T)$. In practice, however, one fit parameter is not sufficient. Problems arise again due to inhomogeneities. First of all, according to Eq. (3.19), the peak value of the longitudinal resistivity ρ_{xx}^{max} is temperature independent, which is almost never the case for the maximum of the longitudinal resistance obtained in experiment. Secondly, the curves $R_{xy}(B)$ measured at different contacts have PP transitions at slightly different fields as shown in Fig. 4.1b and 4.4b. Usually, the filling factor ν is calculated from the magnetic field using Eq. (1.6), where the density n is assumed to be constant across the sample. If the carrier density exhibits a gradient such an assumption is not correct, of course. Proceeding in this "standard" way we find that the critical filling factor ν_c at which the transition takes place is slightly different at different contacts. Therefore, at least one of them cannot attain a half-integer value. To overcome these problems, while keeping the description as simple as possible, we introduce two additional fitting parameters: ν_c, which in not necessarily equal to $\bar{\nu} + 1/2$ any more, and the dimensionless pre-factor R_0 in Eq. (3.13), which now can be written as:

$$\rho_{xx} = \frac{h}{e^2} \frac{R_0 P}{(\overline{\nu}+1)^2 + (\overline{\nu}P)^2}. \tag{4.21}$$

The parameter R_0 indicates how much the experimental peak value of the resistivity differs from the theoretical one. In the ideal case $R_0 = 1$. A similar procedure, with an extra fit parameter, has been used in Ref. [80], where the authors introduced a pre-factor σ^{pk} in order to fit the peak $\sigma_{xx}(\nu)$ with a temperature dependent maximum value.

We found that with the modification described in the previous paragraph, the expressions proposed in Ref. [61] follow the experimental data rather good. In Fig. 4.7a we show the longitudinal resistance of sample #659 taken from the top pair of contacts and normalized by the geometrical factor W/L. The data were taken after illumination. The density gradient reveals itself, among other things, by $R_0 = 1.14$, *i.e.* the peak value of the longitudinal resistivity is higher than the theoretical value $\rho_{xx}^{max} = \frac{1}{60} h/e^2$ by 14%. Nevertheless, the theoretical curve (4.21) fits the experimental data much better than other popular peak functions like a Lorentzian or Gaussian, which also have three fit

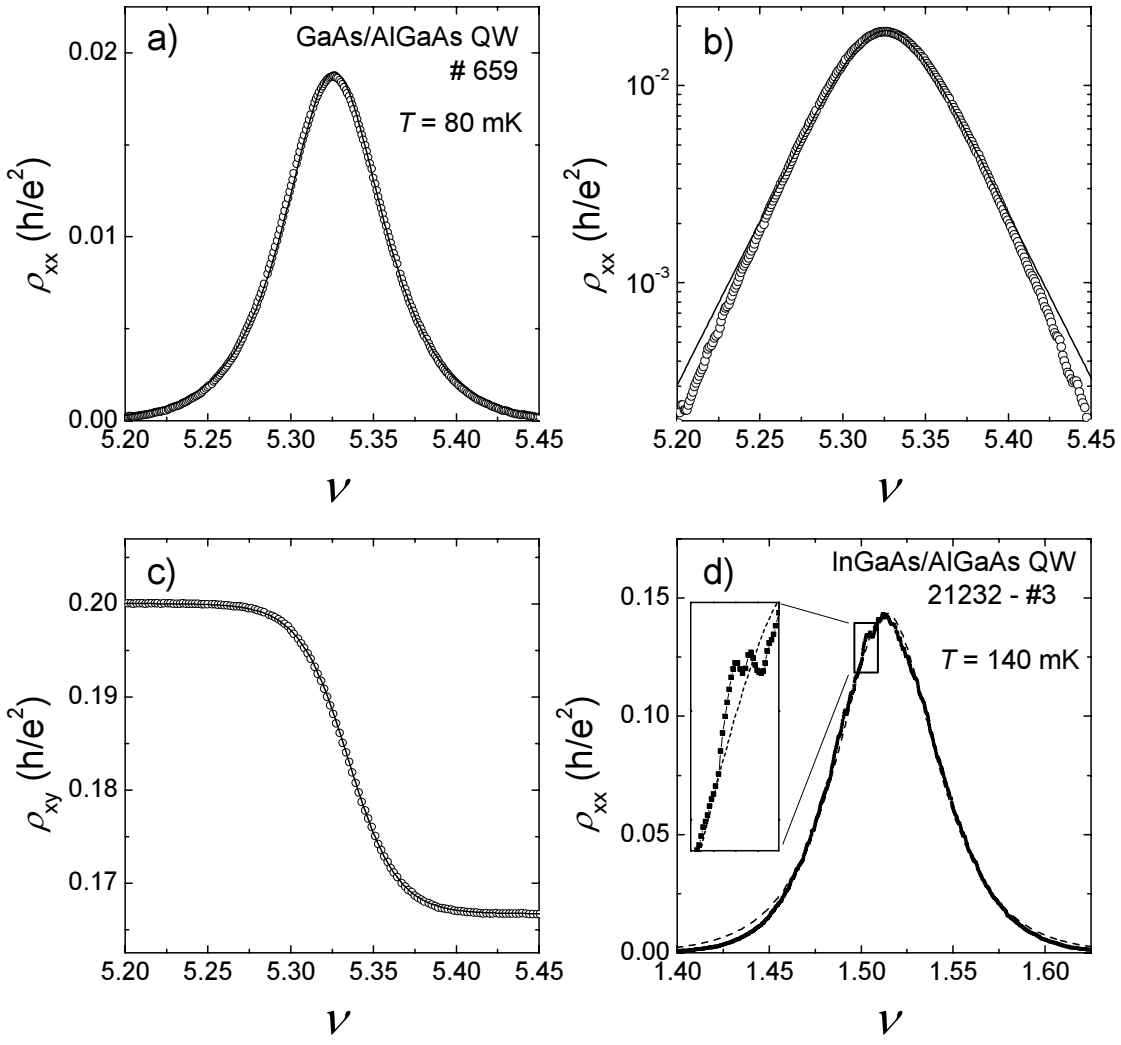

Figure 4.7: Experimental data for the PP transitions fitted with the functions Eqs. (3.14), (3.15) and (4.21): (a) The "longitudinal resistivity" ρ_{xx}^{top} of GaAs/AlGaAS QW at the $5 \rightarrow 6$ PP transition as a function of the filling factor (open symbols) and the fit (solid line). The extracted parameters are: $\nu_0 \approx 0.026$, $\nu_c = 5.33$ and $R_0 = 1.14$; (b) the same data as (a) presented on a logarithmic scale to show deviations from the theoretical behavior in the tales of the PP transition; (c) the "Hall resistivity" ρ_{xy}^{right} of the same GaAs/AlGaAs quantum well (open symbols). The solid line represents fit with parameters $\nu_0 \approx 0.029$ and $\nu_c = 5.34$; (d) Example of the $2 \rightarrow 1$ PP transition of an InGaAs/AlGaAs QW. The experimental curve (bold solid line) can still be fitted by the function Eq. (4.21) (dashed line), although it has a reproducible fine structure enlarged in the inset. The extracted parameters are: $\nu_0 \approx 0.024$, $\nu_c = 1.53$ and $R_0 = 0.57$.

parameters. The deviations appear mainly in the tails of the PP transition, as can be seen in Fig. 4.7b, where the same data set is shown on a logarithmic scale in order to enhance the difference. These deviations possibly can be attributed to inhomogeneities. Numerical simulations presented in Chapter 7 reveal very similar behavior at the tails of the PP transition in a sample with a density gradient. On the other hand, the deviations might be caused by limitations of the model. The authors of Ref. [61] assume that the longitudinal resistance at the PI transition is an exponential function of the filling factor: $\rho_{xx} = h/e^2 \exp(-X)$, where $X = (\nu - \nu_c)/\nu_0(T)$. Experiments on the PI transitions suggest, however, the presence of higher order terms of X in the exponential dependence of ρ_{xx} (Chapters 5 and 6). These additional non-linear terms might be responsible for the deviations as well. An experimental verification of this latter possibility is however unlikely for sample #659 as the PI transition takes place at ~ 50 T, a field that cannot be reached with continuous magnets yet. Other parameters extracted from the fitting procedure are $\nu_0 = 0.026$ and $\nu_c = 5.33$. The critical filling factor ν_c is considerably smaller than 5.5 (the expected half-integer value). The difference $\delta\nu_c = 5.5 - 5.33 = 0.17$ occurs due to the relatively low Zeeman energy, which is not sufficient at the critical field of $5 \rightarrow 6$ PP transition to completely separate the two Landau levels with opposite spin directions. This is well-known behavior. The Zeeman energy E_Z is proportional to the magnetic field B, while the width of the Landau levels E_W is proportional to $B^{1/2}$ [81]. At high enough magnetic fields the Zeeman splitting is always dominant, but at moderate fields the width of the Landau levels becomes comparable to the Zeeman energy, which results in an overlap. Fig. 4.8 gives a sketch of the band structure at the critical filling factor $\nu = \nu_c$ when $E_Z \approx E_W$. The states in the grey area belong to the lower Landau level ($i = 5$), however, since they lie above the Fermi energy E_F, these states are empty. Therefore, the total filling factor ν in this situation is smaller by the amount $\delta\nu_c$ than expected for completely separated levels. Despite a non-zero density of states at the Fermi energy, the fifth Landau level does not contribute to resistivity, because the electrons in the tails of the Landau level are localized.

While the fit for the longitudinal resistance works reasonably well, the fit for the Hall data works perfectly. This is especially comfortable because only two parameters are used to fit the Hall resistance. As can be seen in Fig. 4.7c, the difference between experiment and fit is almost indistinguishable. The extracted parameters are: $\nu_0 = 0.029$ and $\nu_c = 5.34$. The value of ν_0 extracted from

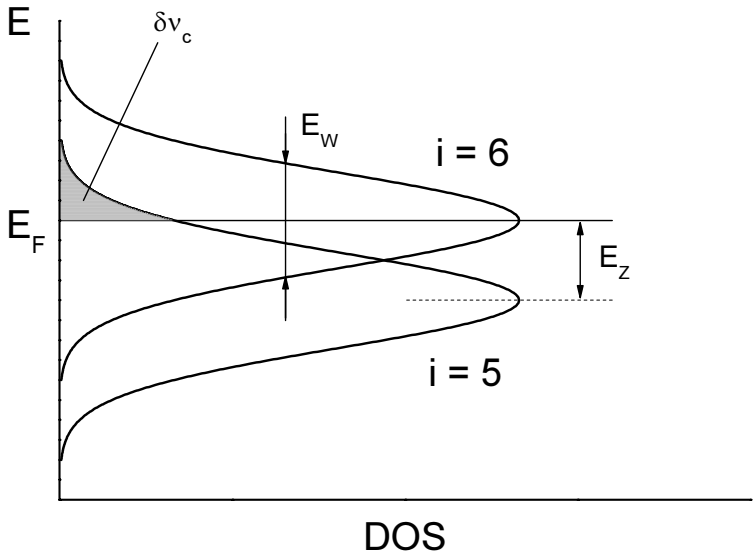

Figure 4.8: Schematic representation of the band structure of a 2DEG in a moderate magnetic field, when two Landau levels are overlapping. The Fermi energy E_F lies at the middle of the sixth Landau level, so $\nu = \nu_c$. Due to overlapping some of the localized states from the tail of the fifth Landau level are empty (grey area), resulting in $\nu_c < 5.5$.

the Hall measurements is somewhat larger than the one obtained from the longitudinal resistance. This is in agreement with results of simulations presented in Chapter 7. The more accurate value of ν_0 is the one extracted from the Hall data. The parameter ν_0 obtained from the longitudinal resistance is smaller and this decrease is caused by the density gradient. Since it would be more logical at a first glance to expect a widening of the transition and, therefore, a higher value of ν_0 for the ρ_{xx} data, we have to give a qualitative explanation for this unusual behavior. The density gradient affects the longitudinal resistance in two ways: it makes the transition wider in general, but it also changes the height of the peak. Depending on which pair of contacts, top or bottom, is used for the measurements, the peak value can be higher or lower than expected for the homogeneous sample. In the example shown in Fig. 4.7a, the peak is obviously higher ($R_0 = 1.14$). The deformation of the peak at the PP transition for small gradients is such that the central part of the peak is more affected than the shoulders. Therefore the "width at half-maximum" decreases due to an increase of the peak height. To determine the true widening of the PP transition due to inhomogeneities, the top and bottom longitudinal resistances have to be averaged. The peak obtained after averaging gives, according to simulations, a

larger value of ν_0 than the one obtained from Hall measurements.

In the last frame of Fig. 4.7 we present an example of a fit for the $2 \rightarrow 1$ PP transition of an InGaAs/AlGaAs QW. Although the shape of the experimental curve agrees well with the model, the measured data reveal an additional reproducible structure, enlarged for clarity in the inset. Although such a structure has been seen for other samples [79], it is still unclear whether the observed fluctuations affect the width of the transition. For mesoscopic samples such an influence is undoubtedly present, because the shape of the PP transition is completely modified [39].

4.4. When can reflection symmetry not be observed?

In the early days of the quantum Hall effect many experiments were done on samples of rather poor quality. Not only inhomogeneities in the 2DEG, but also fabrication of well defined Hall bars formed a problem. As a result, an additional complication occurs: misalignment of Hall contacts. Fortunately, this type of problem is easy to detect in Hall measurements by reversing the polarity of magnetic field. Moreover, it turns that misalignment does not affect the determination of the critical exponent. The reason for this is the following. The Hall resistance measured on such a sample is equal to $\rho_{xy} + \alpha\rho_{xx}$, where α is proportional to the misalignment of the Hall contacts. According to scaling ideas [10], both ρ_{xx} and ρ_{xy} are functions of the same scaling variable $X = (\nu - \nu_c)(T/T_0)^{-\kappa}$. Therefore, the linear combination $\rho_{xy} + \alpha\rho_{xx}$ is also a function of X. This argument is not valid, however, if the contact misalignment is accompanied by a density gradient, because then there is no simple dependence of the transport coefficients on a single variable.

According to the qualitative explanation of reflection symmetry given in Section 4.2, changing sign of the Hall resistance after field reversal (without changing its absolute value) is an important condition for observing reflection symmetry. Violation of Eq. (4.3) due to contact misalignment destroys the symmetry in $R_{xx}(B)$.

In Fig. 4.9 we present the results of measurements on an InGaAs/InP heterostructure. This sample with an averaged density $n = 2.2 \times 10^{11}$ cm^{-2} and transport mobility $\mu = 16000$ cm^2/(Vs) has been intensively used in the past for studying the PP and PI transition in the quantum Hall regime [82, 83]. However, at the time the papers were written, the effects of inhomogeneities on the transport data were not completely understood, and a wrong conclusion

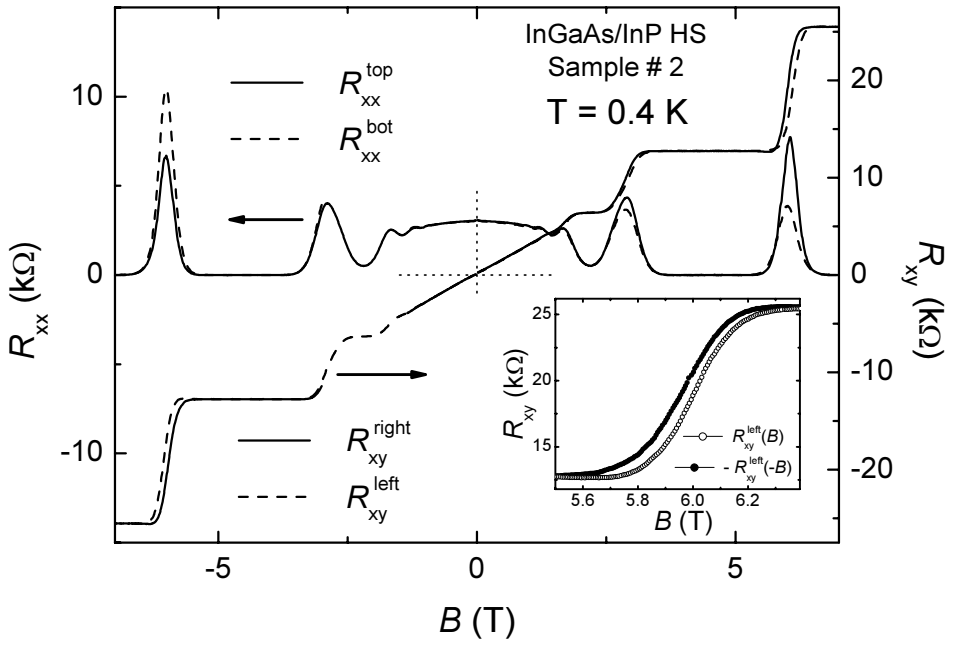

Figure 4.9: Longitudinal and Hall resistances of an InGaAs/InP heterostructure. The gradient of the electron density is accompanied by misalignment of Hall contacts. Reflection symmetry in the longitudinal resistance is absent.

was put forward. In particular, in Ref. [83] it was mentioned that the value of the critical exponent $\kappa = 0.55 \pm 0.05$, extracted from the PI transition, is different from the "true" universal value $\kappa = 0.42$ because of inhomogeneities.

Peaks in the longitudinal resistance in Fig. 4.9 at $|B| \approx 6$ T correspond to the $2 \rightarrow 1$ PP transition. The reflection symmetry in $R_{xx}(B)$ is clearly violated. The Hall resistances measured at different contact pairs exhibit a density gradient: the transition in $R_{xy}^{right}(B)$ takes place at a slightly lower field than in $R_{xy}^{left}(B)$ for both field polarities. However, the density difference cannot simply be calculated from the difference between R_{xy}^{right} and R_{xy}^{left} along the B-axis because these quantities depend on the field polarity. The inset shows the Hall data measured from the left pair of Hall contacts for positive and negative fields. In an ideal Hall bar these curves should coincide. One of the possible reasons for the observed difference is a misalignment of Hall contacts, which results in an additional contribution from the longitudinal resistivity. By subtracting $R_{xy}^{left}(B)$ from $|R_{xy}^{left}(-B)|$ we estimate the admixture of ρ_{xx} to R_{xy} to be of the order of 7-9%. Similar numbers were obtained for the right pair of Hall contacts. To calculate the "true" Hall resistance we average the Hall curves measured from the same contacts for both field polarities. From these we estimate a

density difference along the Hall bar of 1.6%.

At the end of this Section we would like to mention, that contact misalignment is not the only possible reason for violation of the reflection symmetry. In Chapter 7 we present results of numerical simulations, which show that the gradient of the electron density in an arbitrary direction, *i.e.* not parallel or perpendicular to the long edge of the Hall bar, can cause an "effective" contact misalignment. It means that even for a Hall bar with an ideally defined geometry Eq. (4.3) can be violated. One way of distinguishing real misalignment from the "effective" one, is to compare Hall and longitudinal resistances at zero field. If the misalignment is real, then at zero field the Hall signal should have a value proportional to the longitudinal resistance. If misalignment is "effective", the Hall signal should be zero at $B = 0$. In the experiment presented above, the zero field Hall resistance is ~ 0.2 kΩ. Taking into account the geometrical factor of the Hall bar we estimated a contribution of ~ 10 % of ρ_{xx} to the zero field Hall resistance, which means that the misalignment is real.

5

PLATEAU-INSULATOR TRANSITION IN AN INGAAS/INP HETEROSTRUCTURE

The plateau-insulator (PI) transition terminates the sequence of quantum Hall transitions in high magnetic fields. It takes place when the center of the lowest Landau level crosses the Fermi energy. The sample undergoes a transition into a true insulating phase with zero longitudinal conductivity and infinite resistance, in contrast with the plateau-plateau (PP) transitions at higher Landau levels, where both conductivity and resistivity are infinitely small (in the zero temperature limit) at both sides of the transition. Despite the dramatic differences between the experimental signatures of the plateau-plateau and plateau-insulator transitions, the underlying physics in both cases is very much the same. The PI and PP transitions can be described by the same universal formula and, therefore, demonstrate identical critical behavior.

It is not easy, however, to prove the universality of both types of transitions experimentally. As far as we know, there are no measurements which report the same critical exponent, extracted from magnetotransport data for both the PI and PP transitions. So far "universality" has been demonstrated in a limited temperature range via mapping one transition on the other (see, for example [84]), using the law of corresponding states [57]. At this stage it is important to notice that the problems are usually related to the PP transitions. The

PI transition most of the times agrees with theoretical predictions such as the universal and temperature independent value of $\sigma_{xx}^{max} = 0.5h/e^2$ at the critical field [20], the semicircle relation between components of the conductivity tensor [19] and a crossing point at the critical field B_c for curves $\rho_{xx}(B)$ measured at different temperatures.

In this chapter, we present the results of a systematic study of the PI transition in an InGaAs/InP heterostructure. We use the same sample as Wei and co-workers used in Ref. [14], *i.e.* the paper in which experimental evidence of scaling behavior of the quantum Hall PP transitions was demonstrated for the first time.

In Section 5.1 we present an overview of existing experimental results on quantum criticality and universality of PP and PI transitions in various quantum Hall systems. Next, in Section 5.2 we present new experimental data on the PI transition of the InGaAs/InP heterostructure. A detailed comparison of the data obtained for the PI and PP transitions in the same experiment and an extensive discussion is presented in Sections 5.3 and 5.4. Finally, the conclusions are given in Section 5.5.

5.1. Overview of early experimental results

The systematic experimental investigation of the critical behavior of quantum Hall systems started with the paper of H.P.Wei *et al.* [14], who measured the width of the peaks in the longitudinal magnetoresistance and the slope of the Hall resistance for several PP transitions in a low mobility InGaAs/InP heterostructure. The authors found that the inverse width of the peak $(\Delta B)^{-1}$, as well as the maximum slope $(dR_{xy}/dB)_{max}$, obey power-law temperature behavior with the same critical exponent κ:

$$\left(\frac{dR_{xy}}{dB}\right)_{max}, (\Delta B)^{-1} \sim T^{\kappa}, \tag{5.1}$$

The result was in agreement with scaling theory [10], which predicted an universal value of the critical exponent κ for all PP transitions (and the PI transition). Although the theory does not give any specific value for the critical exponent, the numerical value of $\kappa = 0.42 \pm 0.04$ is in perfect agreement with results of numerical simulations for non-interacting 2D electrons assuming the largest possible value of the dynamical critical index $p = 2$. Here p determines the temperature dependent phase coherence length $L_\varphi \sim T^{-p/2}$.

The pioneering work of H.P.Wei *et al.* stimulated an enormous activity in the field. Much research followed on various 2-dimensional systems in order to reproduce scaling behavior and to verify the universality of the critical exponent. Roughly, the resulting papers can be divided into three groups: papers that i) confirm scaling with a universal $\kappa = 0.42$ [83, 84, 85, 86, 87, 88, 89, 90, 91, 92]; ii) suggest scaling, but with an exponent that differs from $\kappa = 0.42$ [72, 73, 74, 75, 93]; iii) claim absence of scaling [94, 95].

Despite the large number of publications in the first group, more recent papers mostly belong to the second or third group. Moreover, there are examples, where authors re-evaluate their own experimental results, which were initially used as a demonstration of scaling with a universal exponent $\kappa = 0.42$. For instance, in Ref. [89] scaling is demonstrated for the PI transition of a low mobility InGaAs/InP sample. However, in a follow-up publication [94] the authors accept that the "collapse" of the experimental data in Ref. [89] on a single scaling curve takes place only in a limited temperature range. By analyzing a series of measurements on different samples a new phenomenological law $\nu_0(T) = \alpha T + \beta$, with sample dependent parameters α and β, was proposed [94] instead of the scaling dependence $\nu_0(T) = (T/T_0)^{0.42}$. Concerns about the validity of scaling in a limited temperature range were also expressed in Ref. [80]. Here the authors criticize their earlier publication on the scaling of PP transition in a modulation-doped p-SiGe structure [90]. In Ref. [80] the authors present measurements on the same sample, but over a wider T-range. The observed deviation from scaling behavior is attributed to an additional broadening of the Landau levels at high temperatures due to the Fermi-Dirac distribution.

The new value of the critical exponent $\kappa = 0.55 \pm 0.05$ extracted from the PI transition on InGaAs/InP heterostructures by van Schaijk *et al.* [83] was initially also believed to differ from the "established" value $\kappa = 0.42$ because of inhomogeneities. As a matter of fact, the data set presented in [83] was not complete. An additional experiment on the same sample, which included reversing of the polarity of the magnetic field and taking data at different sets of contacts, revealed [17, 52] that $\kappa = 0.57$ is the true exponent and that it is the PP, rather than the PI transition, which is affected by macroscopic inhomogeneities.

Although the publications in the first and second group claim to provide an experimental evidence for scaling, the data shown in these papers rather demonstrate the opposite sometimes: absence of critical behavior at low T. Often, below a certain sample dependent temperature, the transition width saturates as can be seen, for example, in Fig. 2 in Ref. [75] and in Fig. 4 in Ref. [74]

(with explicit statements about saturation in the text).

Summarizing this Section, despite a large number of experimental publications, there is no consensus in the quantum Hall community about universality of the PP and PI transitions. Even the existence of quantum critical behavior has been put to doubt.

At the same time, the value of the critical exponent $\kappa = 0.42$ is considered to be in good agreement with numerical simulations for the free electron gas, which hampers the acceptance of other non-Fermi liquid like values for κ.

5.2. Experiments on the PI transition and extracting critical exponents

In order to study the critical behavior of the transition to the insulating state and to verify universality of the PP and PI transitions we use the *same* sample HPW-#59, previously investigated by H.P.Wei and co-workers in Ref. [14]. Since the magnetic field needed for observing QHE transitions is inversely proportional to the critical filling factor ν_c at which the transition takes place, the measurements on the PI transition ($\nu_c \approx 0.5$) require about a 3 times higher magnetic field than for the $2 \rightarrow 1$ PP transition ($\nu_c \approx 1.5$). In the InGaAs/InP heterostructure studied by H.P.Wei *et al.* the $2 \rightarrow 1$ PP transition takes place at a magnetic field slightly below 10 T [14]. This implies that for measuring the PI transition, the magnetic field has to be of the order of 30 T.

A picture of the sample taken with a Carl Zeiss Microscope is shown in Fig. 5.1. Due to the relatively large size of the Hall bar the left current contact did not fit into the frame of the CCD camera attached to the microscope, which is the reason that it is not shown in the figure. Analogous to the sketch of the Hall bar in Fig.4.1a, the labels 3, 4, 5, and 6 in Fig. 5.1 indicate the potential contacts, while label 2 marks one of the current contacts. Other contacts (without labels) in Fig. 5.1 are not in use. One can easily see, that the edges of the Hall bar are not really straight. The width varies slightly along the Hall bar and it makes calculation of the geometrical factor inaccurate. We estimated the ratio of the width W over the distance L between the middle two potential contacts W/L at 0.37 ± 0.02. In addition, there is a considerable misalignment of the Hall contacts, which can easily be proven by measuring the Hall resistance at zero field or by reversing the polarity of the magnetic field in magnetotransport measurements.

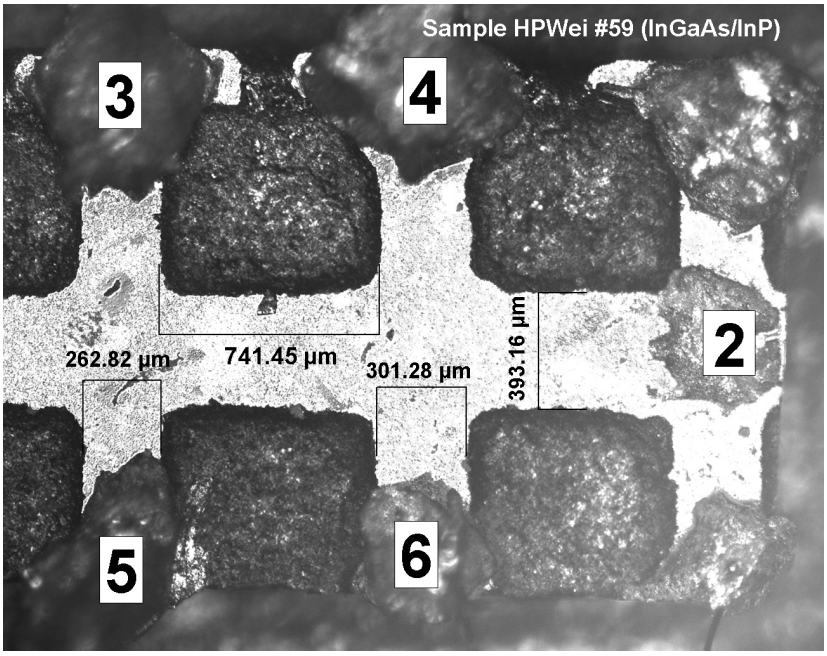

Figure 5.1: Sample HPW-#59 (InGaAs/InP heterostructure). Labels indicate the current and potential contacts used in the transport measurements. The left current contact is not shown.

Magnetotransport experiments were carried out in the Nijmegen High Field Magnet Laboratory using the 33 T Bitter magnet and the plastic dilution refrigerator (see Chapter 2).

A few typical magnetoresistance curves measured at different temperatures are shown in Fig. 5.2. As a reminder we mention that, every time when we present experimental data in this thesis using notations ρ_{xx} and ρ_{xy}, we refer to the normalized longitudinal resistance $\frac{W}{L}R_{xx}$ and the Hall resistance R_{xy}, which in most of the cases do not coincide with local values of the longitudinal and Hall resistivity due to inhomogeneities in the sample. For the curves shown in Fig. 5.2, we have used potential contacts 5-6 and 3-5 for measurements of the longitudinal and transverse resistances, respectively. The data are for positive polarity of the magnetic field. As in the paper of Wei *et al.* [14], the $2 \rightarrow 1$ PP transition takes place at fields slightly below 10 T. From the slope of the Hall resistance in weak magnetic field and from the zero-field longitudinal resistance we calculate the electron density $n \approx 3.4 \times 10^{11}$ cm^{-2} and transport mobility $\mu \approx 34000$ cm^2/(Vs). Both these parameters are in very good agreement with those reported in Ref. [14]. Therefore, we conclude that the overall transport parameters of the sample did not chance since it was studied by H.P.Wei *et al.*

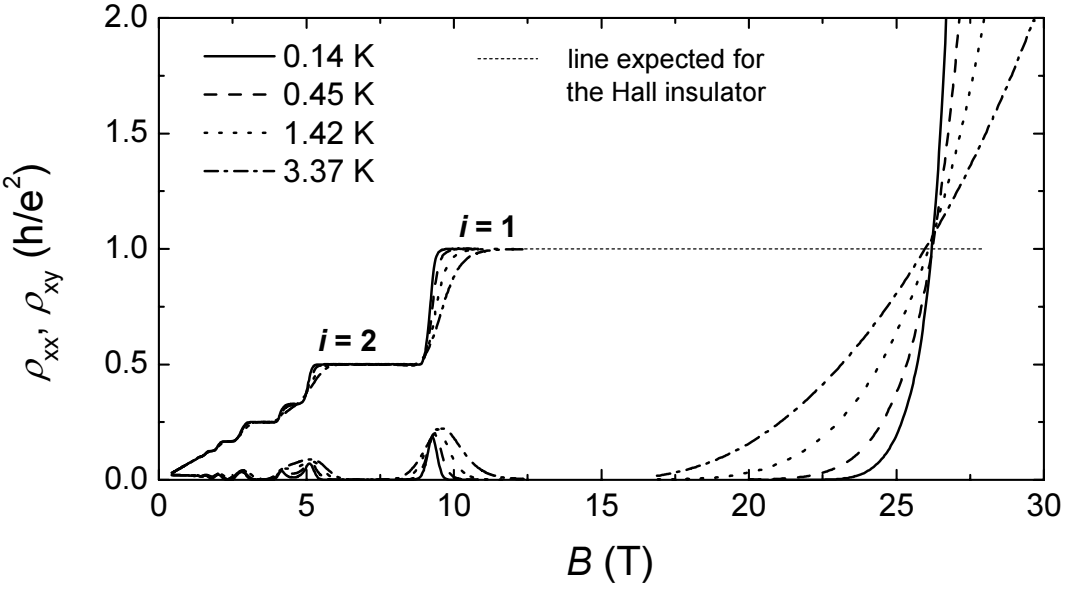

Figure 5.2: The longitudinal and Hall resistances measured on the InGaAs/InP heterostructure HPW-#59 at several temperatures as indicated. The longitudinal resistance is normalized by the geometrical factor W/L.

more than 15 years ago. This gives us the opportunity not just to compare the PI and PP transitions, but also to verify the results of the original paper.

In large magnetic fields, the curves $\rho_{xx}(B)$ measured at different temperatures show a crossing point at $B_c = 26.4$ T, *i.e.* the critical field of the plateau-insulator transition [17, 60, 83, 89]. The value of the normalized longitudinal resistance $\rho_{xx} = \frac{W}{L} R_{xx}$ at this field is temperature independent and amounts to $1.08 h/e^2$. The deviation from h/e^2 can be attributed to the uncertainty in the geometrical factor. The crossing point separates two phases. Above B_c there is a true insulating phase, where the longitudinal resistance increases with decreasing temperature. For $B < B_c$ the longitudinal resistance behaves metallic like, *i.e.* it decreases with decreasing temperature.

The Hall resistance is expected to be quantized through the PI transition at the value h/e^2 as shown by the thin dashed line in Fig. 5.2. Most of the reported experiments on the PI transition support this idea [17, 39, 60]. However, due to the strong field dependence of the longitudinal resistance and misalignment of Hall contacts, quantization cannot easily be proven experimentally. In Fig. 5.3a we show measurements of the Hall resistance at $T = 0.6$ K from the same pair of contacts for positive and negative polarity of the magnetic field as indicated. By averaging R_{xy} over both field polarities we may eliminate the

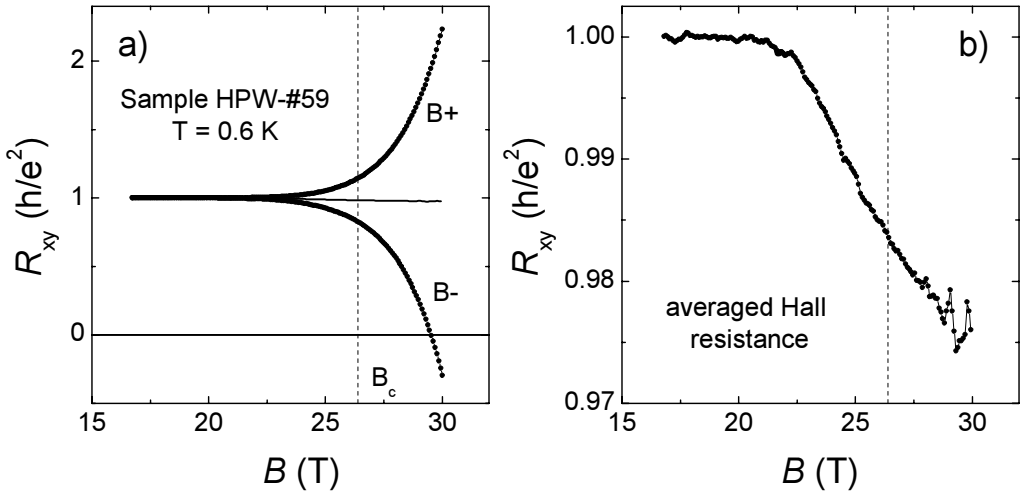

Figure 5.3: (a) Hall resistances of sample HPW-#59 near the PI transition for positive and negative polarity of the magnetic field as indicated. The solid line represents the averaged value. The vertical dashed line indicates the critical field B_c for the PI transition; (b) Zoom in on the averaged Hall resistance. The deviation from the quantized value h/e^2 of the order of 2% near B_c is clearly visible.

field-symmetric contribution from the longitudinal resistance. The solid line in Fig. 5.3a results after averaging. Plotted on the same scale as the experimental data, the averaged curve appears to be quantized. However, a closer inspection of the averaged data shows a deviation of the order of 2 % from h/e^2, as shown in Fig. 5.3b. At present we do not have a satisfactory explanation for the observed downward curvature of R_{xy}. Since the out-of-phase signal does not exceed 3% we are sure it cannot be attributed to an erroneous signal due to high sample resistance and capacitive losses between wires (Chapter 2). A possible explanation is that it is due to the relatively short distance between current and potential contacts on the Hall bar. Our numerical simulations, presented in Section 7.9, indeed show that the proximity of current and potential contacts can lead to deviations of the Hall resistance towards smaller values. Another possible explanation is that the deviation from quantization is just a systematic error of the measurements. Basically, we are trying to obtain constant value of R_{xy} by averaging two quite different and rapidly changing quantities. Despite of the high signal to noise ratio, the lock-in technique does not yield a very high absolute accuracy. The experimental data published so far by other groups all seem to have the same problem: the averaged Hall resistance usually deviates from the value h/e^2 [39, 60].

From a theoretical point of view there are three possible scenario for the behavior $R_{xy}(B)$ in the insulating state [57, 96, 97]. The Hall resistance R_{xy} can be: a) quantized *i.e.* field and temperature independent; b) diverging to infinity together with the longitudinal resistance; c) following classical behavior $R_{xy} \sim B$. Clearly our data are in support of the quantized Hall insulator.

If the Hall resistance stays quantized at $R_{xy} = h/e^2$, the components of the conductivity tensor automatically follow the semicircle law at the PI transition. The equations:

$$\sigma_{xx} = \frac{\rho_{xx}}{\rho_{xx}^2 + 1}, \quad \sigma_{xy} = \frac{1}{\rho_{xx}^2 + 1} \tag{5.2}$$

obtained from Eq. (1.8) by substituting $\rho_{xy} = 1$ (in units h/e^2) are the parametric equations for a semicircle in the $\sigma_{xx}(\sigma_{xy})$ plane. Details of the field dependence $\rho_{xx}(B)$ are not important, as long as it changes from zero to infinity. Sample inhomogeneities also do not play a role. The only essential requirement is quantization of the Hall resistance, $\rho_{xy} = 1$.

The theory, however, implies more than just a semicircle. It also defines the exact position of the critical point at $\sigma_{xx} = \sigma_{xy} = 1/2$ (in units e^2/h)[20], which results in a T-independent crossing point at the critical field B_c where $\rho_{xx} = \rho_c = h/e^2$. Within the uncertainty in the geometrical factor, the experimental curves in Fig. 5.2 fulfil this condition. A crossing point at $\rho_c = h/e^2$ was also reported in Refs. [17] and [73]. However, in literature different values of ρ_c, which most likely originate from inhomogeneities in the sample, have been reported as well: $1.65h/e^2$ [60], $0.86h/e^2$ [89], 0.93 and $1.15h/e^2$ [94].

In Fig. 5.4 we present, in more detail, the experimental data for ρ_{xx} of sample HPW-#59 at the PI transition. The longitudinal resistance is shown as a function of the filling factor ν in order to verify validity of the phenomenological dependence proposed by Shahar *et al.* [94]:

$$\rho_{xx}(\nu, T) = \frac{h}{e^2} \exp(-\frac{\nu - \nu_c}{\nu_0(T)}) \tag{5.3}$$

where ν_c is the critical filling factor associated with the position of the crossing point. On the upper axis the corresponding values of the magnetic field values are given. The filling factor has been calculated from the magnetic field using Eq. (1.6) with the electron density $n \approx 3.4 \times 10^{11}$ cm^{-2} obtained from the slope of the Hall resistance in low fields at 4.2 K. The PI transition takes place at a filling factor $\nu_c \approx 0.53$, which is slightly larger than the value $\nu_c = 0.5$ expected for a half-filled Landau level. So far, in all experimental papers reporting on the

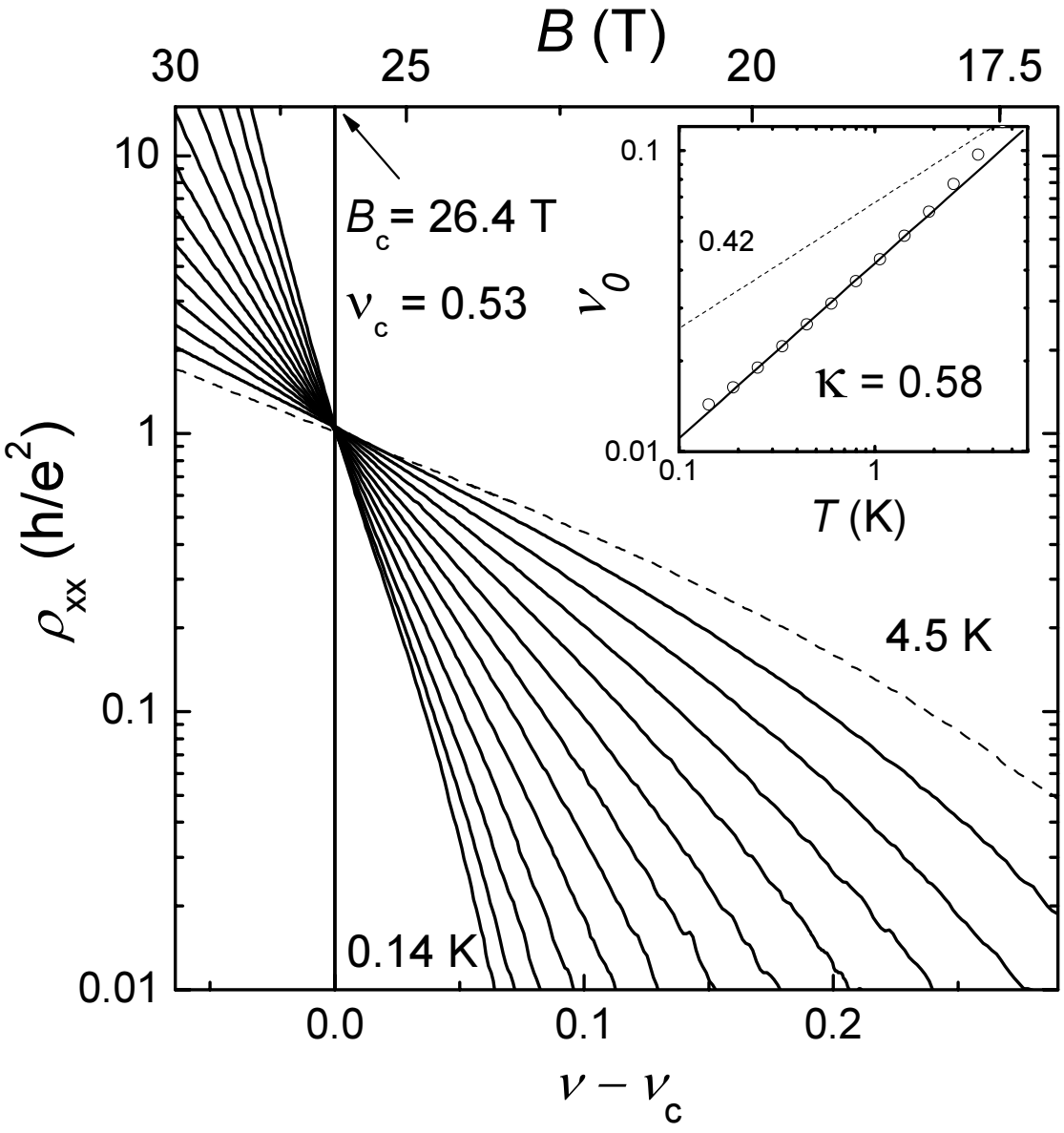

Figure 5.4: The longitudinal resistance of an InGaAs/InP heterostructure (sample HPW-#59), normalized by the geometrical factor, plotted versus the filling factor (lower axis) and magnetic field (upper axis) at several temperatures: 4.5 (dashed line), 3.4, 2.5, 1.9, 1.4, 1.1, 0.8, 0.6, 0.45, 0.34, 0.25, 0.19 and 0.14 K. The inset shows the temperature dependence of the parameter ν_0, which is proportional to the slope of the curves in the main figure at the critical point. From the linear fit of $\nu_0(T)$ in the double logarithmic plot, the critical exponent $\kappa = 0.58 \pm 0.02$ has been extracted. For comparison we also show the line corresponding to $\kappa = 0.42$

PI transition, the value of ν_c is somewhat higher than 0.5. It ranges between 0.69 [73] and 0.53 [98], and higher values of ν_c are usually observed on samples with lower density.

As follows from Fig. 5.4, close to the critical point the experimental data can be described by Eq. (5.3). Indeed, all curves, except the one at the highest temperature (4.5 K), cross at the same point and obey a linear behavior near ν_c. Away from the crossing point deviations, however, become significant, which means that higher order terms of $(\nu - \nu_c)/\nu_0(T)$ contribute to the exponential function in Eq. (5.3). Higher order corrections, as we mentioned in Section 4.3, are most likely the reason for deviation of the experimental data from the fit curve (3.13) in Fig. 4.7b. This expression for a fit function was obtained by the Landau level addition transformation, assuming that the longitudinal resistance at the PI transition obeys the exponential dependence given by Eq. (5.3).

In order to analyze the critical behavior we extract from the experimental data in Fig. 5.4 the temperature dependent parameter $\nu_0(T)$, which is inversely proportional to the slope of $\log(\rho_{xx})$ *vs* ν at the critical point. In the inset we show the temperature dependence $\nu_0(T)$ obtained by fitting of the linear behavior in the vicinity of ν_c, shown in the main figure. The critical, *i.e.* power law, behavior implies that the data points $\nu_0(T)$ fall on a straight line in a double logarithmic plot, where the critical exponent is equal to the slope of the line. Strictly speaking, the open points in the inset do not fall on a straight line. Deviations occur at the lowest and highest temperatures. However, fitting the data below 2 K only, which still covers one order of magnitude in T, we extract the critical exponent $\kappa = 0.58 \pm 0.02$. This is the most important result of the present experiments. The numerical value of κ is significantly higher than the previously established value 0.42 ± 0.04, measured on *the same sample* for the PP transitions [14]. For comparison we also show in the inset the dashed line with slope corresponding to $\kappa = 0.42$.

At high temperatures, the deviations of $\nu_0(T)$ from the critical behavior at the PI transition can be attributed to the Fermi-Dirac distribution in the density of states [80]. In fact, departures from scaling can be seen already in the raw data. The curve $\rho_{xx}(B)$ at 4.5 K shown by the dashed line in Fig. 5.4 does not encompass the common crossing point. It means that at this temperature the longitudinal resistance is not a function of the single variable $X = (\nu - \nu_c)(T/T_0)^{-\kappa}$ any more and the 2DEG is not in the scaling regime.

At the end of this Section we would like to discuss the symmetry of the magnetoresistance data. In chapter 4 we showed that a gradient in the electron

density leads to a reflection symmetry in the longitudinal resistance at the PP transition. One can ask the question whether this is true for the PI transition as well. Perhaps it comes as a surprise, but the longitudinal resistance for the PI transition does not depend on the field polarity and the particular choice of contacts. The reason for this is the quantization of the Hall resistance. The reflection symmetry between R_{xx}^{top} and R_{xx}^{bot} for the PP transitions, originates from the inequality of R_{xy}^{left} and R_{xy}^{right}, which in turn, is caused by the difference in local values of the critical field in different parts of the sample. At the PI transition the Hall resistance is quantized. Therefore:

$$R_{xy}^{left} = R_{xy}^{right} \tag{5.4}$$

and

$$R_{xx}^{top} = R_{xx}^{bot}. \tag{5.5}$$

for both field polarities. Contact misalignment, of course, may violate these last two relations and leads to additional terms proportional to ρ_{xx}. Instead of Eq. (5.5) we obtain:

$$R_{xx}^{top} = (1+\varepsilon)R_{xx}^{bot}. \tag{5.6}$$

where $\varepsilon << 1$ is a field and temperature independent constant proportional to the contact mismatch.

The extra contribution from the parameter ε, however, does not change the slope of the longitudinal resistance in the logarithmic plot and does not affect the crossing point. It only results in a vertical shift. Therefore, in case of the PI transition a small contact misalignment does not impose serious problems for analyzing the longitudinal resistance. However, as we already discussed, it renders studies of the Hall resistance fairly difficult.

5.3. Comparison of the PI and PP transitions

In the "traditional" method of analyzing magnetotransport data proposed by H.P.Wei *et al.*[14] the only quantity that has been compared for different PP transitions is the value of the critical exponent κ. Universality implies that the numerical value of κ does not depend on the Landau level index. Moreover, both the longitudinal and Hall resistance measurements should provide the same value of κ. In order to prove scaling, the transport data have to

be studied over a broad temperature range, which covers at least one order of magnitude. A drawback of this method is that it does not allow to establish a direct correspondence between different transitions at a fixed temperature.

Experimental attempts to treat universality wider and to map one transition on the other at a fixed temperature using Landau level addition transformations [57] were made by Shahar *et al.* [84] and by Coleridge [90]. In both cases the authors reported on the remarkable similarities between the measured curves and those obtained by mapping. The term universality used by the authors of Refs. [84, 90] has, however, a somewhat different meaning than the universality reported by Wei *et al.* [14]. For instance, the presence of scaling and universality of κ do not necessarily require Landau level addition to be valid. Also, even if the Landau level addition transformation gives rise to proper mapping, the PP and PI transitions do not necessarily scale, *i.e.* show critical behavior with a fixed critical exponent.

The expressions for the components of the resistivity tensor proposed by Oswald, Span and Kuchar [61] as given in Eqs.(3.13)-(3.15), allow one to merge both methods into one. The parameter ν_0 is proportional at the same time to: a) the width of the PP transitions in $\rho_{xx}(\nu)$ data, b) the maximum slope of the $\rho_{xy}(\nu)$ curve, and c) the slope of $\ln(\rho_{xx})$ vs ν at the PI transition. If the Landau level addition transformation works, the values of ν_0 at any fixed T should be the same for all transitions, and in case of universal scaling all the temperature dependencies $\nu_0(T)$ should obey power law behavior with the same critical index κ:

$$\nu_0(T) = (T/T_0)^{\kappa} \tag{5.7}$$

Note, if the parameter T_0 depends on the Landau level index, it automatically implies that the Landau level addition transformation is not valid.

As mentioned before our new data were taken on the same sample as used by Wei *et al.* [14]. We note however an important difference between the analysis of Ref. [14] and the one presented in this chapter. The point is, that the components of the resistivity tensor can be presented as function of the magnetic field B or, equivalently, as function of the filling factor ν. Therefore, the width of the peak in ρ_{xx} can also be obtained in terms of the magnetic field (ΔB) or the filling factor ($\Delta\nu$). The filling factor is inversely proportional to the magnetic field, which means that the temperature dependencies of ΔB and $\Delta\nu$ are quite different. If one of these dependencies is represented by a power law, it does not mean that the other one follows a power law behavior as well. Both

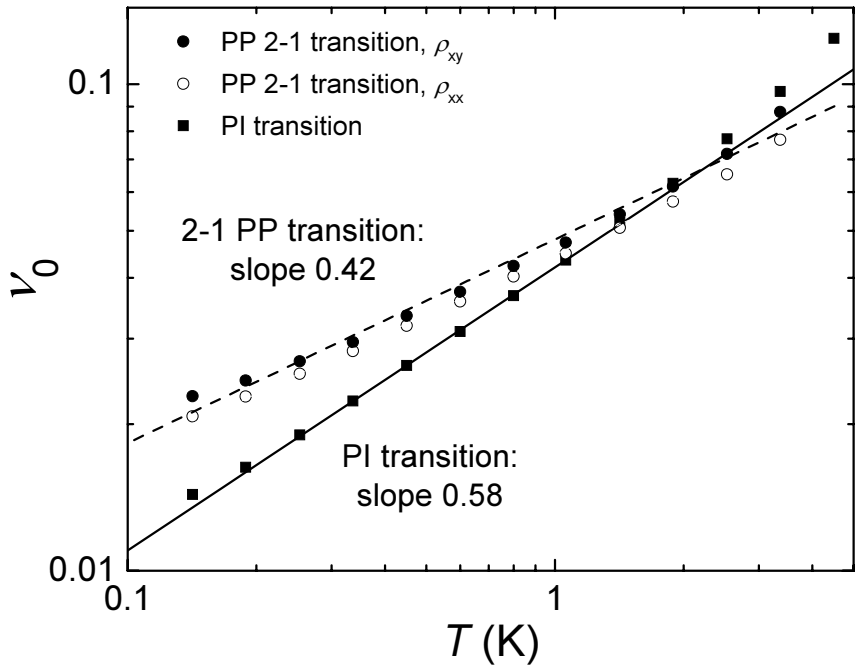

Figure 5.5: The temperature dependencies of the parameter ν_0 extracted from the PI and $2 \rightarrow 1$ PP transitions. The PI transition data demonstrate critical behavior with the critical exponent $\kappa = 0.58$. The strong deviation of $\nu_0(T)$ for the PP transition from the power law dependence is due to widening of the transition, presumably caused by macroscopic sample inhomogeneities (see Chapter 7). The linear fit, which is not really appropriate in this case, gives for the PP transition data $\kappa = 0.42$, the same value as reported in Ref. [14].

ΔB and $\Delta\nu$ have the same temperature behavior only if ΔB ($\Delta\nu$) is much smaller than the magnetic field B_c (critical filling factor ν_c), at which the transition takes place. This is, however, not always the case, especially at high temperatures. From the theoretical point of view, scaling implies that the components of the resistivity tensor are functions of the single variable $X = (\nu - \nu_c)(T/T_0)^{-\kappa}$. Therefore, the width of the peak in the longitudinal resistance has to be calculated in terms of the filling factor. In Ref. [14], however, the width was determined in terms of the magnetic field.

Next, we show in Fig. 5.5 the temperature dependence $\nu_0(T)$ obtained for the PI and the $2 \rightarrow 1$ PP transitions. Notice, the data points for the PI transition are the same as in the insert of Fig. 5.4. The PP transition data were extracted from the longitudinal and Hall resistances measured at potential contacts 3-4 and 4-6, respectively, and then averaged over both polarities of the magnetic field. The parameter ν_0 was obtained by fitting the magnetotransport curves

according to the procedure described in Section 4.3.

The open and solid circles in Fig. 5.5 represent $\nu_0(T)$ extracted from the longitudinal and Hall resistances at the $2 \rightarrow 1$ PP transition, respectively. Both data sets have a similar temperature dependence. The difference at any fixed temperature does not exceed 10 %. However, the difference between $\nu_0(T)$ for the PI and PP transition is dramatic. First of all, the curves for the PP transition strongly deviate from a straight line. Thus no scaling is observed for the PP transition. This is a first and most important difference compared to the results reported in Ref. [14]. The character of the deviation is such that there is a clear tendency towards saturation. The dashed line in Fig. 5.5 represents the linear fit of $\nu_0(T)$ obtained from the longitudinal resistance at the PP transition (solid circles). Although such a fit is not appropriate in this situation, it is important to notice, that the value of the "critical exponent" obtained in this way is 0.42. As regards the absolute value of ν_0, the best agreement between the two data sets is found around $T \sim 2$ K. With decreasing temperature, the difference between ν_0 extracted from the PI and PP transitions becomes larger, exceeding 40 % for the data extracted at the lowest temperature. This implies, that in this case Landau level addition definitely cannot be applied for transforming the PI data into PP data and vice versa. Our accuracy in the determination of ν_0 is better than 2%. Therefore 40% difference at $T = 0.14$ K indicates a true widening of the peak in $\rho_{xx}(\nu)$ at the $2 \rightarrow 1$ PP transition compared to the width expected from the PI data.

Another point of concern is the height of the peak in ρ_{xx} at the PP transitions. The Landau level addition transformation implies that the maximum value of $\rho_{xx}(\nu)$ at the $2 \rightarrow 1$ PP transition is temperature independent and equal to $h/(4e^2)$. The measured temperature dependence of the peak height is shown in Fig. 5.6. Data represent measurements for the top (3-4) and bottom (5-6) pairs of contacts for positive and negative field polarities. All dependencies are surprisingly similar. This means, that density gradients are small, otherwise, according to the findings of the previous chapter, we should observe large differences in the peak height. Small differences between the data sets and violation of the reflection symmetry are due to contact misalignment. In contrast to the expected T-independent behavior with $\rho_{xx}^{max} = 0.25h/e^2$, the measured peak heights are smaller and have a pronounced non-monotonic temperature dependence with a maximum around 2 K. At this temperature, the difference between the theoretically expected ($0.25\ h/e^2$) and real ($\sim 0.21h/e^2$) value of ρ_{xx}^{max} is the smallest. Since the values of the parameter ν_0 near 2 K are almost the same for

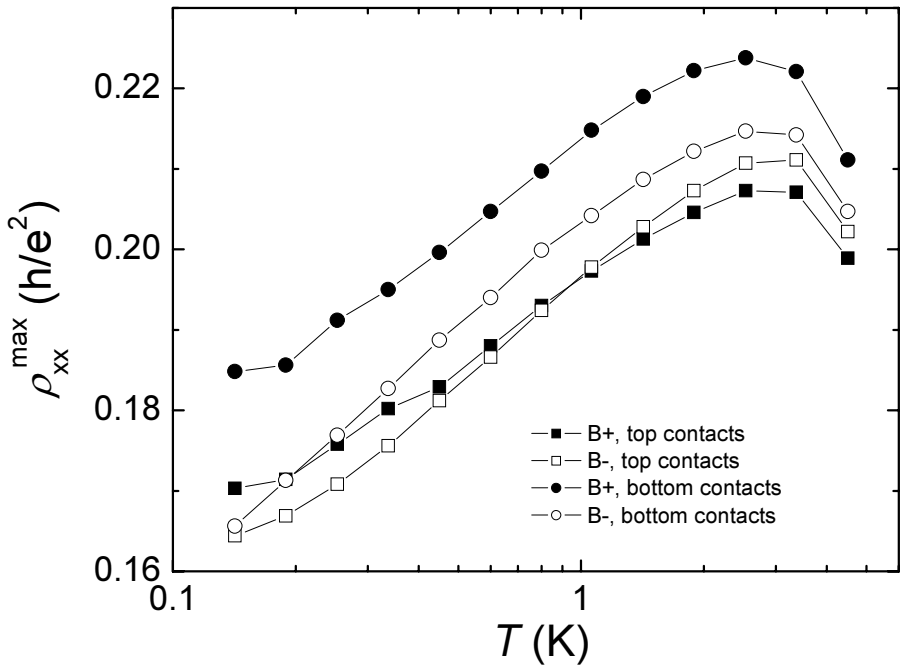

Figure 5.6: The temperature dependencies of the maximum of the longitudinal resistance at $2 \rightarrow 1$ PP transition normalized by the geometrical factor ($\rho_{xx}^{max} = \frac{W}{L} R_{xx}^{max}$). Data are shown for the top and bottom pairs of contacts and for positive and negative magnetic field direction. According to the Landau level addition transformation ρ_{xx}^{max} should be temperature independent and equal to $h/(4e^2)$.

the PP and PI transition, we can say that at this temperature the Landau level addition transformation is "almost valid". This cannot be considered, of course, as an experimental evidence of its validity, because the law of corresponding states was derived in the limit $T \rightarrow 0$. Therefore, we have to accept that the Landau level addition transformation simply does not work or that there are other reasons, which hamper experimental verification of its validity. From our point of view, macroscopic sample inhomogeneities are responsible for the observed discrepancy. Inhomogeneities strongly affect the PP and almost have no effect on the PI transition due to the very different character of the dependence of the resistance on the filling factor for these two transitions. Qualitatively (and very roughly), the difference can be explained in the following way. The longitudinal resistance is measured over a rather large distance L, where the local carrier density varies due to macroscopic inhomogeneities. Therefore, the measured resistance represents some sort of averaged value. At the PP transition the longitudinal resistivity has a peak-like dependence on the magnetic field. Small variation of the carrier density shifts the peak position along the

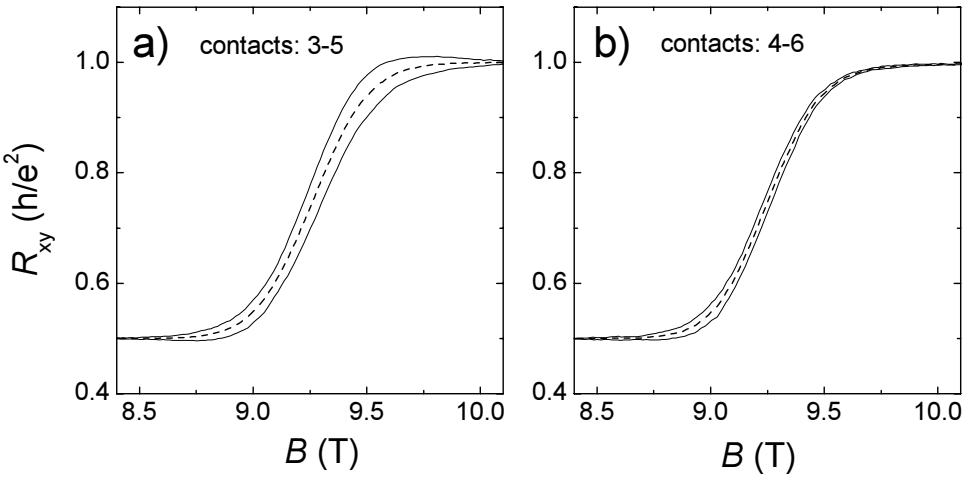

Figure 5.7: The Hall resistances of sample HPW-#59 as a function of magnetic field measured at contacts 3-5 (a) and 4-6 (b). Solid lines are the experimental data measured at positive and negative polarities of the magnetic field. The averaged curves are shown by the dashed line. Data were taken at $T = 0.45$ K.

B-axis. Averaging of peak functions with closely located maxima (closer than the width of the peak) gives us another peak function with lower height and larger width. In contrast, the longitudinal resistance at the PI transition is an exponential function of B. Averaging of exponential functions with the same exponent, but slightly shifted along the B-axis, results in a very similar function in the analysis of the experimental data, with most importantly almost the same exponent. That is why for the same amount of macroscopic inhomogeneities the PI transition still gives the correct value of ν_0, while for the PP transition the extracted value of ν_0 is overestimated and accompanied by a decrease of the peak height. In Chapter 7 we provide further evidence for these results based on numerical simulations of the transport problem.

Next we estimate the amount of inhomogeneities in the sample. The most straightforward method was described in the previous chapter and gives the density difference between two pair of Hall contacts. Since the sample has a significant contact misalignment, the true Hall resistance should be determined by averaging two Hall resistances measured for opposite field polarities. The experimental data measured at $T = 0.45$ K and the averaged curves are shown in Fig. 5.7 for two pairs of potential contacts. Despite the obvious difference between the experimental curves, the averaged data, when plotted on the same graph, practically coincide. This means that the local values of the electron density near the potential contacts are almost the same and that the density gradient

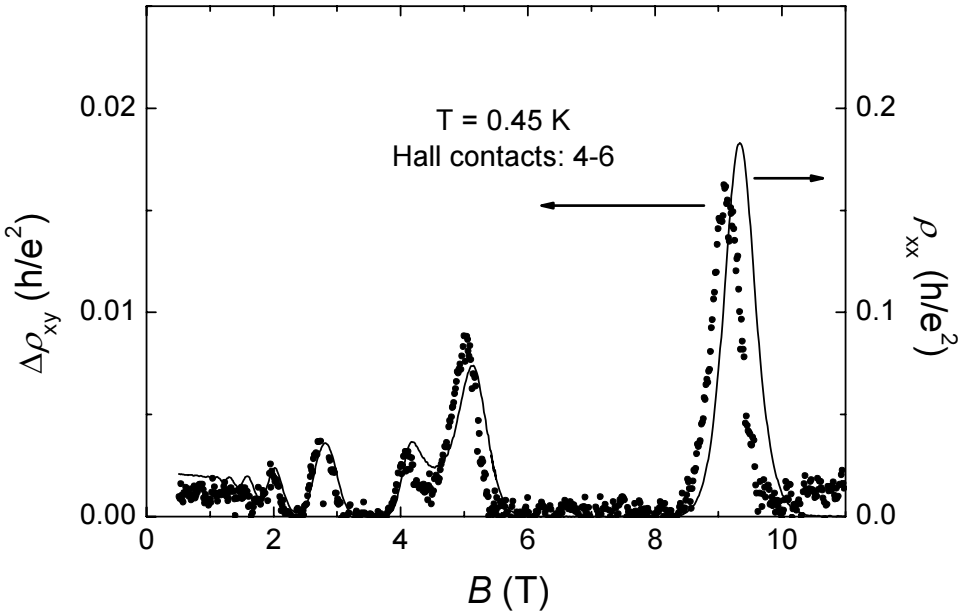

Figure 5.8: The difference $\Delta\rho_{xy}$ between the absolute values of the Hall resistances measured at contacts 4-6 at positive and negative magnetic field (solid symbols, left axis) and the longitudinal resistance normalized on the geometrical factor $\rho_{xx} = \frac{W}{L}R_{xx}$ (solid line, right axis) plotted as function of the magnetic field at $T = 0.45$ K. The shift between the positions of the maxima indicates a difference of ~ 1.5 % between the local (near potential contact 4-6) and the averaged electron densities.

is very small. This is not a surprising result. The same conclusion was already drawn from the comparison of the peak heights ρ_{xx}^{max} presented in Fig. 5.6. Comparison of the averaged Hall resistances indicate that the difference between the local densities does not exceed 0.1%.

An almost vanishing difference between the averaged Hall resistances does not indicate, however, that the sample is homogeneous. Surprisingly, the contact misalignment, which is generally an unwanted property of the Hall bar, helps us to estimate the variation of the carrier density in sample HPW-#59 beyond the gradient approximation. Due to the misalignment of the contacts the measured Hall resistance consists of two contributions with different parity upon reversal of the magnetic field. One is the true Hall resistance, which is an odd function of the magnetic field, and the other one is an additional term proportional to the longitudinal resistivity and the contact mismatch. The second term is always positive irrespective of the polarity of the magnetic field. Therefore, the difference between the absolute values of the Hall resistances

measured for positive and negative magnetic field is proportional to the longitudinal resistance, or to be more precise, to the local value of the longitudinal resistivity in the region between two Hall contacts. In Fig. 5.8 we compare the difference $\Delta\rho_{xy} = |\rho_{xy}^{right}(+B)| - |\rho_{xy}^{right}(-B)|$ with the longitudinal resistance, which was measured at the top pair of contacts (3-4) for positive polarity of the magnetic field. Although the relative error in the $\Delta\rho_{xy}$ data is rather large, the position of the peak at the $2 \rightarrow 1$ PP transition is clearly shifted towards lower fields compared to the data for the longitudinal resistance. This can only be due to a difference in the electron density. The difference $\Delta\rho_{xy}$ is measured locally between two Hall contacts, while ρ_{xx} represents the averaged value between contacts 5-6 over a sample length L. From the shift between the peak maxima we estimate a density difference of $1.5 \pm 0.3\%$. Since this is the difference between the averaged and local values, the peak-to-peak fluctuation of the local density in the sample should be, at least, twice larger or of the order of 3%. As we will show in Chapter 7 this value is large enough to change the first significant digit of the critical exponent κ. Therefore, the difference between $\kappa = 0.58$ extracted from the PI transition and $\kappa = 0.42$ obtained from the PP data is not surprising.

Even more accurate measurements of the difference between the local and averaged values of the carrier density can be made using the PI transition. Again, we use contact misalignment to extract the "local" longitudinal resistance from the difference between the Hall resistances measured for opposite polarities of the magnetic field. In Fig. 5.9, the difference $\Delta\rho_{xy}$ at several temperatures is compared with the measured longitudinal resistance. The common feature of plots (a) and (b) is the presence of the crossing point at the critical field. However, the value of B_c is different in the different panels. Assuming that in both cases the PI transition takes place at the same critical filling factor, the shift of the crossing point can be explained by a difference in the electron density. The accuracy of this method is higher compared to the method explained in the previous paragraph, because of the significantly larger value of the longitudinal resistance at the PI transition. The density difference is estimated at $1.6 \pm 0.1\%$, which is consistent with the result obtained from the PP transition data at fixed temperature.

Summarizing, in this Section we have made a quantitative analysis of the macroscopic inhomogeneities of the sample HPW-#59. A lower bound for the variation of the electron density across the sample is $\sim 3\%$. We also observed a pronounced temperature dependence of ρ_{xx}^{max} at the $2 \rightarrow 1$ PP transition and a

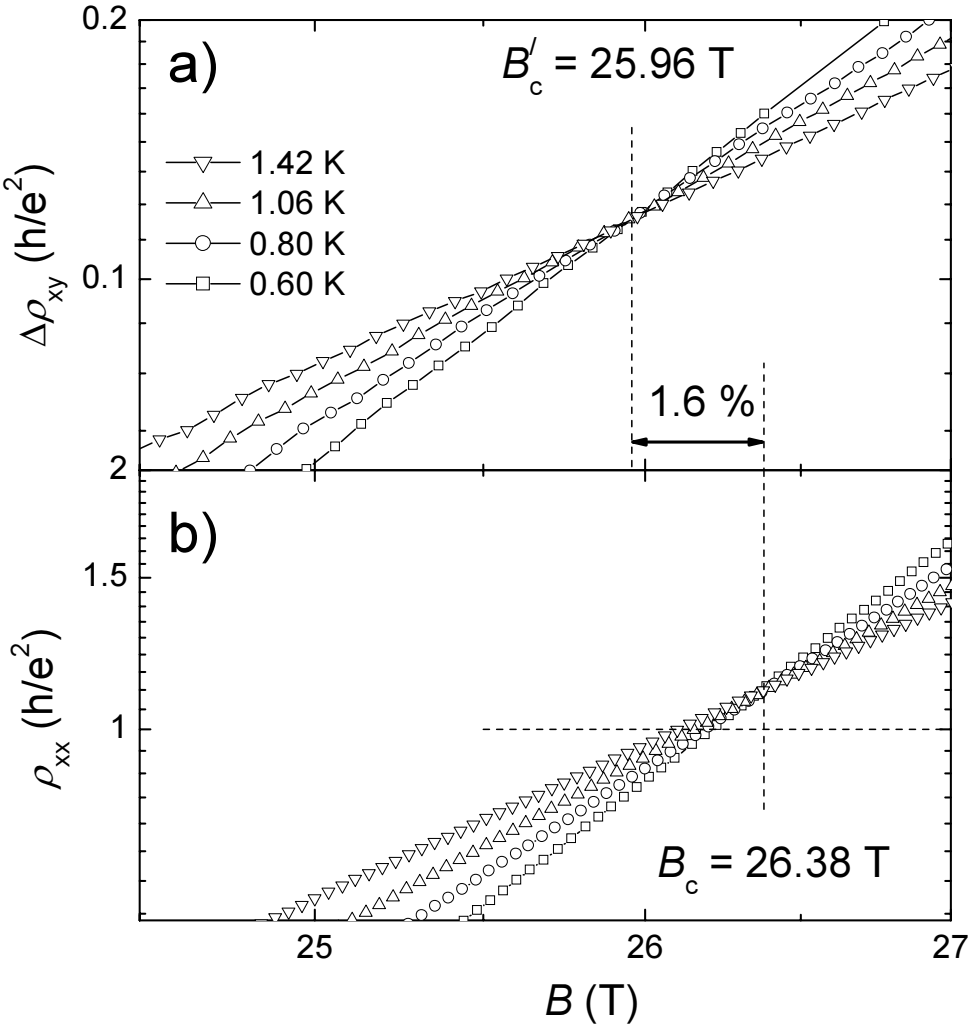

Figure 5.9: (a) The difference $\Delta\rho_{xy}$ between the absolute values of Hall resistances measured on contacts 1-4 at positive and negative magnetic field at several temperatures as a function of B; (b) The longitudinal resistance normalized by the geometrical factor at the same temperatures as in (a). The data sets in both panels show a crossing point corresponding to the critical field of the PI transition. The difference between the position of the crossing points is due to the difference between the local and averaged carrier densities.

deviation of the temperature dependence of the parameter ν_0 (proportional to the width of the PP transition) from scaling behavior. The Landau level addition transformation was found not to be valid for a transformation of the PI to $2 \rightarrow 1$ PP transition. All observed features can be qualitatively accounted for by a 3% carrier density variation as will be shown by numerical simulations in Chapter 7.

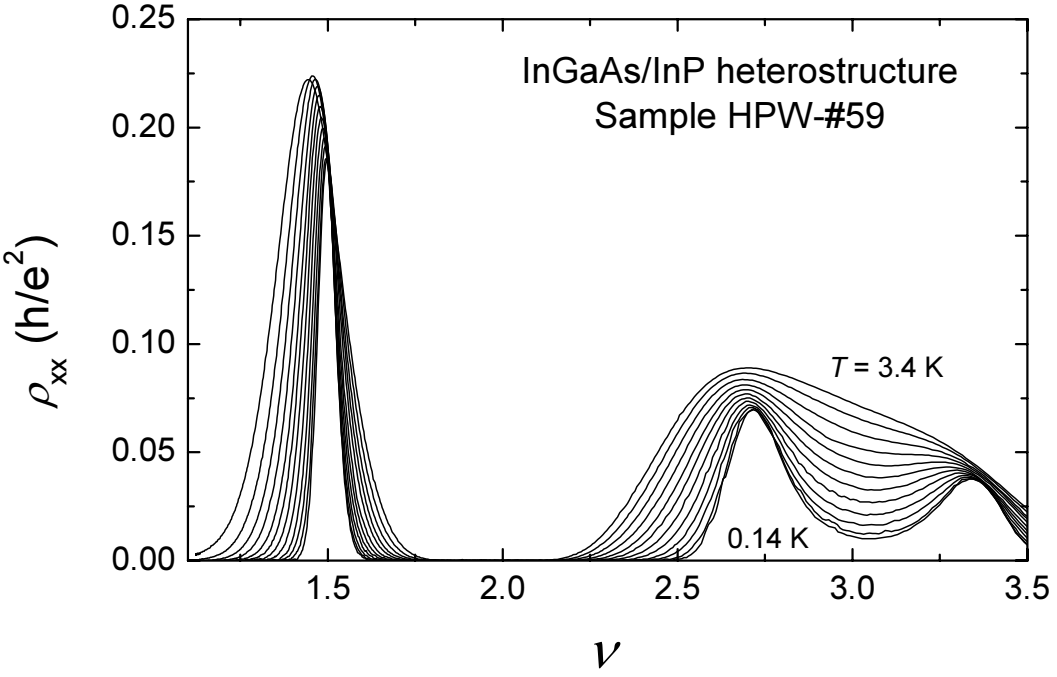

Figure 5.10: The longitudinal resistance normalized by the geometrical factor $\rho_{xx} = \frac{W}{L} R_{xx}$ as a function of the filling factor at temperatures: 3.4, 2.5, 1.8, 1.4, 1.1, 0.8, 0.6, 0.45, 0.34, 0.25, 0.19 and 0.14 K. The field polarity is negative; data are taken from potential contacts 5 and 6.

5.4. Higher order PP transitions in an InGaAs/InP heterostructure

One of the most important results of Wei's paper [14] is the demonstration of universality of the critical exponent measured for different PP transitions, notably the $2 \rightarrow 1$, $3 \rightarrow 2$ and $4 \rightarrow 3$ PP transitions were investigated and all could be described by $\kappa = 0.42 \pm 0.04$.

We have shown already, that the experimentally obtained value $\kappa = 0.42$ for the $2 \rightarrow 1$ PP transition is the result of inherent sample inhomogeneities, which strongly hamper observation of true critical behavior. Consequently, the question arises whether inhomogeneities affect all the PP transitions in the same way.

To answer this important question we present in Fig. 5.10 the raw experimental data of the longitudinal resistance as a function of the filling factor in the temperature range 0.14-3.4 K. Notice that for sake of clearness we did not label all the curves, but wider peaks corresponds to higher temperatures. The

first feature to pay attention to is the position of the peaks. As expected from theory, the $2 \rightarrow 1$ PP transition (the highest peak in the plot) takes place at a semi-integer filling factor ($\nu \approx 1.5$). This is not the case, however, for other PP transitions shown in Fig. 5.10. The maximum of the peak for the $3 \rightarrow 2$ PP transition takes place at a filling factor significantly higher than 2.5, while the next $4 \rightarrow 3$ PP transition appears at ν lower than 3.5. Although it is not correct to identify the position of the maximum in $\rho_{xx}(\nu)$ with the critical filling factor[1], in practice the difference between them is small. The minimum in $\rho_{xx}(\nu)$ between these two transition occurs at $\nu \approx 3$, where it is expected to be. A shift in the positions of peak maxima, while the minimum stays at the proper filling factor, indicates, that the $3 \rightarrow 2$ and $4 \rightarrow 3$ PP transitions are not completely resolved, which can happen if the gap between the centers of the Landau levels is smaller than the level width. A similar situation was considered in the previous chapter for a GaAs/AlGaAs QW (sample #659) and the data are shown in Fig. 4.7(a)-(c). The overlap of the Landau level can affect the width of the transitions: in the simplest possible model the overlap increases the transition width due to the simultaneous sweep through the extended states of one Landau level and the localized states of the neighboring level.

This conclusion about additional widening of the higher PP transitions is corroborated by the fact that the absolute width of the $3 \rightarrow 2$ and $4 \rightarrow 3$ PP transitions at 0.14 K (at the lowest T shown in Fig. 5.10) is obviously larger than the one for the $2 \rightarrow 1$ PP transition. This is in contradiction with the Landau level addition transformation, which predicts the same width $\Delta\nu$ (in terms of filling factor) for all resolved PP transition at fixed temperature (see Section 3.4).

Our biggest concern, however, about extraction of the critical exponent from the higher PP transitions is rather technical. Considering data sets in the entire range of accessible temperatures, we have to admit that only the $2 \rightarrow 1$ PP transition is properly separated from the other transitions. Determination of the width of the $3 \rightarrow 2$ and $4 \rightarrow 3$ PP transitions, as can be seen from Fig. 5.10, requires a non-trivial approach, especially at high temperatures, where the minimum between the two peaks disappears. Unfortunately, in Ref. [14] the method used for extracting the width of the transitions is not described. As far as we know, there is no model, which predicts the shape of $\rho_{xx}(\nu)$ curve for overlap-

[1] According to theory, the maximum of the longitudinal conductivity (not resistivity) corresponds to the critical filling factor. At critical filling, the resistivity has a crossing point for the $\rho_{xx}(\nu)$ curves measured at different T. The value of the resistivity at the crossing point for the $2 \rightarrow 1$ PP transition is $\rho_{xx}(\nu_c) = 0.2h/e^2$, which is 80% of the peak height.

ping Landau levels at finite temperature. Therefore, we can not exclude that the data of the transition width extracted by Wei *et al.* may contain systematic errors, due to limitation of the model chosen to calculate the width.

The same is, basically, true for the Hall resistance data. It is fair however to say, that for $T < 1$ K the temperature dependence of the maximum slope of the Hall resistance for the $3 \rightarrow 4$ and $4 \rightarrow 5$ PP transitions can roughly be approximated by a power law dependence with exponent close to 0.4. Therefore, at this point we confirm the results of Ref. [14].

Taking into account all mentioned experimental difficulties, we arrive at the conclusion, that the identical value of κ for the different PP transitions reported in Ref. [14] is coincidental, rather than universal.

In this thesis we will not analyze the effect of inhomogeneities on PP transitions higher than $2 \rightarrow 1$. However, in Chapter 7 we offer simple qualitative arguments, which show that the higher the transition index, the stronger the effect of inhomogeneities is on the width of the peak in the $\rho_{xx}(\nu)$ data.

5.5. Conclusions

In this chapter we have presented the results of a thorough magnetotransport study on an InGaAs/InP heterostructure in magnetic fields up to 30 T. We use the same sample as Wei *et al.* in Ref. [14], *i.e.* the publication which triggered intensive studies of critical behavior in quantum Hall systems. Compared to the experiments carried out by Wei *et al.*, we extended the range of the magnetic field in order to include the PI transition ($B_c \approx 26.4$ T). The transport coefficients were measured at different sets of potential contacts of the Hall bar for both, positive and negative, polarities of the magnetic field. Since the electron density and the transport mobility were found to be the same as reported in the paper by Wei *et al.*, our experiment allows us to verify some key statements of the original publication. We find that the PI and PP transitions studied on sample HPW-#59 over a broad temperature range demonstrate qualitatively different behavior.

PI transition:

• Below 2 K, the magnetoresistance data obey scaling behavior with a critical exponent $\kappa = 0.58$, which differs from the "universal" results of Wei *et al.* who obtained $\kappa = 0.42$ for three PP transitions investigated.

• Below 2 K the curves $\rho_{xx}(\nu)$ measured at different T have a well defined crossing point at $\nu_c = 0.53$ and $\rho_{xx}^c \approx h/e^2$, which separates the insulating from

the quantum Hall phase.

• The Hall resistance data measured at $T = 0.6$ K and averaged over both polarities of the magnetic field indicate that at low temperatures the Hall resistance stays quantized through the PI transition. Therefore, in high magnetic field the low mobility 2DEG in the InGaAs/InP heterostructure is a quantized Hall insulator.

• From both previous conclusions it follows, that a quantum critical point for the PI transition in the $\sigma_{xx}(\sigma_{xy})$ plane is located at $\sigma_{xx} = \sigma_{xy} = 1/2$, as expected from the theory

• Above 2 K, the 2DEG is not in the scaling regime as can be concluded from the deviation of $\nu_0(T)$ from power law behavior and the absence of a crossing point at ν_c in the $\rho_{xx}(\nu)$ data.

• Small deviations of $\nu_0(T)$ at the lowest temperatures are, most likely, caused by macroscopic sample inhomogeneities.

• Using misalignment of the Hall contacts we are able to extract information about macroscopic sample inhomogeneities beyond the "gradient approximation". Two different methods for estimating the magnitude of inhomogeneities are used. From the shift of the crossing point at the PI transition, as well as from the shift of the peak at the PP transition, we estimate a lower limit of the carrier density variation in sample HPW-#59 of the order of 3%.

PP transition:

• The magnetoresistance data extracted from the $2 \rightarrow 1$ PP transition do not satisfy important conditions for scaling, which include: a) crossing point at the critical filling factor of the curves $\rho_{xx}(\nu)$ and $\rho_{xy}(\nu)$ measured at different T; b) a temperature independent value of the peak maximum ρ_{xx}^{max}; c) power law temperature dependence of the parameter ν_0, which is proportional to the width of peak in the $\rho_{xx}(\nu)$ data and the maximum slope of the $\rho_{xy}(\nu)$ curve.

• Despite the obvious absence of scaling signatures, the linear fit of the $\nu_0(T)$ data on a double logarithmic scale yields $\kappa = 0.42$, which coincides with the value obtained in Ref. [14]

• The observed deviations from scaling behavior for the $2 \rightarrow 1$ PP transition are attributed to macroscopic sample inhomogeneities.

• Analyzing the higher index PP transitions we found that universality of the critical exponent κ as reported by Wei *et al.* was rather coincidental.

At the end it is important to notice that the temperature dependence of the parameter ν_0 obtained from the PI transition measurements on sample HPW-#59 will be used in the numerical simulation of the transport properties of the inhomogeneous 2DEG presented in Chapter 7.

6

Plateau-Insulator Transition in an InGaAs/GaAs Quantum Well

In the previous chapter we presented magnetotransport experiments for the PP and PI transitions in an InGaAs/InP heterostructure. The sample used in these investigations was the same as the sample used by Wei *et al.*in their pioneering experiments on scaling of the quantum Hall effect [14]. We showed that the data for the PP transition are affected by small but not negligible macroscopic inhomogeneities, while the PI transition data are less sensitive to inhomogeneities. Taking into account that sample HPW-#59 has been made more than 15 years ago it is of paramount importance to check our findings using newer samples of better quality.

In this chapter, we present the results of transport measurements on a 2DEG in an InGaAs/GaAs quantum well (QW). The wafer from which the Hall bars were prepared was grown by molecular beam epitaxy (MBE), which provides better control over the growth process than MOCVD used for making the InGaAs/InP heterostructure discussed in the previous chapter.

One of the key reasons for the intensive study of the sample described in this chapter is the possibility to tune its electron density in a range convenient for our magnetotransport set-ups. This allows us to check universality of the critical exponent κ for various carrier concentrations.

Furthermore, precise etching of the Hall bar largely excludes misalignment of the Hall contacts, which in turn allows more accurate measurements of the Hall resistance through the plateau-insulator (PI) transition. The deviation of the Hall resistance from the quantized value at $T \gtrsim 1$K enables us to extract another important parameter, the so-called irrelevant critical exponent $\tilde{y}_\sigma$, which gives access to modelling the flow diagram in the $\sigma_{xx}(\sigma_{xy})$ plane.

6.1. Experiments on samples with tunable carrier density

The carrier density is an important parameter of the 2DEG. For instance, as discussed in Chapter 2, the value of the electron concentration determines whether the PI transition can be accessed within the available magnetic field range. The very first experiments on the quantum Hall effect were performed using samples of which the density of the 2DEG was varied, rather than the magnetic field [1]. This was accomplished by using a metallic gate on top of the Hall bar. By applying a constant voltage between the gate and a common ground the carrier density can be modified. This method is suitable for all kinds of samples and allows one to change the density over a broad range of values. The limiting factor is the electrostatic breakdown of the gate. We prepared several gated samples, however the results were usually disappointing. Especially we found that covering of the samples with the gate made them more inhomogeneous compared to the initial Hall bar. Consequently, these samples were not suitable for our research purposes. In order to tune the carrier density we relied on another well known method, namely, illumination with an infra-red LED at low temperatures. This method, however, should also be used with care. Typical problems that we encountered are relaxation of the carrier density after illumination and induction of parallel conductivity. Also some samples were not photosensitive at all. An example of such a sample is the rather high mobility InGaAs/InP heterostructure C-759-#1 (see Fig. 2.8c). Despite the above mentioned difficulties, we had access to a number of samples, for which illumination is a perfect instrument to increase the carrier concentration and to improve the homogeneity of the 2DEG.

The sample described in this chapter is an $In_{0.2}Ga_{0.8}As/GaAs$ quantum well grown by MBE. According to the growth sequence, the 2DEG is located in a 12 nm thick $In_{0.2}Ga_{0.8}As$ layer, separated from the doping layer by a 20 nm thick

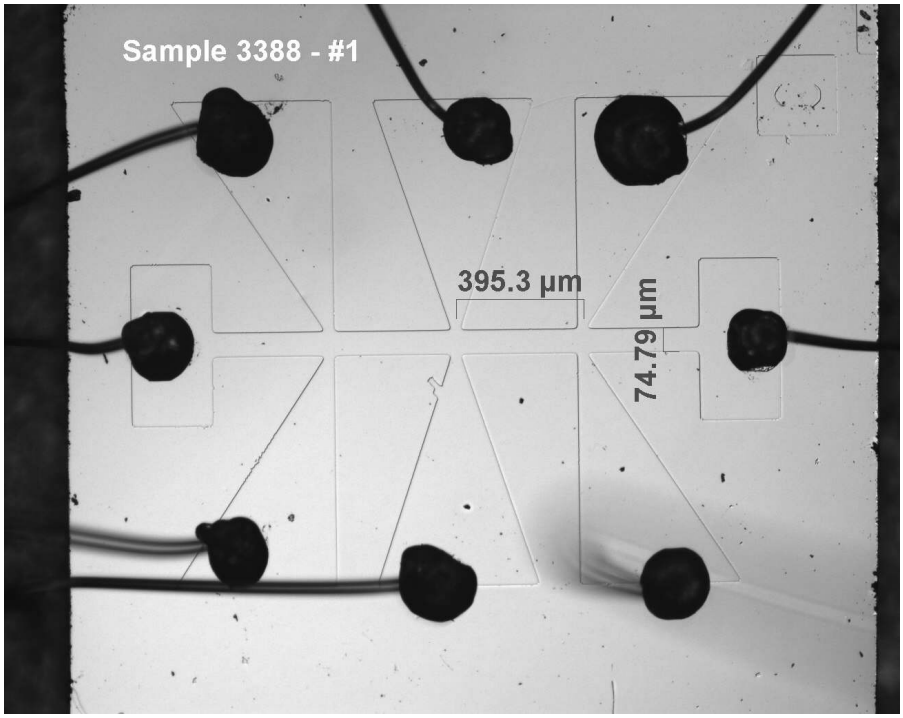

Figure 6.1: Sample 3388-#1 and its dimensions.

spacer. The sample was prepared without a cap-layer. A Hall bar was etched by photolithography as shown in Fig. 6.1. It has 6 potential and 2 current contacts enabling one to measure the Hall resistance from 3 different pairs of contacts and the longitudinal resistance - from 4 pairs. The geometrical factor of the Hall bar is $W/L = 0.19$ $(L/W = 5.2)$.

This particular sample, labelled as 3388-#1, is insulating in the dark. Persistent photoconductivity is found after pulse illumination at helium temperatures ($T = 4.2$ K). The low field Hall resistance measured a few seconds after illumination and one day later were identical, hence no relaxation of the electron density occurred. The carrier concentration in the sample can be varied smoothly between zero (insulating sample) and 4×10^{11} cm^{-2} with an accuracy better than 1%. High precision of the carrier density was achieved by systematic increase of the pulse duration (usually increasing from 1 to 20 seconds), as well as by accurate control of the current through the LED. For this we used a current source Keithley 2400. Illumination, typically started from 1 μA and subsequently the current was increased every time by a factor 2, until the desired electron density of the 2DEG was obtained. The obvious disadvantage of illumination is its irreversibility. In order to restore the initial low density, the

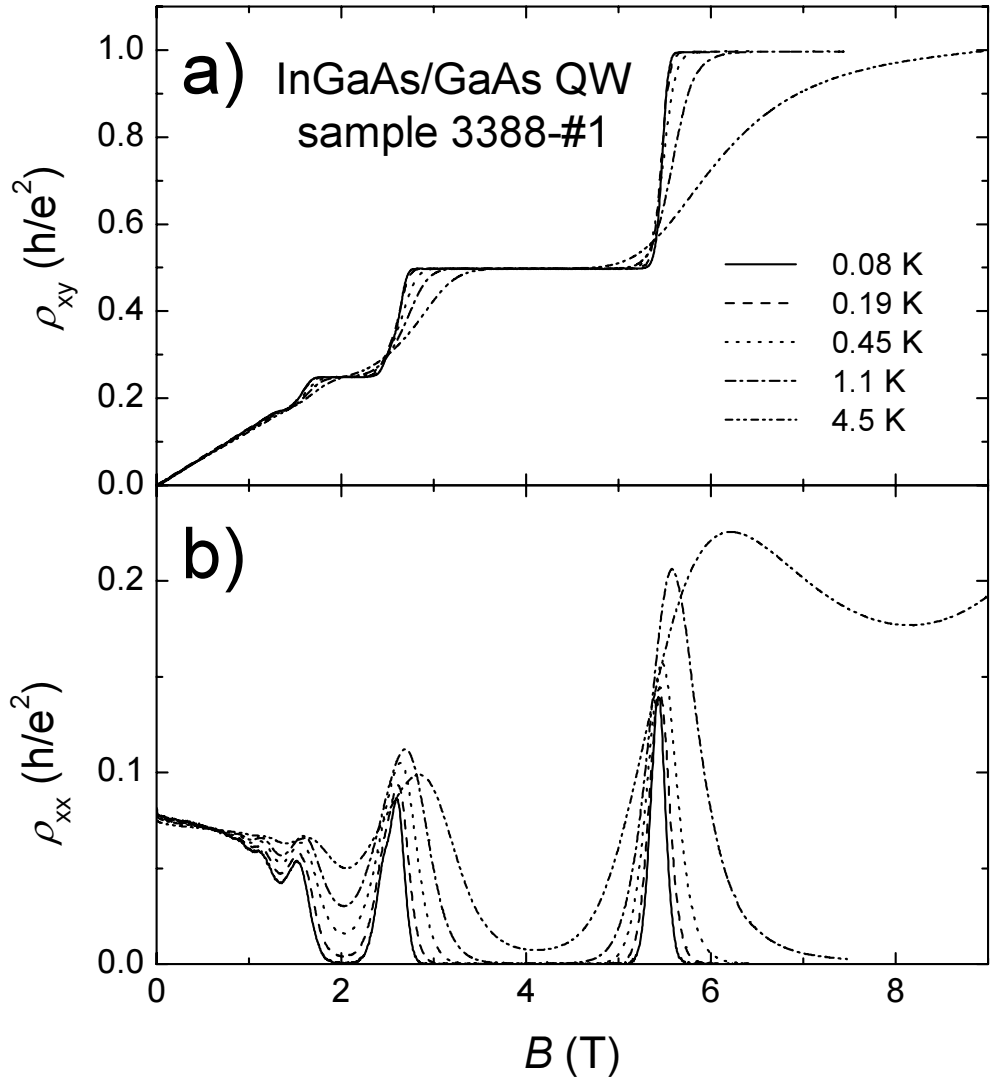

Figure 6.2: Hall (a) and normalized longitudinal resistance (b) of sample 3388-#1 as a function of magnetic field at different temperatures as indicated.

sample has to be warmed up to relatively high temperatures ($T \sim 100$ K) and cooled down again.

In this Section we present three series of measurements on sample 3388-#1: two of them were carried out in the GHMFL (Grenoble, France) and a third set of data was taken at the Van der Waals - Zeeman Institute. In Grenoble, experiments were carried out in magnetic fields up to 20 T, while in Amsterdam the accessible magnetic field was limited to 9 T. In all three series of measurements, data were taken at different carrier densities.

Typical magnetotransport traces measured in Amsterdam in the temperature range 0.08-4.2 K are shown in Fig. 6.2. Here the electron density and trans-

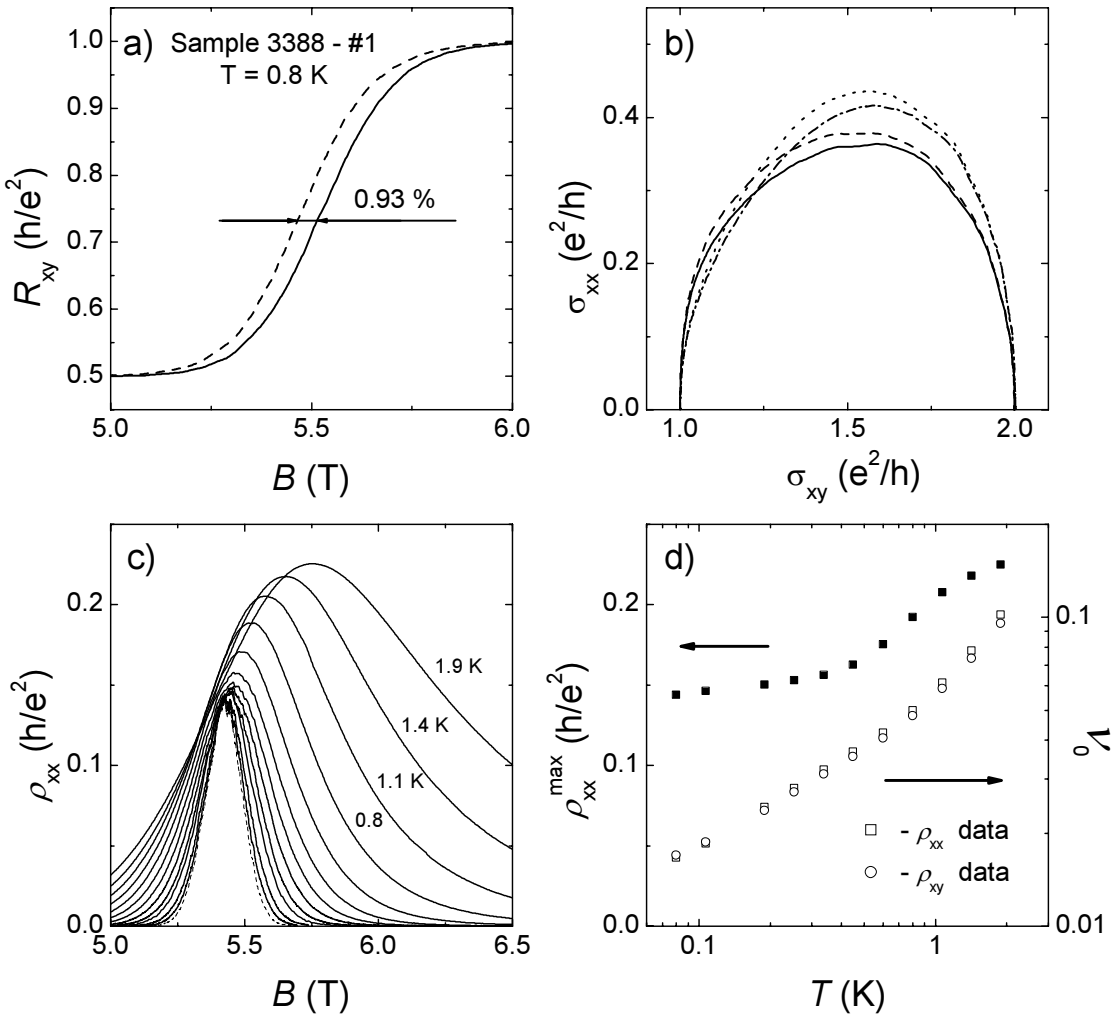

Figure 6.3: a) Hall resistances measured at two pairs of contacts on sample 3388-#1 at $T = 0.8$ K. The density difference is about 1%; b) $\sigma_{xx}(\sigma_{xy})$ diagram at $T = 0.8$ K obtained by combining magnetoresistance curves measured at different contacts; c) The magnetoresistance of sample 3388-#1 at the $2 \rightarrow 1$ PP transition measured at temperatures of 1.9, 1.4, 1.1, 0.8, 0.6, 0.45, 0.34, 0.29, 0.14, 0.08 K (all shown by solid lines) and at base temperature of the dilution refrigerator (dashed line). Curves measured below 0.8 K are not labelled; d) The temperature dependencies of the magnetoresistance peak height (left axis) and the parameter ν_0 (right axis) extracted from the longitudinal and Hall resistances at the $2 \rightarrow 1$ PP transition.

port mobility are $n = 1.9 \times 10^{11}$ cm^{-2} and $\mu = 16000$ cm^2/Vs, respectively. The transport mobility is fairly low, and as a result for $T < 1.5$ K only the $2 \rightarrow 1$ PP transition is resolved. As usually in presentation of the experimental data, the notation ρ_{xx} indicates the normalized longitudinal resistance $\frac{W}{L}R_{xx}$ (which can be quite different from the true longitudinal resistivity). As expected for an accurately etched Hall bar, field reversal changes only the sign and not the absolute value of the Hall voltage. Despite of broad plateaux in $\rho_{xy}(B)$ and the sharp peak in $\rho_{xx}(B)$ for the $2 \rightarrow 1$ PP transition, the density gradient measured between the different pairs of the Hall contact is significant. In Fig. 6.3a we show the Hall resistances measured at $T = 0.8$ K at the middle and right pairs of potential contacts. From the shift between the two curves we conclude that the density difference is of the order of 1%. Further illumination generally leads to a decrease of the gradient, however the simultaneous increase of the density pushes the PI transition to above the accessible magnetic field range. Combining the Hall data shown in Fig. 6.3a, with the longitudinal resistance measured on the same set of (four) potential contacts, results in four slightly different $\sigma_{xx}(\sigma_{xy})$ curves shown in Fig. 6.3b. A dramatic difference between this plot and the one shown in Fig. 4.5c is that all four curves have a peak value, well below the theoretically expected value $\sigma_{xx}^{max} = 0.5e^2/h$. This cannot be explained by merely a 1% carrier gradient. Just like in the experiments on the InGaAs/InP heterostructure discussed in Chapter 5, we observed a fine structure in $\rho_{xx}(B)$ curves at low T (see Fig. 6.3c) and a strong dependence of ρ_{xx}^{max} on temperature (Fig. 6.3d). Despite of the significant gradient, there is no large difference in the peak height ρ_{xx}^{max} measured on different contacts and for different magnetic field polarities. The reason for this is the small geometrical factor W/L, which makes the difference between the $\rho_{xx}(B)$ curves measured at the opposite contacts about 5 times smaller than the difference between the $R_{xy}(B)$ curves. This makes the reflection symmetry less pronounced compared to the case of sample #659 described in Chapter 4. Consequently, variation of the peak height with the temperature, $\rho_{xx}^{max}(T)$, is quite similar for all sets of contacts. The solid symbols in Fig. 6.3d show the $\rho_{xx}^{max}(T)$ dependence extracted from the data presented in Fig. 6.3c. Using these data, we also extract the temperature dependence of the parameter ν_0 shown by open squares in Fig. 6.3d together with $\nu_0(T)$ obtained from the Hall data (open circle symbols). Again, the PP transition does not obey the theoretically expected behavior: firstly, the peak height is lower than $0.25h/e^2$ and secondly, $\nu_0(T)$ does not follow power law behavior over the

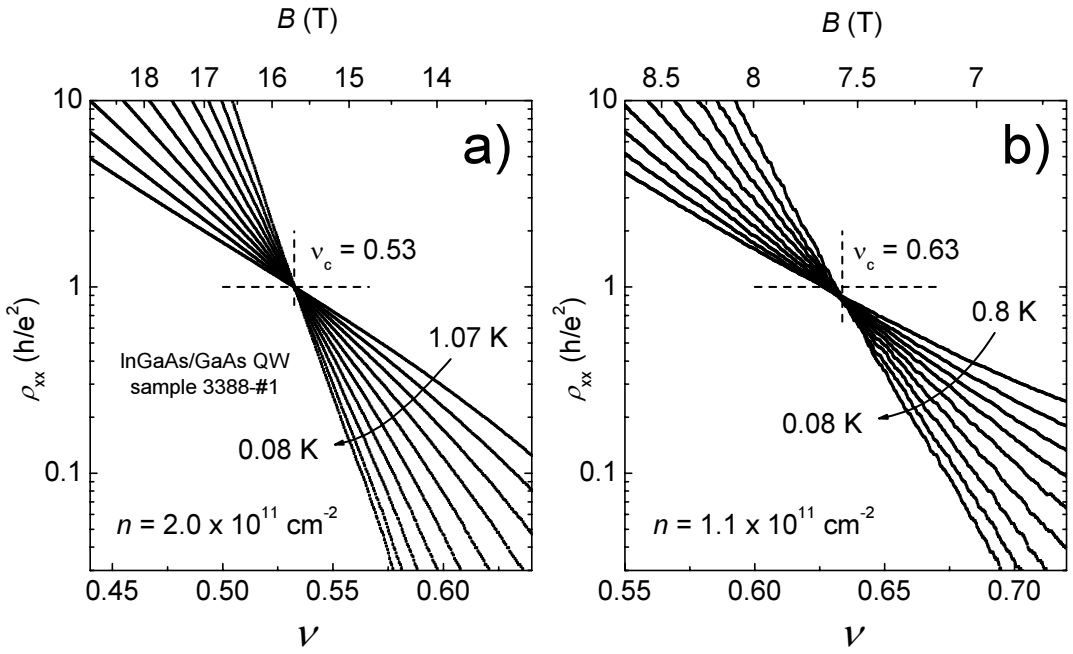

Figure 6.4: The normalized longitudinal resistance of sample 3388-#1 as a function of the filling factor ν and the magnetic field B (upper axis) for two values of the electron density $n = 2.0 \times 10^{11}$ cm^{-2} (a) and $n = 1.1 \times 10^{11}$ cm^{-2} (b) at temperatures 1.07 (in (a) only), 0.80, 0.60, 0.45, 0.34, 0.26, 0.19, 0.14, 0.107 and 0.08 K. The crossing point indicates the PI transition. The horizontal dashed line corresponds to the level $\rho_{xx} = h/e^2$, at which the crossing point is expected for the homogeneous sample. The arrow shows the direction of decreasing temperature.

entire temperature range. The fit of the low temperature parts (below 1 K) of $\nu_0(T)$ in Fig. 6.3d yields exponents $\kappa = 0.48$ and $\kappa = 0.45$ for the longitudinal and Hall resistance data, respectively.

Next we consider the PI transition. Magnetotransport data covering the PI transition were taken at three different densities: $n = 1.1 \times 10^{11}$ cm^{-2}, 1.5×10^{11} cm^{-2} and 2.0×10^{11} cm^{-2}. The first data set, at low density was measured at the WZI, using the Oxford 200S dilution refrigerator, equipped with a 9 T superconducting magnet, while the other two data sets were taken at GHMFL in magnetic fields up to 20 T.

In Fig. 6.4a we show the normalized longitudinal resistance as a function of the filling factor for the highest density $n = 2.0 \times 10^{11}$ cm^{-2}. Notice that the density was determined in the usual manner from the slope of $R_{xy}(B)$ in low magnetic field. The measurement frequency was as low as 2.1 Hz in order to reduce the out of phase signal as much as possible. Similarly to the data

presented in the previous chapter, the critical filling factor for the PI transition can be identified by the crossing point of the $\ln \rho_{xx}$ *versus* ν curves measured at different T, *i.e.* $\nu_c = 0.53$. The normalized resistance at the critical point is $\rho_{xx,c} = h/e^2$ to within 1%. The crossing point is well defined in the entire temperature range investigated (0.8 - 1.07 K). In the vicinity of ν_c, the normalized resistance ρ_{xx} follows the empirical law [94]:

$$\ln(\rho_{xx}/\rho_{xx,c}) = -\Delta\nu/\nu_0(T), \tag{6.1}$$

where $\Delta\nu = \nu - \nu_c$. The second data set measured in Grenoble (not shown) at a lower density, $n = 1.5 \times 10^{11}$ cm^{-2}, is very similar to the one presented in Fig. 6.4a. The only difference being that the PI transition takes place at lower field and the crossing point appears at $\nu_c = 0.58$. The results of measurements at the lowest carrier density $n = 1.1 \times 10^{11}$ cm^{-2} are shown in Fig. 6.4b. We notice a further increase of the critical filling factor, which is now $\nu_c = 0.63$, and a significantly lower (more than 10%), value of $\rho_{xx,c}$ at the crossing point. The horizontal dashed line corresponds to $\rho_{xx} = h/e^2$, which is the value expected from the theory for the longitudinal resistance at the critical filling factor. Another qualitative difference is related to the shape of the curves $\rho_{xx}(\nu)$. At the highest density ($n = 2.0 \times 10^{11}$ cm^{-2}, Fig. 6.4a) the curves $\rho_{xx}(\nu)$ practically satisfy the condition of particle-hole symmetry:

$$\rho_{xx}(\nu - \nu_c) = \rho_{xx}^{-1}(\nu_c - \nu) \tag{6.2}$$

which is equivalent to the requirement that the crossing point is the center of symmetry for the resistance traces. In contrast, at low electron density (Fig. 6.4b) the particle-hole symmetry is clearly violated.

The linear fit of the data near the critical point gives us the temperature dependence of the parameter ν_0, which is inversely proportional to the slope of the fitted lines. The dependence $\nu_0(T)$, for all three values of the carrier density, is shown in Fig. 6.5. In this double logarithmic plot all sets of data fall on straight lines. The quality of data undoubtedly allows to conclude that $\nu_0(T)$ obeys power law behavior. The values of the critical exponent κ extracted from Fig. 6.5 are 0.58, 0.54 and 0.53. These values show a small spread, beyond the experimental uncertainty estimated to be of the order of 0.02. It is important to note that the numerical value of κ at the highest density is the same as the value obtained for the PI transition in the InGaAs/InP heterostructure ($n = 3.4 \times 10^{11}$ cm^{-2}) reported in Chapter 5. It is also, within the experimental error, equal to

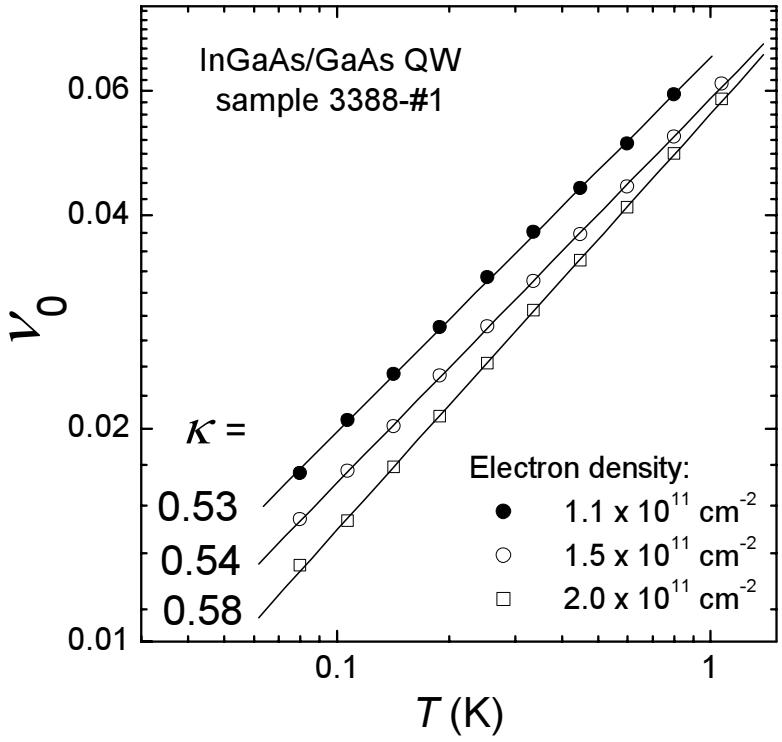

Figure 6.5: The temperature dependence of the parameter ν_0 at three different electron densities as indicated. All curves obey perfect scaling behavior.

$\kappa = 0.57$ measured on a second InGaAs/InP heterostructure ($n = 2.2 \times 10^{11}$ cm^{-2}) reported in Ref. [17]. Nevertheless, the data in Fig. 6.5 indicate that κ is a weak function of n. At the same time the decrease of κ at lower n is accompanied by an increase of the critical filling factor ν_c, or in other words, ν_c progressively deviates from the theoretically expected value 0.5. In the following paragraph we offer a tentative explanation for this phenomenon.

For this we have to realize that the total filling factor ν is the sum over the filling factor of the individual Landau levels:

$$\nu = \sum_i \nu_i. \tag{6.3}$$

If the Landau levels do not overlap, the PP transitions take place at half-integer values of ν, and the PI transition takes place at $\nu = 0.5$. Such a situation for the PI transition is most likely to occur in samples with a high carrier density. In this case a strong magnetic field is needed to attain the PI transition and consequently the Landau levels are well separated due to Zeeman splitting. For low density samples, the field needed to attain the PI transition is smaller and the Landau levels might still overlap. This means that at the PI transition

the second Landau level ($i = 2$), which is often referred in literature as $0\downarrow$, is partially occupied as well and $\nu = \nu_1 + \nu_2$. The point is that the magnetic field is inversely proportional to ν, while the measured resistance depends only on ν_1. At these high fields, states in the $0\downarrow$ Landau level do not contribute to the transport, because they are localized. This offers the explanation for the large difference between the measured value of ν_c and the expected value 0.5 for low-density samples. The difference $\nu_c - 0.5$ is the filling fraction of the second Landau level when the lowest Landau level is half-full (critical filling).

Apart from the shift of ν_c, the overlap with the second Landau level increases the width of the PI transition, which in turn results in an increase of ν_0. As follows from Fig. 6.5 such an increase indeed takes place: the lower the density, the higher the curve $\nu_0(T)$ is located in the plot. Another consequence of the overlapping of Landau levels is violation of the particle-hole symmetry. The second Landau level has a higher density of the localized states at the "plateau side" of the PI transition than at the "insulating side". This leads to a distortion at the "plateau side", *i.e.* an effective stretching along the ν-axis due to additional states, which do not contribute to the transport. Such a behavior can be seen in Fig. 6.4b, while in Fig. 6.4a the data look rather symmetric with respect to the critical point.

The increase of $\nu_0(T)$, discussed in the previous paragraph, can be derived analytically. The parameter ν_0 is inversely proportional to the slope of $\ln \rho_{xx}$ vs ν near the crossing point ν_c:

$$\nu_0(T) = -\left(\frac{\partial \ln \rho_{xx}(\nu_1, T)}{\partial \nu}\right)^{-1} \tag{6.4}$$

where we take into account that the resistivity depends only on the filling fraction ν_1 in the lowest Landau level. If the carrier density is constant, ν_1 is a function of ν and the relation between them does not depend on temperature. Therefore:

$$\nu_0(T) = -\left(\frac{\partial \ln \rho_{xx}(\nu_1, T)}{\partial \nu_1}\frac{\partial \nu_1}{\partial \nu}\right)^{-1} = \nu_{0,L}(T)\left(\frac{\partial \nu_1}{\partial \nu}\right)^{-1} \tag{6.5}$$

where $\nu_{0,L}(T)$ is the "true" temperature dependence of ν_0 in case of completely separated lowest Landau levels. Since ν_1 is a smooth monotonic function of ν and $\nu_1 \leq \nu$, the quantity $\partial\nu_1/\partial\nu$ is always smaller or equal to 1. Therefore, the last equation explains higher values of ν_0 at lower densities (and stronger overlap) seen in Fig. 6.5. Note that this model does not explain the small decrease of κ with decrease of the density since $\partial\nu_1/\partial\nu$ is temperature independent.

A further comment about the difference observed between the curves in Fig. 6.5 is in place. The temperature reading is affected by the small errors due to magnetoresistance of the thermometer exposed to strong magnetic field. This problem was discussed in much detail in Chapter 2, where we showed that the measured magnetoresistance of the RuO_2 thermometer does not affect the measured value of the exponent κ, but nevertheless can cause a shift of the whole curve $\nu_0(T)$ along the T-axis (with logarithmic scale). This shift, however, cannot be responsible for the difference between the curves in Fig. 6.5 because it should show the opposite sign: the curves $\nu_0(T)$ for a higher carrier density (higher magnetic fields) should be higher on the plot. This indicates that the effect of overlap of the Landau levels, might even be stronger than follows from Fig. 6.5.

Because the misalignment of the Hall potential contacts is relatively small for this sample, it is possible to determine the correct value of the Hall resistance at the PI transition and determine the so-called irrelevant critical exponent $\tilde{y}_\sigma$ [10]. In the first order approximation $\tilde{y}_\sigma$ describes the vertical flow in the $\sigma_{xx}(\sigma_{xy})$ plane near the quantum critical point (QCP), in contrast to the relevant critical exponent κ, which determines the horizontal flow away from the QCP. The exponent $\tilde{y}_\sigma$ can be extracted from the temperature dependence of the Hall resistance at the critical field [52]:

$$\rho_{xy} = 1 + \eta(T), \quad \eta(T) = (T/T_1)^{\tilde{y}_\sigma} \tag{6.6}$$

where T_1 is a fit parameter. In Fig. 6.6 we present the magnetic field dependence of the averaged Hall resistance at several temperatures. The extracted temperature dependence of the parameter η is shown in the inset, together with the result of a fit by a power law function (dashed line). We find $\tilde{y}_\sigma \approx 2.6$ and $T_1 \approx 4.5$ K, which are comparable with $\tilde{y}_\sigma \approx 2.5$ and $T_1 \approx 9.8$ K obtained in the InGaAs/InP heterostructure [52].

6.2. An alternative way of extracting the critical exponent

In order to corroborate the scaling results described in Section 6.1, we next present an alternative way of investigating scaling at the PI transition. Notice, that for most of the scaling data sets reported in this thesis we have chosen the temperatures T_{si} at which the field is sweeped such that the isotherms are

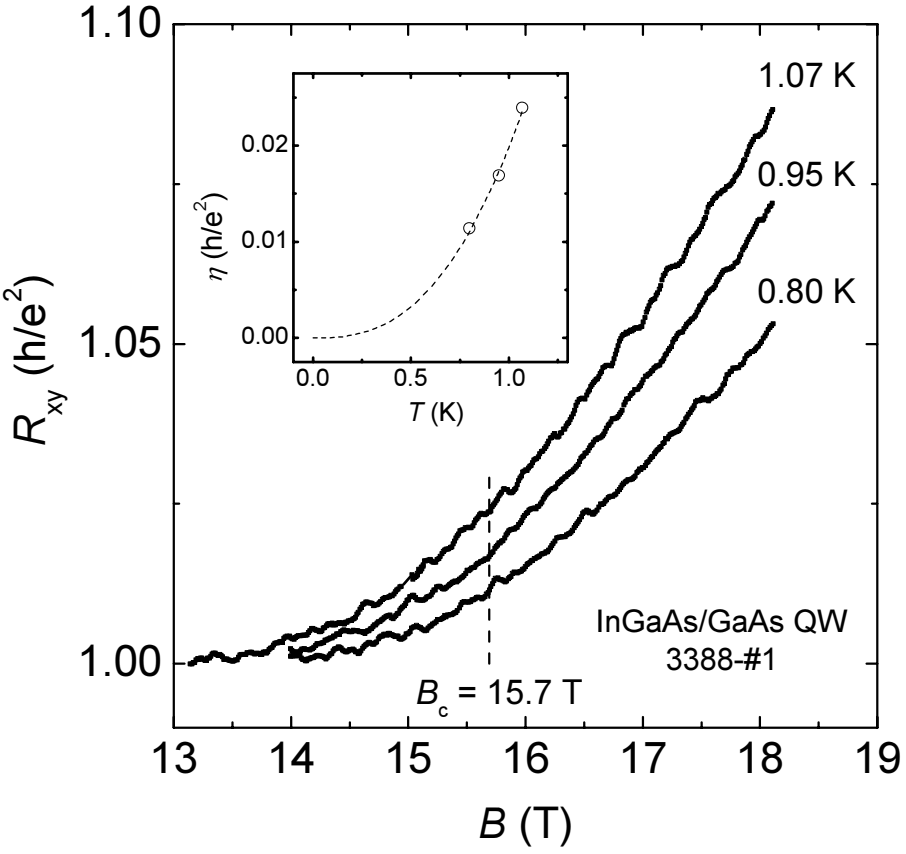

Figure 6.6: The averaged Hall resistance $R_{xy}(B)$ (after magnetic field reversal) of InGaAs/GaAs QW (sample 3388-#1, $n = 2. \times 10^{11}$ cm^{-2}) at several temperatures. From the temperature dependence of the deviation of the Hall resistance from the quantized value h/e^2 at the critical field B_c (see inset) the irrelevant critical exponent $\tilde{y}_\sigma = 2.6$ was obtained.

equally spaced on a logarithmic temperature scale, *i.e.* $\ln T_{si} = \ln T_{s0} - \alpha i$. Here T_{s0} and α are constants specific for each experiment and i is an integer which labels the different curves. In case of scaling $\ln \nu_0(T) = \kappa \ln T$. Hence, the parameter ν_0 changes with index i as

$$\ln \nu_0(T_{si}) = -\alpha\kappa i + const \tag{6.7}$$

Taking the logarithm of Eq. (6.1) and taking into account Eq. (6.7), we obtain

$$\ln |\ln \rho_{xx}| = \ln |-\Delta\nu| + \alpha\kappa i - const \tag{6.8}$$

where ρ_{xx} is expressed in units of h/e^2. The absolute value here is used to take into account both positive and negative values of $\Delta\nu$ and $\ln \rho_{xx}$, depending whether $\nu < \nu_c$ or $\nu > \nu_c$. Therefore, under the condition of scaling, a

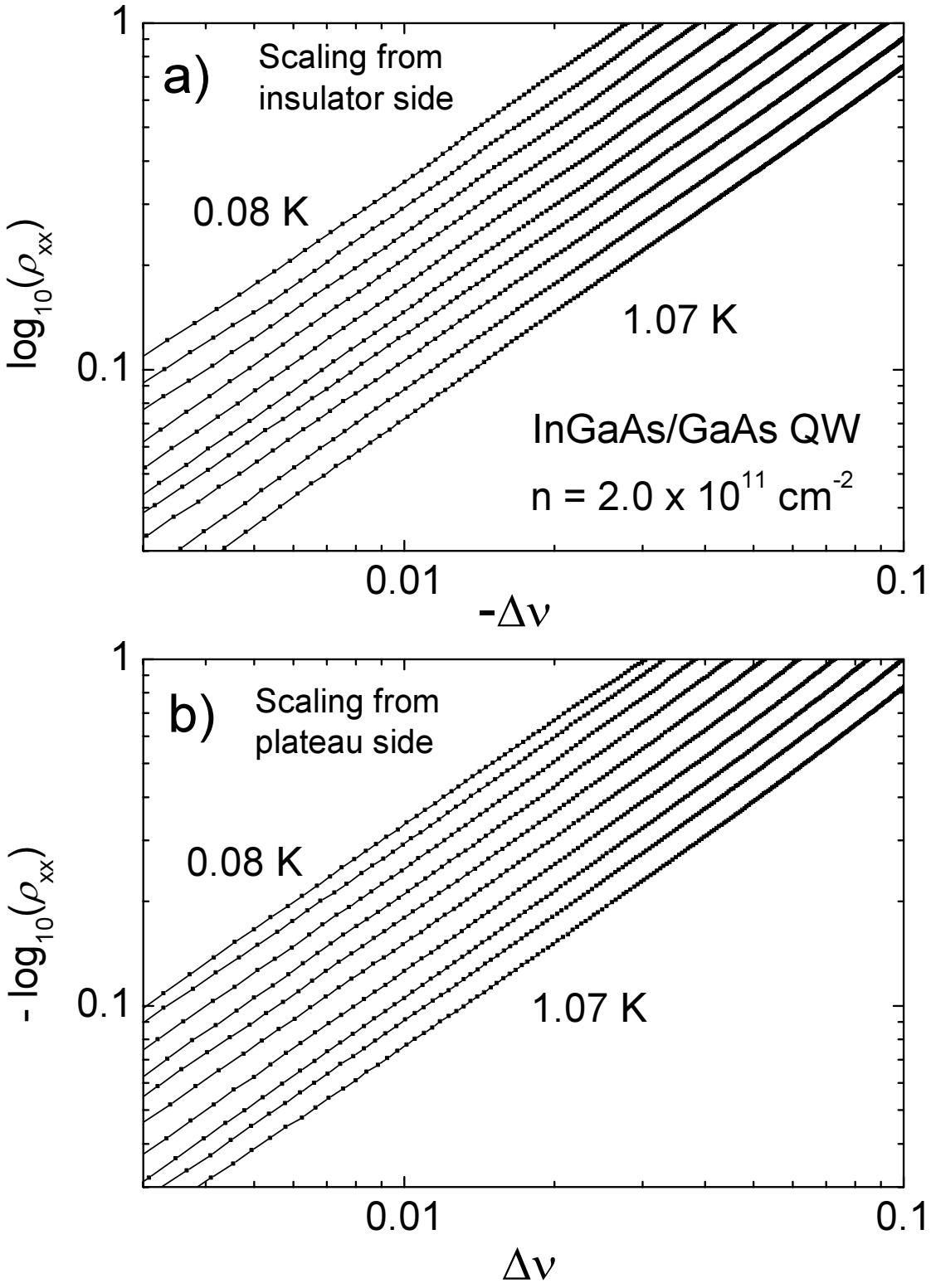

Figure 6.7: The ρ_{xx} data for the InGaAs/GaAs QW (B_c = 15.7 T) from Fig. 6.4a, plotted versus $\Delta\nu$ in the insulating (a) and quantum Hall phase (b). The axis are rescaled to illustrate the validity of Eq. 6.8. Equally spaced parallel lines signify scaling.

plot of $\ln|\ln\rho_{xx}|$ vs. $\ln|-\Delta\nu|$ transforms the experimental data into sets of parallel lines, equally spaced by the amount $\alpha\kappa$ along the abscissa. This is illustrated in Fig. 6.7 for the same data set shown in Fig. 6.4. The derived values of κ are identical to the values quoted above. The advantage of this method, which relies on the presence of a sharp well-defined crossing point, over the "traditional" method is that no fitting procedure is needed to visualize scaling behavior. Hence, errors in the determination of the critical exponent due to arbitrary fitting constraints are minimized. Besides, scaling behavior can be verified away from the critical field B_c, at relatively large $\Delta\nu$ and from both sides of the PI transition. This is quite a step forward compared to the traditional method, where only a small part of the data around B_c is used to calculate κ. Furthermore, this method allows for a direct check of particle-hole symmetry, $\rho_{xx}(\Delta\nu) = 1/\rho_{xx}(-\Delta\nu)$. In this case, the curves for $\nu > \nu_c$ (Fig. 6.7a) and $\nu < \nu_c$ (Fig. 6.7b) should be identical as can be verified by plotting the data from both panels in the same graph. In fact, by doing so we did not obtain perfect coincidence between the "insulating" and "plateau" parts of the PI transition. At high absolute values of $\Delta\nu$ the lines on the "plateau" side are slightly more dense than on the "insulating" side. This means that the exponent obtained from magnetoresistance data is somewhat smaller at the "plateau" side, where the overlap with the next Landau level is stronger. The difference is of the order $\sim 0.01 - 0.02$, which is comparable to the difference between the values of κ extracted in the traditional way for different densities. This is yet another indirect indication that the exponent κ is not a function of the carrier density. The small decrease of κ observed in transport measurements is likely due to the overlap of Landau levels, being stronger at lower electron densities.

6.3. Conclusions

In this chapter we have presented results of magnetotransport measurements in an InGaAs/GaAs QW with tunable electron density. We conclude the following:

- despite of an advanced growth procedure (MBE) our InGaAs/GaAs QWs turn out to exhibit macroscopic sample inhomogeneities on a scale comparable to the size of the sample, which hamper the proper study of the critical behavior of the PP transitions;
- in contrast, the PI transition obeys perfect scaling behavior over a broad temperature range at different values of the electron density;

- at the highest electron density ($n = 2.0 \times 10^{11}$ cm^{-2}) we extract the critical exponent $\kappa = 0.58$, which coincides with the values of κ measured at the PI transition in InGaAs/InP heterostructures.
- at lower electron densities we observe a minor decreasing of κ accompanied by a violation of particle-hole symmetry and a deviation of the critical filling factor ν_c from the theoretically expected value 0.5 towards higher values. We attribute these effects to overlap of the Landau levels at moderate magnetic fields in the low-density low-mobility 2DEG.
- by measuring the deviations of the Hall resistance from the quantized value h/e^2 at the PI transition at elevated temperatures ($T \sim 1$ K), we extract the irrelevant critical exponent $y_\sigma = 2.6$.

We also proposed an alternative way of presenting scaling behavior at the PI transition. This method does not require a fitting procedure and has a number of advantages compared to the traditional method of analyzing scaling.

7

NUMERICAL SIMULATIONS

7.1. Motivation

The spatial variations in the electron density produce a spatially varying filling fraction ν of the Landau level. Any such macroscopic inhomogeneity in the electron density, no matter how small, will eventually complicate the critical behavior of the electron gas in the limit where T and, hence, the width $\delta\nu$ of the plateau transitions goes to zero. The experimental situation is in many ways similar to that of an ordinary liquid-gas phase transition where, as is well known, inhomogeneity effects due to gravity prevents one from entering arbitrary deep into the critical phase. Unlike the liquid-gas phase transition, however, there hardly exists any detailed study or systematic knowledge on the inhomogeneity problem, especially in low-mobility heterostructures. Transport measurements on the Hall bar geometry at low T usually give rise to rather different results depending on the pairs of contacts that are being used, the polarity of the external field B, *etc*. These annoying and puzzling complications have been the primary reason why the experiments on the Hall bar geometry have so far not provided any reliable information on the details of the scaling functions of the conductivity parameters in the transition regime between adjacent quantum Hall plateaus, notably the peak value and the shape of σ_{xx}. Moreover, the most important and fundamental aspect of the problem, the numerical value of the critical index κ has remained an unsettled experimental problem. In spite of the fact that the original data of H.P. Wei *et al.* [14] have provided an impressive experimental demonstration of a quantum phase transition in the quantum Hall regime over the largest possible range of experimental T, it has remained some-

what uncertain whether the extracted value of the exponent $\kappa = 0.42 \pm 0.04$ is in fact the true critical value, or whether it represents an *effective* exponent resulting from an admixture of quantum critical behavior and sample-dependent effects due to macroscopic inhomogeneities. On the basis of numerical simulations presented in this chapter we claim that the plateau-insulator (PI) transition is generally much less affected by sample inhomogeneities than the plateau-plateau (PP) transitions taken from the same sample. As a result of all this, one can now say that the previously accepted experimental value of the exponent $\kappa = 0.42$ is incorrect.

7.2. Formulation of the problem

The purpose of this Section is to derive a differential equation, which describes the transport properties of an inhomogeneous two-dimensional electron gas exposed to a perpendicular magnetic field and present the relevant boundary conditions. We focus on the Hall bar geometry with current flowing between two metallic contacts. In the subsequent sections the solution of the problem for the special case of a gradient in the electron density and its implication for studying quantum criticality will be given.

The starting point is a system of Maxwell equations in two dimensions (x-y plane). Since we treat the static case, the problem can be reduced to two equations:

$$\nabla \cdot \vec{j} = 0, \tag{7.1}$$

$$\nabla \times \vec{E} = 0 \tag{7.2}$$

The first equation yields the conservation of current flow and the second one imposes the electric field to be rotation free.

We search a solution in the form of a current potential $\phi = \phi(x, y)$, such that the current density $\vec{j} = \nabla \times (\vec{z}\,\phi)$, where $\vec{z}$ is the unit vector perpendicular to the x-y plane. Choosing such a solution the current conservation law is satisfied automatically. The electric field can be expressed in terms of the current potential using the material equation:

$$\vec{E} = \hat{\rho}\vec{j} = \hat{\rho}\nabla\phi, \tag{7.3}$$

where $\hat{\rho}$ is the local resistivity tensor:

$$\hat{\rho} = \begin{pmatrix} \rho_{xx} & \rho_{xy} \\ -\rho_{xy} & \rho_{xx} \end{pmatrix}. \tag{7.4}$$

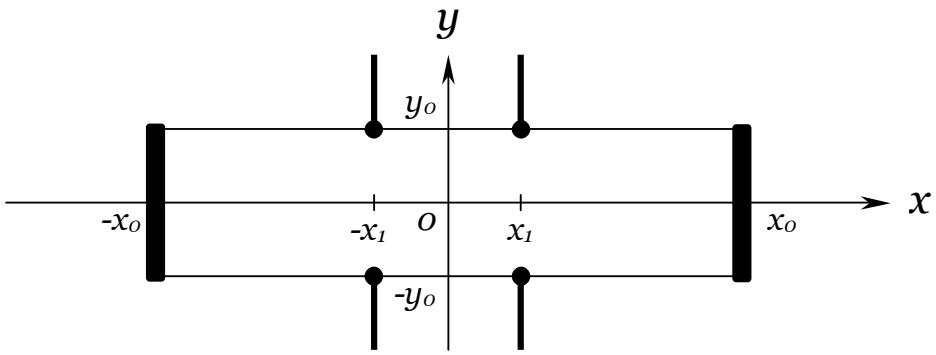

Figure 7.1: Simplified representation of the Hall bar used in the numerical simulations.

In case of an inhomogeneous sample, which is considered here, both components of the resistivity tensor, ρ_{xx} and ρ_{xy}, are functions of x and y.

Substitution of the electric field from Eq. (7.3) transforms Eq. (7.2) into a second order non-linear partial differential equation, which after simplification has the form:

$$\Delta\phi = C(x,y)\frac{\partial\phi}{\partial x} + D(x,y)\frac{\partial\phi}{\partial y} \tag{7.5}$$

with coefficients $C(x,y)$ and $D(x,y)$ depending on the particular distribution of inhomogeneities in the sample:

$$C(x,y) = -\frac{1}{\rho_{xx}}\left(\frac{\partial\rho_{xx}}{\partial x} - \frac{\partial\rho_{xy}}{\partial y}\right) \tag{7.6}$$

$$D(x,y) = -\frac{1}{\rho_{xx}}\left(\frac{\partial\rho_{xx}}{\partial y} + \frac{\partial\rho_{xy}}{\partial x}\right) \tag{7.7}$$

Even for simple inhomogeneity cases, such as a gradient of the carrier density along the Hall bar, an exact analytical solution of Eq. (7.5) cannot be found. The only way to deal with inhomogeneities is to solve the problem numerically.

To reduce the amount of calculations, boundary conditions are chosen in their simplest possible form. Instead of the true Hall bar geometry, we consider a rectangle defined by four lines in the x-y plane: $x = \pm x_0$ and $y = \pm y_0$ (see Fig. 7.1). The potential contacts are considered to be infinitely small (*i.e.* point contacts) and located at $(\pm x_1, \pm y_0)$, while the current contacts cover the left and right edges of the sample completely.

The boundary conditions at the upper and lower edge of the sample are given by realizing that the current cannot cross the edge. Therefore, the y-component of the current density, j_y, vanishes at the boundary: $j_y = -\partial\phi/\partial x =$

0, requiring the potential $\phi(x,y)$ to be constant along the lines $y = -y_0$ and $y = +y_0$.

Since the current potential is only defined up to an additive constant, we are free to choose the zero level at the lower edge of the sample:

$$\phi(x,y) = 0, \quad y = -y_0. \tag{7.8}$$

In this case the value of ϕ at the upper edge is determined by the total current J across the sample:

$$J = \int_{-y_0}^{y_0} j_x dy = \int_{-y_0}^{y_0} \frac{\partial \phi}{\partial y} dy = \phi(x,y_0) - \phi(x,-y_0). \tag{7.9}$$

Without loss of generality we can take the total current J equal to unity. Then,

$$\phi(x,y) = 1, \quad y = +y_0. \tag{7.10}$$

The boundary conditions at the left and right side of the sample are more complicated. We will assume, that the current contacts are "ideal", *i.e.* with an infinitely small resistance at the interface and in the contact. At a finite current density the electric field in such a contact is zero. Since the component of the field parallel to the boundary is continuous, E_y vanishes at both sides of the sample:

$$E_y = 0, \quad x = \pm x_0. \tag{7.11}$$

Using the definition of the current potential and the material equation (7.3), it can be shown that:

$$E_y = -\rho_{xy} \frac{\partial \phi}{\partial y} - \rho_{xx} \frac{\partial \phi}{\partial x}. \tag{7.12}$$

Combining the last two equations, we arrive at the final form of the boundary condition at the interface between the current contacts and the sample:

$$\frac{\partial \phi}{\partial x} + \alpha(x,y) \frac{\partial \phi}{\partial y} = 0, \qquad x = \pm x_0, \tag{7.13}$$

where $\alpha(x,y) = \rho_{xy}/\rho_{xx}$ is the tangent of the Hall angle.

Eq. (7.5) together with the boundary conditions given by Eqs. (7.8),(7.10) and (7.13) complete the formulation of the initial problem.

7.3. Measurable quantities

The experimentally measured quantity is a 4-point resistance, not a current potential. To calculate the resistance from the solution of Eq. (7.5), a few additional steps are needed. First of all, we have to obtain the current distribution by taking spatial derivatives of $\phi(x, y)$:

$$j_x = \frac{\partial \phi}{\partial y}, \quad j_y = -\frac{\partial \phi}{\partial x}. \tag{7.14}$$

Then, using material equations, we obtain the distribution of the electric field:

$$E_x = \rho_{xx} j_x + \rho_{xy} j_y, \tag{7.15}$$

$$E_y = -\rho_{xy} j_x + \rho_{xx} j_y. \tag{7.16}$$

In the last step the electric field between two potential contacts has to be integrated in order to calculate the voltage. Since the total current is equal to unity, the voltage corresponds to the value of the 4-point resistance. For an ideal, homogeneous sample the longitudinal resistances measured at the top and bottom pair of contacts are identical. However, this is not the case for a sample with macroscopic inhomogeneities with a length scale comparable to the sample size. Therefore, we distinguish two longitudinal resistances measured at the top and the bottom edges of the sample (see Fig. 7.1):

$$R_{xx}^{top} = \int_{-x_1}^{x_1} E_x(x, y_0) dx, \quad R_{xx}^{bot} = \int_{-x_1}^{x_1} E_x(x, -y_0) dx, \tag{7.17}$$

as well as two Hall resistances measured at the left and right pairs of potential contacts :

$$R_{xy}^{left} = \int_{-y_0}^{y_0} E_y(-x_1, y) dy, \quad R_{xy}^{right} = \int_{-y_0}^{y_0} E_y(x_1, y) dy. \tag{7.18}$$

7.4. Density gradient and local resistivities

The simplest and, perhaps, most interesting example of a macroscopic inhomogeneity is a gradient of the carrier density. This type of inhomogeneity is easy to parametrize and to determine experimentally. In some special cases it can even be solved analytically. Carrier density gradients were found to be ubiquitous present in the samples discussed in this work. In this Section we discuss the spatial variation of the local resistivities, $\rho_{xx}(x, y)$ and $\rho_{xy}(x, y)$, caused

by a small carrier gradient in an arbitrary direction. We also derive expressions for the coefficients $C(x,y)$ and $D(x,y)$, which will be used in the numerical simulations in the following Section.

A gradient of a carrier density n_e in an arbitrary direction can be written as:

$$n_e(x,y) = n + G_x\frac{x}{2x_0} + G_y\frac{y}{2y_0} \tag{7.19}$$

where n is the averaged density and G_x and G_y are parameters, which are the measure of the strength of the gradient along the different axes. For instance, $G_x = 0.02$ means that the density increases by 2% from the left to the right edge of the sample.

A major assumption in this and the following sections is the dependence of the components of the local resistivity tensor on two parameters only: temperature T and the local value of the filling factor ν. Such an assumption is rather natural and it has been used in many other works that analyze transport properties of quantum Hall systems [61, 65, 99]. Explicit expressions Eqs. (3.13)-(3.15) for the components of the resistivity tensor as a function of the filling factor ν were derived by Oswald, Span and Kuchar [61] using the Landau level addition (substraction) transformation. Thus, we assume that inhomogeneities in ρ_{xx} and ρ_{xy} are caused merely by the spatial variation of ν, which, in turn, completely depends on the distribution of the carrier density n_e:

$$\nu(x,y) = \frac{h}{eB}n_e(x,y). \tag{7.20}$$

The experiments reported in Chapter 4 show, that density gradients of the order of 1-2% are rather normal, even for high quality samples. The important question rises to what extent such small gradients affect the distribution of local resistivities. To answer this question, consider the $\rho_{xx}(B)$ curves in Fig. 7.2, simulated by the Landau level addition procedure. Fig. 7.2 shows ρ_{xx} as a function of the magnetic field B for two values of the carrier density, with a 1.5% difference. The parameter ν_0 used for simulation of the curves was taken from the PI transition on sample HPW-#59 at $T = 0.14$ K (see Chapter 5).

The distance ΔB between the two peaks in Fig. 7.2 is determined by the difference in the carrier concentration Δn:

$$\frac{\Delta B}{B} = \frac{\Delta n}{n_e}, \tag{7.21}$$

while the width of the peaks is controlled by the temperature. At high T (not shown) the peaks are broad and the local resistivities vary only slightly across

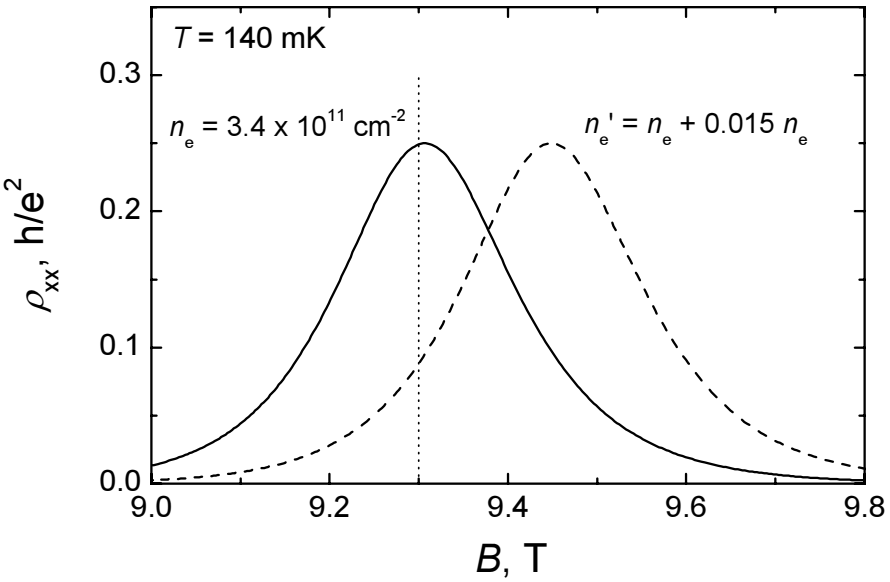

Figure 7.2: Simulated curves for the longitudinal resistivity as a function of the magnetic field for two close values of the carrier density at $2 \rightarrow 1$ PP transitions. At $B = 9.3$ T (dotted vertical line) the values of the longitudinal resistivities differ almost a factor 3. Such a large difference is the result of only 1.5% variation in the carrier density.

the sample. However, at low enough temperatures, the width becomes comparable to the distance between the peaks, as illustrated in Fig. 7.2. In this case, the values of the local resistivity in different parts of the sample can vary significantly. For example, at $B = 9.3$ T (where the left curve has a maximum) the ratio of local resistivities is about 3. Therefore at low temperatures even small inhomogeneities in the carrier concentration can cause huge spatial variations of the resistivity.

For a known distribution of n_e given by Eq. (7.19) we can obtain all partial derivatives needed for calculating $C(x,y)$ and $D(x,y)$ according to Eqs. (7.6)-(7.7). For example,

$$\frac{\partial \rho_{xx}}{\partial x} = \frac{\partial \rho_{xx}}{\partial \nu}\frac{\partial \nu}{\partial x} = \frac{G_x}{2x_0}\frac{h}{eB}\frac{\partial \rho_{xx}}{\partial \nu}, \tag{7.22}$$

and similar equations can be derived for $\frac{\partial \rho_{xx}}{\partial y}$, $\frac{\partial \rho_{xy}}{\partial x}$ and $\frac{\partial \rho_{xy}}{\partial y}$.

The last piece of information we need to determine for the coefficients $C(x,y)$ and $D(x,y)$ are explicit expressions for ρ_{xx}, $\partial\rho_{xx}/\partial\nu$ and $\partial\rho_{xy}/\partial\nu$ as function of the filling factor ν. For this we refer again to Eqs. (3.13)-(3.15) and calculate the derivatives as follows:

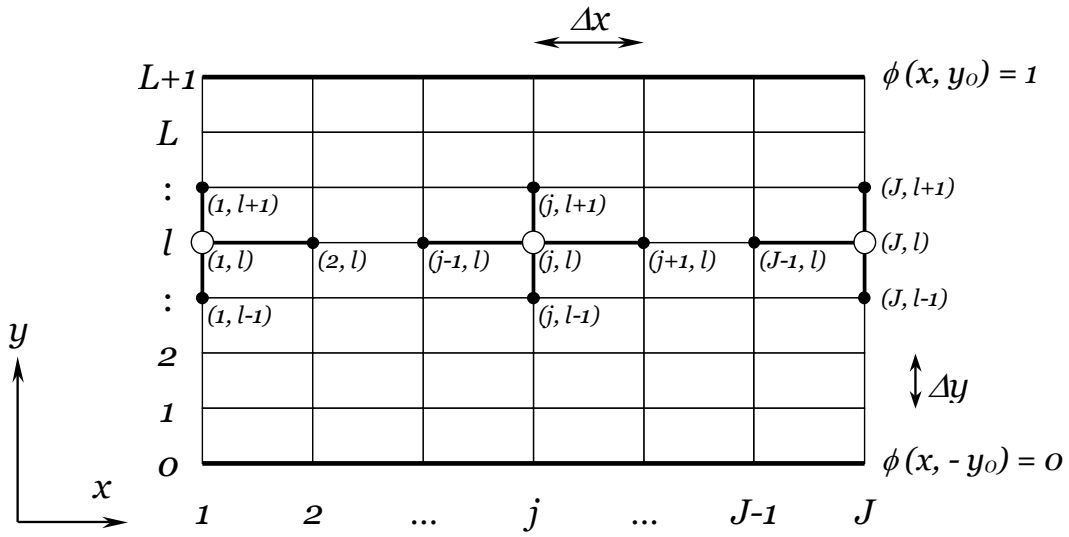

Figure 7.3: Grid, which illustrates the application of the finite difference method to solve Eq. (7.5).

$$\frac{\partial \rho_{xx}}{\partial \nu} = \frac{e^{\frac{1+2\nu+2\bar{\nu}}{2\nu_0(T)}} \left(\bar{\nu}^2 e^{\frac{1+2\bar{\nu}}{\nu_0(T)}} - (1+\bar{\nu})^2 e^{\frac{2\nu}{\nu_0(T)}} \right)}{\nu_0(T) \left(\bar{\nu}^2 e^{\frac{1+2\bar{\nu}}{\nu_0(T)}} + (1+\bar{\nu})^2 e^{\frac{2\nu}{\nu_0(T)}} \right)} \tag{7.23}$$

$$\frac{\partial \rho_{xy}}{\partial \nu} = \frac{-2\bar{\nu}\,(1+\bar{\nu})\, e^{\frac{1+2\nu+2\bar{\nu}}{\nu_0(T)}}}{\nu_0(T) \left(\bar{\nu}^2\, e^{\frac{1+2\bar{\nu}}{\nu_0(T)}} + (1+\bar{\nu})^2\, e^{\frac{2\nu}{\nu_0(T)}} \right)^2} \tag{7.24}$$

7.5. Calculation details

There is large number of textbooks dedicated to numerical solutions of partial differential equations (see *e.g.* Ref. [100]). The most straight forward way to solve nonlinear equations like the one in Eq. (7.5) is the finite-difference method (FDM).

Consider a discrete set of points within the rectangular area $-x_0 \leq x \leq x_0$, $-y_0 \leq y \leq y_0$ defined as (see Fig. 7.3):

$$x_j = -x_0 + (j-1)\Delta x, \qquad j = 1, 2, ..., J \tag{7.25}$$

$$y_l = -y_0 + l\Delta y, \qquad l = 0, 1, ..., L+1 \tag{7.26}$$

where Δx and Δy are the grid spacings:

$$\Delta x = \frac{2x_0}{J-1}, \Delta y = \frac{2y_0}{L+1} \tag{7.27}$$

Different ways of indexing in Eq. (7.25) and Eq. (7.26) were chosen for sake of compactness in dealing with the problem at a later stage.

From now on, we write $\phi_{j,l}$ for $\phi(x_j, y_l)$ and $\alpha_{j,l}$ for the tangent of the Hall angle $\alpha(x_j, y_l)$. According to the boundary conditions (7.8) and (7.10), the values of the current potential at the top and bottom edges of the sample are fixed:

$$\phi_{j,0} = 0, \quad \phi_{j,L+1} = 1, \qquad j = 1, 2, ..., J. \tag{7.28}$$

Therefore, on the whole grid we have $J \times L$ points with unknown values $\phi_{j,l}$.

Following the main ideas of FDM we substitute the derivatives and the Laplace operator at each point (x_j, y_l) with finite differences (see Fig. 7.3):

$$\frac{\partial \phi}{\partial x} = \frac{\phi_{j+1,l} - \phi_{j,l}}{\Delta x}, \tag{7.29}$$

$$\frac{\partial \phi}{\partial y} = \frac{\phi_{j,l+1} - \phi_{j,l}}{\Delta y}, \tag{7.30}$$

$$\Delta \phi = \frac{\phi_{j+1,l} - 2\phi_{j,l} + \phi_{j-1,l}}{(\Delta x)^2} + \frac{\phi_{j,l+1} - 2\phi_{j,l} + \phi_{j,l-1}}{(\Delta y)^2}. \tag{7.31}$$

The substitution (7.29) can not be applied at the right edge of the sample because in this case the index j runs out of range. Therefore, at $j = J$ we should use:

$$\frac{\partial \phi}{\partial x} = \frac{\phi_{j,l} - \phi_{j-1,l}}{\Delta x}. \tag{7.32}$$

Eqs. (7.29)-(7.32) transform the initial problem into a system of $J \times L$ linear equations with $J \times L$ unknowns $\phi_{j,l}$. The first $(J-2) \times L$ linear equations originate from Eq. (7.5). For $1 < j < J$, $1 \leq l \leq L$ we can write:

$$\begin{aligned} b^2\phi_{j,l-1} + \phi_{j-1,l} - (2 + 2b + C_{j,l} + D_{j,l})\phi_{j,l} + \\ (1 + C_{j,l})\phi_{j+1,l} + (b^2 + D_{j,l})\phi_{j,l+1} = 0, \end{aligned} \tag{7.33}$$

where $b = \Delta x / \Delta y$, $C_{j,l} = C(x_j, y_l)\Delta x$ and $D_{j,l} = bD(x_j, y_l)\Delta x$.

The remaining $2L$ equations can be obtained from the boundary conditions Eq. (7.13). Following the logic of previous substitutions, we write:

$$\phi_{2,l} - \phi_{1,l} + b\alpha_{1,l}(\phi_{1,l+1} - \phi_{1,l}) = 0 \tag{7.34}$$

$$\phi_{J,l} - \phi_{J-1,l} + b\alpha_{J,l}(\phi_{J,l+1} - \phi_{J,l}) = 0 \tag{7.35}$$

for all $1 \leq l \leq L$. Although the last two equations are absolutely correct, the solution was found to be unstable in the areas near the current contacts when the Hall angle approaches a value $\pi/2$ and as α diverges. Fortunately, for long enough Hall bars these instabilities do not affect the solution in the central part. This is quite understandable, because the measured resistance should not depend on details of the current contacts. Nevertheless, to obtain a smooth solution everywhere in the sample including the contact areas we replace Eqs. (7.34) and (7.35) by slightly different equations. These also originate from the boundary conditions Eq. (7.13), but extra requirements on smoothness are imposed:

$$2(\phi_{2,l} - \phi_{1,l}) + b\alpha_{1,l}(\phi_{1,l+1} - \phi_{1,l-1}) + \varepsilon(\phi_{1,l+1} - 2\phi_{1,l} + \phi_{1,l-1}) = 0 \quad (7.36)$$

$$2(\phi_{J,l} - \phi_{J-1,l}) + b\alpha_{J,l}(\phi_{J,l+1} - \phi_{J,l-1}) + \varepsilon(\phi_{J,l+1} - 2\phi_{J,l} + \phi_{J,l-1}) = 0 \quad (7.37)$$

where the parameter ε is used to suppress the instability near the current contacts. Note, that a large value of ε modifies the boundary conditions completely, therefore, Eqs. (7.34)-(7.35) should be used with care. If $\varepsilon > 1000$, the current potential changes almost linearly from 0 to 1 between the two ends of the current contact, rather than obeying condition (7.13). Most of the time we used $\varepsilon = 10$. With this value of ε the solution is pretty stable and at the same time it reproduces all characteristic features of the current distribution near the contact areas.

Since the number of equations is the same as the number of unknowns, we can now start numerically solving the system. In order to do so with Mathematica [62], we first switch from two running indexes to one. This is an important step. If indexing is properly done, Mathematica can solve a linear system in its matrix form, *i.e.* without taking care about indexing and using efficient internal algorithms. Renumbering is done according to the rule $\phi_{j,l} \rightarrow \phi_i$, where $i = j + J(l-1)$. In the same way we renumber $\alpha_{j,l}$, $C_{j,l}$ and $D_{j,l}$.

The final system of linear equations in matrix form looks very simple:

$$S\phi = h, \quad (7.38)$$

where S is a matrix of size $(J \times L)$ by $(J \times L)$, ϕ is a vector with $J \times L$ unknown elements ϕ_i, and h is a known vector of the same size as ϕ. The matrix S and the vector h are both sparse, i.e. most of their elements are zero. All non-zero elements are given in Table 7.1.

If not given otherwise, the ratio of the sample length to the width is 8 ($x_0 = 8$, $y_0 = 1$) in all numerical simulations. The mesh consists of 2000×80 points and its size is limited by the available computer memory. All plots

	$j=1$	$2 \le j \le J-1$	$j=J$
$S_{i,i-J}$	$-b\alpha_i+\varepsilon$	b^2	$b\alpha_i+\varepsilon$
$S_{i,i-1}$	0	1	2
$S_{i,i}$	$-2(1+\varepsilon)$	$-2-2b^2-C_i-D_i$	$-2(1+\varepsilon)$
$S_{i,i+1}$	2	$1+C_i$	0
$S_{i,i+J}$	$b\alpha_i+\varepsilon$	b^2+D_i	$-b\alpha_i+\varepsilon$
$h_i\ (l \neq L)$	0	0	0
$h_i\ (l=L)$	$-b\alpha_i-\varepsilon$	$-b^2-D_i$	$b\alpha_i-\varepsilon$

Table 7.1: All non-zero coefficients of sparse matrix S.

with distribution of the current potential, current density *etc*. were generated in Mathematica 5 (older versions of Mathematica do not support operations with sparse matrices).

The solution of the system gives values of the current potential $\phi_{j,l}$ on a grid. To calculate the four-probe resistance, which is the final purpose of our simulations, we have to: a) obtain a smooth function $\phi(x,y)$ from $\phi_{j,l}$ defined on the grid and b) calculate the four-point resistances as described in Section 7.3. Again all operations can be done using standard Mathematica functions, which include interpolation, differentiation and numerical integration.

7.6. Current and electric field distribution

The solution $\phi(x,y)$ of Eq. (7.5) for an homogeneous sample at filling factor $\nu = 1.5$ is shown in Fig. 7.4. The semi-integer (critical) value of the filling factor implies that both components of the resistivity tensor are temperature independent, and therefore, the calculated distribution of the current potential is valid at any T. One can easily see that the function $\phi(x,y)$ shown in Fig. 7.4 satisfies the boundary conditions (7.8) and (7.10): indeed, at the edges parallel to the x-axis the current potential is equal 0 (at $y=-1$) and 1 (at $y=1$).

In principle, the plot $\phi(x,y)$ contains all the information about the current and electric field distribution. However, in the way it is presented in Fig. 7.4 the functions $\phi(x,y)$ look very similar for the homogeneous and inhomogeneous cases. In order to see the differences, which affect the transport properties it is better to compare the distributions of the current density or electric field, extracted from $\phi(x,y)$ using Eqs. (7.14)-(7.16). The four contour plots on the left side of Fig. 7.5 represent the homogeneous case, with the distribution of

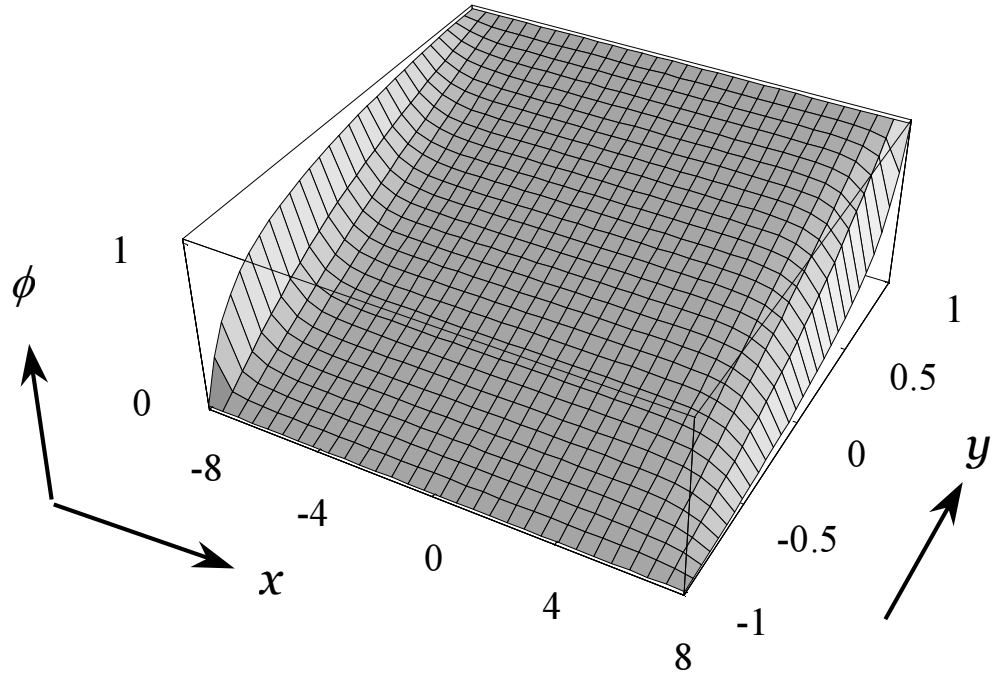

Figure 7.4: Current potential $\phi(x, y)$ for a homogeneous sample at filling factor $\nu = 1.5$.

j_x, j_y, E_x and E_y indicated by the corresponding labels. The darker areas represent higher fields or current densities. The white central area on the $j_y(x, y)$ plot (second from top in the left column) means that the y-component is zero and that the current flows along the long side of the sample. The fewer "lines of constant value" (contour lines) on a plot, the more homogeneous is the distribution of the corresponding component of the current or electric field in the sample. The distortions near the current contacts, which can be seen on all plots, are caused by the boundary conditions: the vector $\vec{E}$ has to be perpendicular to the contact and at the same time it has to form a Hall angle with respect to the vector $\vec{j}$. At the critical filling factor the tangent of the Hall angle is rather small and temperature independent. For example, at $\nu = 1.5$ the tangent of the Hall angle $\alpha = \rho_{xy}/\rho_{xx} = 3$. It becomes larger away from $\nu = 1.5$ and diverges when $T \to 0$. When this happens, the distortions near the current contacts transform into singularities in the current distribution at the right-top and left-bottom corners of the sample (for magnetic fields pointing up).

Our simulations for the homogeneous case show that the 4-point longitudinal resistance is just the product of the resistivity and the geometrical factor x_1/y_0 (see Fig. 7.1). This statement is true as long as the potential and current contacts are far from each other and distortions near the current contacts do not

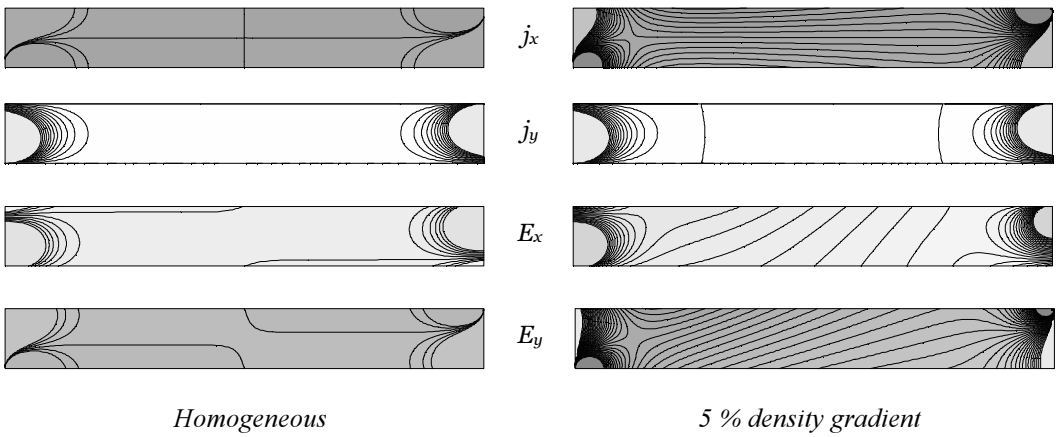

Figure 7.5: Distribution of both components of the current density and the electric field for a homogeneous sample (left column) and for a sample with 5% density difference between left and right edges (right column). The distributions correspond to the (averaged) filling factor $\nu = 1.5$.

affect the homogeneous current flow in the region between the potential contacts. We have calculated that the correction to the 4-point resistance caused by the boundaries are smaller than 0.1%, if the distance between the current and potential contacts is three times larger than the width of the sample. This is the reason why we use in our simulations $x_1 = 2$ most of the time (the other dimension being $x_0 = 8$ and $y_0 = 1$).

Very different current density and electric field distributions were found for an inhomogeneous sample. In the example shown on the right side of Fig. 7.5, the density increases linearly along the x-axis by 5 %. Because of this gradient, the filling factor reaches its critical value $\nu = 1.5$ only at the center of the sample and, in contrast to the homogeneous case, the distribution of local resistivities becomes temperature dependent now. For generating the contour plots on the right side of Fig. 7.5 we choose $\nu_0(T) = 0.037$, which is a realistic value and according to the inset in Fig. 5.4 roughly corresponds to $T \approx 0.8$ K. A striking feature which can be immediately seen in the upper contour plot, is the large number of lines of constant value running almost parallel to the long side of the sample. This means that the x-component of the current, j_x, has a gradient in the y-direction, *i.e.* perpendicular to the carrier density gradient. This somewhat unexpected result was recently derived analytically as well [53, 71, 101]. The distribution of the electric field is also quite different from the homogeneous case shown in the left. There is a large number of lines and moreover the contour plots $E_x(x, y)$ and $E_y(x, y)$ do not have a center of symmetry. This

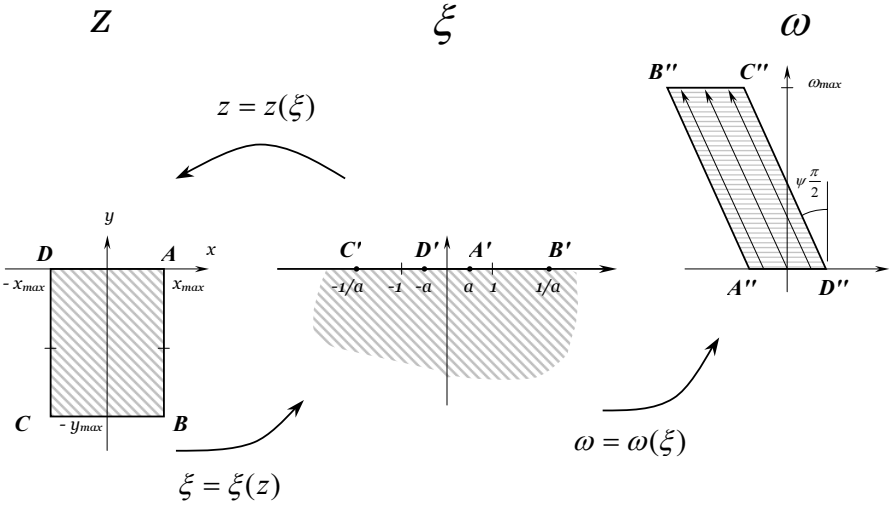

Figure 7.6: Two step conformal mapping of a rectangular sample (on the left side) on the area with a trivial solution of the Laplace equation (on the right).

results in values of the 4-point resistance measured at the top and bottom pairs of contacts, R_{xx}^{top} and R_{xx}^{bot}, which are different.

7.7. Test of the solution

Testing of the solution on a trivial or well-known case is an important step in the simulations. The most obvious (although not the easiest) way to test our method is to compare the results of simulations for a homogenous sample with the semi-analytical solution, which was obtained in the middle of the last century and is known as the gyrator problem [67, 68, 69]. In these papers, the authors employed the at that time popular method of conformal mapping, which was also successfully used by Van der Pauw in developing his famous technique of measuring resistivity on a slab of arbitrary shape [70]. The method is based on a theorem for harmonic functions *i.e.* functions which are solutions of the Laplace equation and have continuous second partial derivatives, which says that the harmonic function stays harmonic under conformal mapping [102]. The idea of the method is the following. By two subsequent mappings one transforms the initial rectangular sample into a parallelogram where the Laplace equation has a trivial solution due to the special relation between the Hall angle and the angles of the parallelogram. Since the functions that describe the mapping are known, one can establish a one-to-one correspondence between each point of the parallelogram and the rectangle and hence calcu-

late the distribution of the electric potential in the initial rectangular sample. These transformations involve special functions, particularly elliptic integrals and Jacobi elliptic functions. The mappings are illustrated in Fig. 7.6. Note, that the sketch shown is somewhat different from the ones in the original papers. Some changes were made for consistency with Mathematica: in the shaded areas (including borders) the special functions are continuous, according to their definitions in Mathematica, while for the sketches in the original papers this is not the case.

Since many special functions and their arguments are often represented using different (and because of that confusing) notations, below we give the so-called standard Mathematica form [62] for the functions used in our calculations for conformal mapping[1]:

$$z(\xi) = a\,\mathtt{EllipticF}[\mathtt{ArcSin}[\frac{\xi}{a}], a^4] \tag{7.39}$$

$$\xi(z) = a\,\mathtt{Sin}[\mathtt{JacobiAmplitude}[\frac{z}{a}], a^4] \tag{7.40}$$

$$\omega(\xi) = -\int_0^{\xi} \frac{dt}{(t-a)^{\frac{1+\psi}{2}}(t+1/a)^{\frac{1+\psi}{2}}(t+a)^{\frac{1-\psi}{2}}(t-1/a)^{\frac{1-\psi}{2}}} \tag{7.41}$$

where $\psi = \frac{2}{\pi}\arctan(\frac{\rho_{xy}}{\rho_{xx}})$ and the parameter a is the solution of the equation:

$$\frac{y_0}{x_0} = \frac{\mathtt{EllipticK}[1-a^4]}{2\mathtt{EllipticK}[a^4]}. \tag{7.42}$$

Unfortunately, the last equation can only be solved numerically, which is the reason to call this method semi-analytical. A good point, however, is that the parameter a depends only on the ratio y_0/x_0 and does not depend on the magnetic field or temperature. So it is enough to calculate it once. A fast algorithm for searching a root of Eq. (7.42) can be found in Ref. [103] (see Example 6 on page 602, where $m = a^4$). The other parameters presented in Fig. 7.6 can be obtained using the following equations:

$$x_{max} = \mathtt{Re}[z(1)],\;\; y_{max} = 2\mathtt{Im}[z(1)],\;\; \omega_{max} = \mathtt{Im}[\omega(\frac{2}{a})] \tag{7.43}$$

where `Re` and `Im` stand for the real and imaginary part, respectively.

The calculations with Mathematica work well for short samples, *i.e.* with a length that does not exceed six times the width. An example of a potential distribution in a homogeneous sample at $\nu = 2.5$ is shown in Fig. 7.7a. Once

[1] For the same formula in the traditional notation see the original papers Ref. [67, 68, 69].

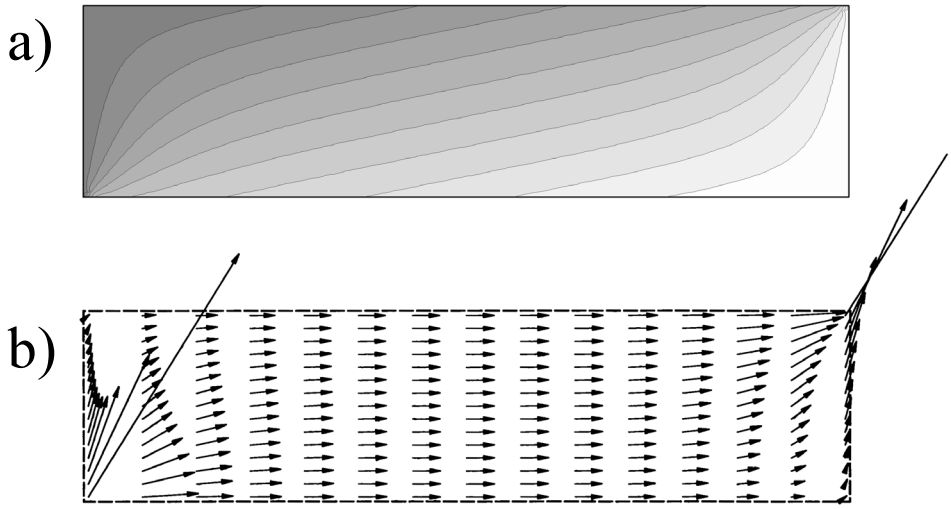

Figure 7.7: Distribution of the electrostatic potential (a) and current (b) in a homogeneous sample at $\nu = 2.5$ obtained by conformal mapping.

the electrostatic potential is known one can also calculate the distribution of the electric field and current density and compare these with results of numerical simulations. The vector plot in Fig. 7.7b represents the current flow. As expected for a homogeneous sample, the distribution is uniform in the middle of the sample with some distortions near the contacts. The mapping method and our simulations give the same results within almost machine accuracy if the Hall angle is small enough ($\alpha < 10$). A small value of α is required in order to use proper boundary conditions *i.e.* $\varepsilon = 0$. But even with $\varepsilon = 10$ and for any α of practical interest the difference between two results does not exceed 0.5% within 90% of the sample. The largest difference appears near the current contacts, but it does not affect the 4-probe resistance, for which only a distribution in the central part of the sample is relevant.

When comparing the simulations with the exact analytical solution, the PI transition represent a very special case. Due to the exponential dependence of the longitudinal resistivity on the filling factor the PI transition allows for an analytical solution in a presence of a gradient in the carrier density (*i.e.* for the inhomogeneous sample). In Section 7.9 such a comparison is made in detail. Here we only mention that the comparison shows perfect agreement between the numerical and analytical results.

Besides the tests described in the previous paragraphs, there are other possibilities to verify the results of our simulations. For example, substitution of the function $\phi(x, y)$ into Eq. (7.5) has to result in cancellation of the right

and left side of the equation. In this way one can test the solution for both homogeneous and inhomogeneous samples.

However, the simplest test is to verify that:

$$R_{xx}^{top} - R_{xx}^{bot} = R_{xy}^{right} - R_{xy}^{left}. \tag{7.44}$$

This simple relation, which is a direct result of Kirchhoff law, is not obviously contained in the solution. In fact, any error in simulations immediately violate this equation[2].

Finally, at the critical filling factor, as shown in the previous Section in Fig. 7.5, a gradient of the carrier density in the x-direction results in a gradient of j_x in the y-direction. This result, however, was already derived analytically in Section 4.2 (see Eq. (4.12)). Therefore, it can be considered as an additional qualitative test for the numerical method.

7.8. The effect of inhomogeneities on the PP transition

Distributions such as shown in Fig. 7.5 may serve to help understanding the effect of inhomogeneities on the transport properties of the 2-dimensional electron gas. In the following we discuss how the inhomogeneities affect the critical behavior. For this we have to simulate the 4-point resistances for different values of the filling factor ν at several temperatures. By analyzing the width of the peaks in $R_{xx}^{top}(\nu)$ and $R_{xx}^{bot}(\nu)$, as well as the slope of $R_{xy}^{left}(\nu)$ and $R_{xy}^{right}(\nu)$, we can determine how much the temperature dependence of the 4-point resistances differs from that of the local resistivities ρ_{xx} and ρ_{xy}. An alternative and, in fact, easier analysis can be done by fitting the simulated longitudinal and Hall resistances with Eqs. (3.14), (3.15) and (4.21) in order to extract the temperature dependence of the apparent parameter ν_0.

In this Section we concentrate on the $2 \rightarrow 1$ PP transition. To obtain a smooth dependence as a function of the filling factor, we calculate the 4-point resistances at 50 values of ν at each temperature. We assume in our model that the local resistivities $\rho_{xx}(\nu)$ and $\rho_{xy}(\nu)$ obey the behavior given by Eqs. (3.13)-(3.15) with the parameter ν_0 following the power-law temperature dependence:

$$\nu_0(T) = \left(\frac{T}{T_0}\right)^{\kappa}, \tag{7.45}$$

[2]Strictly speaking this equation is always violated due to rounding off errors, which occur during simulations, but the errors in the fourth or fifth digit are not considered as such.

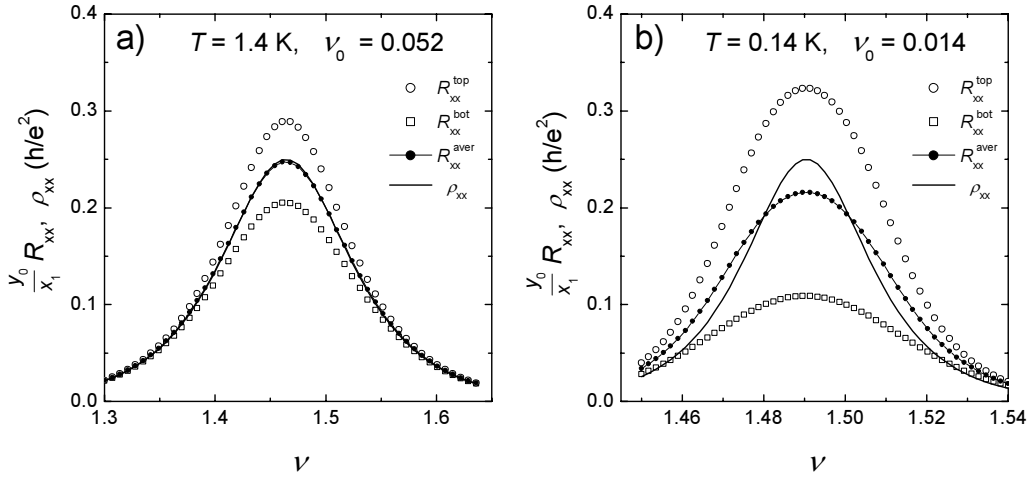

Figure 7.8: Simulated longitudinal 4-point resistance normalized by the geometrical factor x_1/y_0 at: a) high ($T = 1.4$ K) and b) low ($T = 0.14$ K) temperature. The sample has a carrier density gradient along the x-axis. The difference in electron density between the two pair of Hall contacts is 2.5%.

with a critical exponent $\kappa = 0.58$ and the parameter $T_0 = 230$ K, obtained from the experiment on the PI transition in the InGaAs/InP heterostructure (Chapter 5).

Let us first consider a carrier gradient along the Hall bar. In Fig. 7.8, we present results of a simulation for a sample with a 10 % carrier density difference between the two opposite current contacts, or with the definitions from Section 7.4: $G_x = 0.1$ and $G_y = 0$. For a comparison with the experimental data, however, the total density difference is not important. The relevant parameter is the carrier density difference between the potential contacts at $x = -x_1$ and $x = x_1$. Since we choose $x_0 = 8$ and $x_1 = 2$ (see Fig. 7.1), the density difference between the two pairs of Hall contacts is 4 times smaller than along the whole Hall bar and amounts to 2.5%. In order to compare the results of our simulations with the analytical curve given by Eq. (3.13) for $\rho_{xx}(\nu)$, we present in Fig. 7.8 the 4-point resistances normalized by the geometrical factor x_1/y_0. The results of the simulations in Fig. 7.8 are shown for two different temperatures. In both cases, the resistances measured at the top and bottom pairs of contacts are different. This is caused by the higher current density at the top edge of the sample. An inhomogeneous distribution in j_x was obtained in Section 7.6 and demonstrated in the top right contour plot in Fig. 7.5. Such a distribution of the x-component of the current is not just a result of the simulations, it also follows from the analytical solution given in Eq. (4.12).

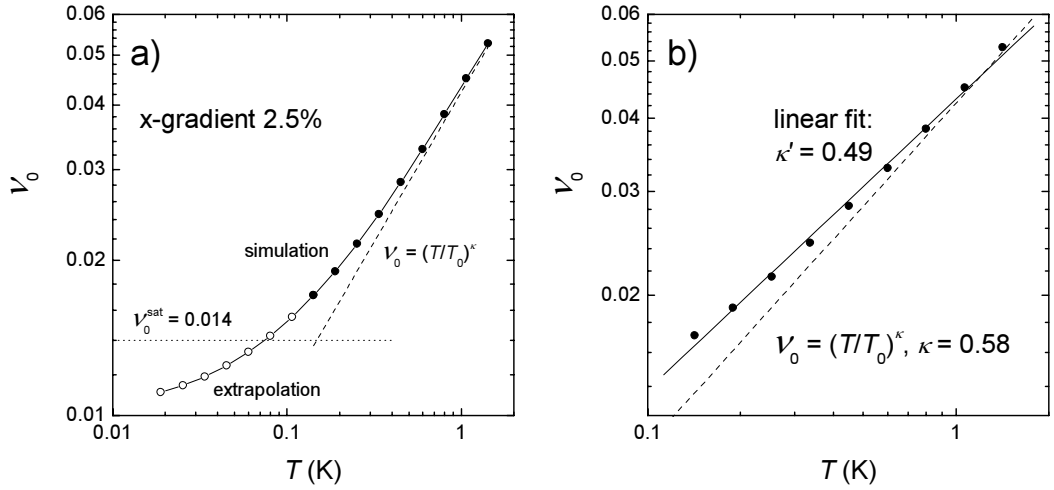

Figure 7.9: a) Temperature dependence of the parameter ν_0 for a homogeneous sample (dashed line) and for a sample with a 2.5% carrier density difference between the two pairs of Hall contacts after averaging (solid points). The open symbols represent an extrapolation to lower temperatures. The horizontal line shows an estimate for the saturation level calculated by Eq. (7.47); b) Same data on a smaller scale. The solid line represents a linear fit which results in a wrong value of the critical exponent.

The qualitative difference between the two plots becomes clear when we compare the averaged resistances $R_{xx}^{aver} = (R_{xx}^{top} + R_{xx}^{bot})/2$ with the theoretical resistivity. At $T = 1.4$ K (Fig. 7.8a), the averaged data are very close to the resistivity curve $\rho_{xx}(\nu)$ shown as the solid line. A completely different behavior was found at low temperatures. In Fig. 7.8b, we show the same set of curves, but simulated for $T = 0.14$ K. The peaks generated at low temperature are much sharper (note the different scale for the horizontal axes in the figures (a) and (b)). Also, the difference in peak heights becomes larger. However, the most important qualitative result is the strong departure of the averaged curve $\frac{y_0}{x_1} R_{xx}^{aver}(\nu)$ from the solid line $\rho_{xx}(\nu)$. The averaged peak is $\sim$15% lower and $\sim$25% wider, than expected for the ideal homogeneous sample.

Since at high temperature the curves $\frac{y_0}{x_1} R_{xx}^{aver}(\nu)$ and $\rho_{xx}(\nu)$ are almost identical, while at low T the deviation becomes more and more pronounced, we expect a different temperature behavior for the averaged and homogeneous sample results. Using the fit function Eq. (4.21), we have extracted the parameter ν_0 from the averaged data at a few temperatures in order to compare it with the true $\nu_0(T)$ behavior given by Eq. (7.45) for the homogeneous sample. The results are shown in Fig. 7.9. On the log-log plot the straight dashed line repre-

sents true power-law dependence. The solid symbols are values of ν_0 extracted from the averaged curves. They all lie above the dashed line. Also, strictly speaking, they do not obey power law behavior. This departure from scaling reminds strongly of the experimental data for the PP transitions reported in Chapter 5, first of all, by a clear tendency for saturation at low temperatures.

The value ν_0^{sat} at which the parameter ν_0 levels off can be roughly and independently estimated in the following way. If the minimum width $\delta\nu_{min}$ of the PP transition at very low T is limited only by the amount of inhomogeneities in the electron density δn, then according to Eq. (7.20):

$$\frac{\delta\nu_{min}}{\nu} = \frac{\delta n}{n}. \tag{7.46}$$

For a 2.5% density difference between the potential contacts $\delta n/n = 0.025$. At the $2 \rightarrow 1$ PP transition $\nu = 1.5$. In Chapter 3 we have shown that the transition width is related to the parameter ν_0 as $\delta\nu \approx 2.6\nu_0$, and therefore:

$$\nu_0^{sat} \approx \frac{\delta\nu_{min}}{2.6} = \frac{\delta n}{n} \times \frac{\nu}{2.6} \tag{7.47}$$

After substitution of numerical values we arrive at $\nu_0^{sat} \approx 0.014$, which is indicated by the horizontal dotted line in Fig. 7.9a. To check the accuracy of this estimate we have extrapolated the temperature dependence of $\nu_0(T)$ to lower values of T. Extrapolation was done with Mathematica and the results are shown by the open scattered symbols. For $T \rightarrow 0$ Mathematica gives the value $\nu_0(0) \approx 0.010$, which is reasonably close to $\nu_0^{sat} \approx 0.014$ obtained from our simple qualitative estimate in Eq. (7.47).

Although the solid points, as we already mentioned, do not fall on a straight line one can always make a linear fit to the data, considering deviations as "experimental errors". This results in an "apparent critical exponent" $\kappa' = 0.49$ (see Fig. 7.9b), which is significantly lower than the value 0.58 used in the simulations. The difference appears already in the first significant digit! This finding brings us to one of the most important results of this thesis: even rather small inhomogeneities in electron density hamper the observation of true critical behavior in measurements on the PP transition.

For a twice smaller carrier gradient, *i.e.* 1.25 %, the simulated exponent κ' obtained in the same temperature range 0.14-1.4 K amounts to 0.56. The systematic error decreased from 16 % in the previous example (2.5 % gradient) to less than 4 %, which shows that the error is not proportional to the density gradient. In fact not only the amount of inhomogeneities, but also the temperature

range, is important for the error in κ. Extending the low temperature limit to below 0.14 K leads to a larger error. This is because at lower T the value of ν_0 is closer to saturation. Therefore, the deviation from the power-law dependence is stronger.

According to Eq. (7.47), the systematic error for the PP transitions in the higher Landau levels should be larger than for the $2 \rightarrow 1$ transition, due to the larger value of the filling factor ν and, consequently, higher ν_0^{sat}. Such a Landau level dependent saturation at different ν_0^{sat} was experimentally observed in GaAs/AlGaAs heterostructures [75], although the authors did not offer an explanation for their finding.

We, however, do not simulate the effect of the gradient on higher PP transitions in this work. The reason for that is the following. Due to the large amount of disorder in the low-mobility structures the width of the Landau level seems often to be larger than the Zeeman splitting. In this case, different Landau levels significantly overlap and the PP transitions take place at filling factors which are quite different from the expected semi-integer values. An example of such a transition is shown in Fig. 4.7a. To avoid an additional complication of the model and a possible misinterpretation of the existing experimental results we concentrate on the $2 \rightarrow 1$ PP transition only.

Another important result of the simulations with a direct link to the experiment is the temperature dependence of the peak height. According to theory, the maximum of $\rho_{xx}(\nu)$ is temperature independent and, for example, for the $2 \rightarrow 1$ PP transition $\rho_{xx}^{max} = h/(4e^2)$. The experiments show, however, that the maximum of the longitudinal resistance has a pronounced T-dependence. Even after averaging over different contacts or opposite field polarities the peak height decreases with decreasing T. Results of simulations of the temperature dependence of the maximum value of the 4-point resistances are shown in Fig 7.10a. Although the top and bottom peaks have different types of temperature behavior, the averaged peak height decreases with decreasing T. Note, that the analytical result given by Eqs. (4.14)-(4.15) can not explain the temperature dependence of R_{xx}^{max} for the averaged curve. The analytical expressions in Chapter 4 were obtained using a linear approximation, which is not sufficient to reproduce all results of the numerical simulations.

The slope of the Hall resistance turns out to be rather insensitive to gradients in the x-direction. In Fig. 7.10b we present simulated Hall resistances for both pairs of contacts at $T = 0.14$ K. Fitting the curves $R_{xy}^{left}(\nu)$ and $R_{xy}^{right}(\nu)$ by the function Eq. (3.14), gives practically the same value of the parameter ν_0 as

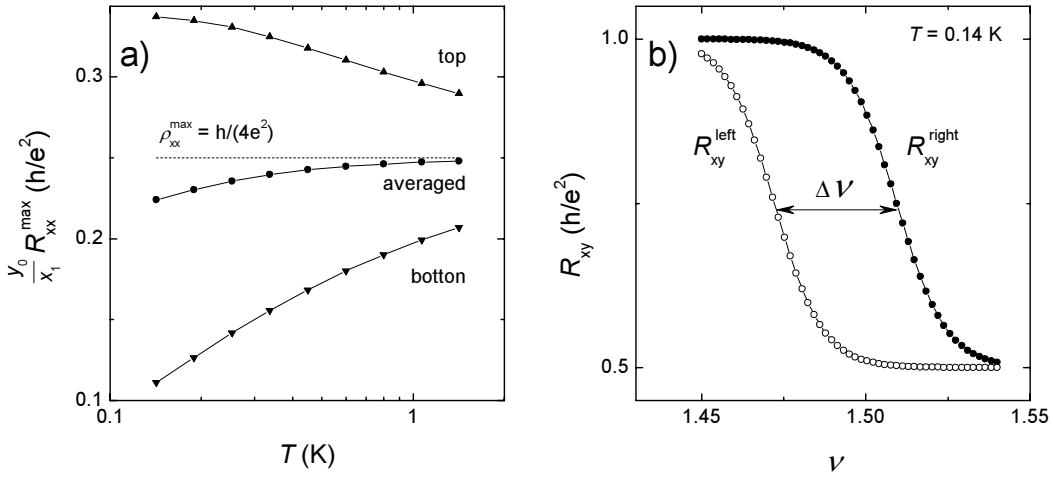

Figure 7.10: a) Temperature dependencies of the normalized peak height $\frac{y_0}{x_1} R_{xx}^{max}(T)$ for the $2 \rightarrow 1$ PP transition at 2.5% density difference. b) Hall resistances at the left and right pairs of contacts as a function of the filling factor simulated for the sample with a 2.5% carrier density difference between the two pairs of the Hall contacts. The shift $\Delta\nu$ between the curves directly related to the density gradient according to Eq. (7.48).

used in the simulations. Therefore, unlike for the longitudinal resistance, the Hall data provide a correct value of the critical exponent κ in case of a small density gradient along the Hall bar. Moreover, the shift $\Delta\nu$ between the two curves in Fig. 7.10b is proportional to the density difference Δn and can be used to determine the gradient:

$$\frac{\Delta n}{n} = \frac{\Delta \nu}{\nu}. \tag{7.48}$$

The reason, why the Hall resistance is less sensitive to the x-gradient is obvious: the Hall contacts probe a rather small area with one density, while the longitudinal resistance is measured over a longer distance with a significant change of the carrier concentration.

The results of simulations with a density gradient along the x-axis described so far are in line with the experimental results presented in Chapter 4. Indeed, simultaneous measurements of the Hall resistances from two pairs of contacts immediately reveal a density gradient, which is the key to understand the non-trivial symmetry in the longitudinal resistance upon field reversal. Less obvious is the effect of a density gradient in the y-direction. Using very general symmetry related considerations, one can say that an infinitely long sample with a gradient along the y-axis possesses translational symmetry in the

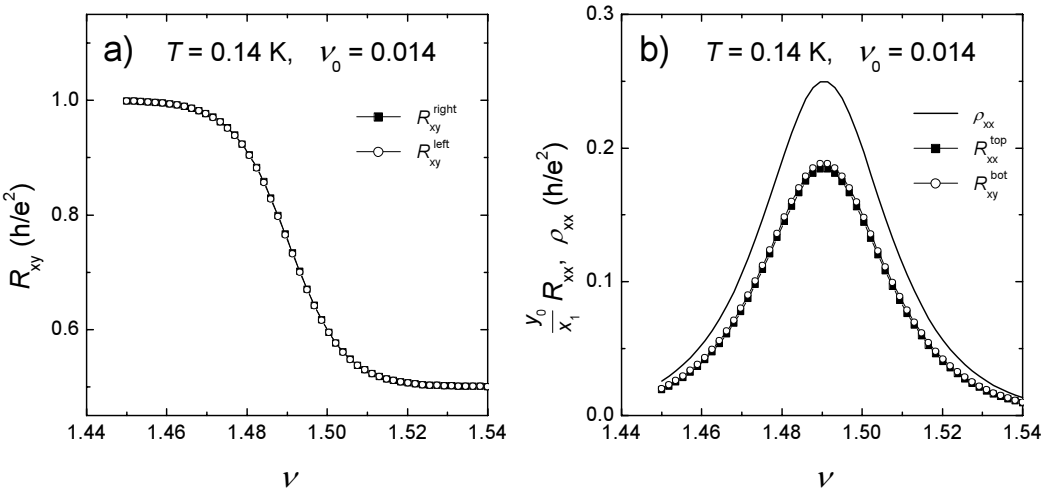

Figure 7.11: Hall (a) and longitudinal (b) resistance as a function of filling factor for a sample with 2.5% density difference in the y-direction. The main effect of the gradient perpendicular to a Hall bar is to decrease the peak height.

x-direction. Therefore, the Hall resistance should be the same everywhere in the sample: $R_{xy}^{right} = R_{xy}^{left}$. This also implies that the top and bottom longitudinal resistances must be equal according to Eq. (7.44). In principle, the equality of Hall resistances can be violated due to the finite sample size, but, since the current contacts are far away from the potential contacts such a violation is unlikely. The results of a simulation for a 2.5% density difference in the y-direction is shown in Fig. 7.11. As expected from the symmetry of the problem, both Hall, as well as both longitudinal resistances, measured at different pairs of contacts, are practically the same. The main effect of the perpendicular gradient is a decreasing peak height, which is 25% lower than for the homogeneous sample. The width of the peak is affected only slightly by the gradient (5% decrease), while the Hall curves seem to be identical to $\rho_{xy}(\nu)$ for the homogeneous case.

So far we considered only two particular cases of a density gradient, *i.e.* along the x- and y-axes. In both cases the temperature dependence of the Hall resistance gives a correct value of the critical exponent κ. Does this mean that Hall measurements are immune to inhomogeneities and always give a proper exponent? Simulations for gradients in arbitrary directions show that this is not the case. For example, for $G_x = 0.08$ and $G_y = 0.02$, the largest density difference between two potential contacts (between left bottom and right top contacts) is $\sim 2.8\%$. The values of the apparent critical exponents obtained from longitudinal and Hall resistances are $\kappa' = 0.53$ and $\kappa' = 0.55$, respectively. More-

over, due to the lower symmetry of the initial problem, the Hall resistance is not symmetric upon field reversal:

$$R_{xy}^{top}(-B) \neq -R_{xy}^{top}(B), \quad R_{xy}^{bot}(-B) \neq -R_{xy}^{bot}(B) \tag{7.49}$$

In other words, if the gradient direction does not coincide with one of the axes, inhomogeneities are responsible for an "effective contact misalignment", even if the Hall bar itself has an ideal geometry.

7.9. Numerical simulation and the PI transition

In Chapter 3 we have shown that the PI transition represents an exceptional case for which the 4-point resistance can be calculated analytically for arbitrary density gradients. This result was obtained for an infinitely long sample assuming that the Hall resistivity ρ_{xy} is quantized and the longitudinal resistivity ρ_{xx} obeys the exponential law:

$$\rho_{xy}(\nu) = 1, \tag{7.50}$$

$$\rho_{xx}(\nu) = \exp(-X), \quad X = -\frac{\nu - \nu_c}{\nu_0(T)}. \tag{7.51}$$

where ν_c is the critical value of the filling factor ν and both components of the resistivity tensor ρ_{xx} and ρ_{xy} are expressed in units of h/e^2. We derived that the 4-point Hall resistance R_{xy} stays quantized through the PI transition:

$$R_{xy}(\nu) = 1, \tag{7.52}$$

while the longitudinal resistance R_{xx} is:

$$R_{xx}(\nu) = \frac{L}{W}\,\rho_{xx}(\nu)N(\nu), \tag{7.53}$$

where W and L stand for the sample width and for the distance between the potential contacts, respectively. The additional factor $N(\nu)$ is:

$$N(\nu) = \frac{\sinh(g_x)}{g_x} \cdot \frac{g_y}{\sinh(g_y)}, \tag{7.54}$$

where the parameters g_x and g_y are proportional to the components of the density gradient along the different axes:

$$g_x = \frac{1}{2}\frac{\Delta n_x}{n} \cdot \frac{\nu}{\nu_0(T)}, \quad g_y = \frac{1}{2}\frac{\Delta n_y}{n} \cdot \frac{\nu}{\nu_0(T)}. \tag{7.55}$$

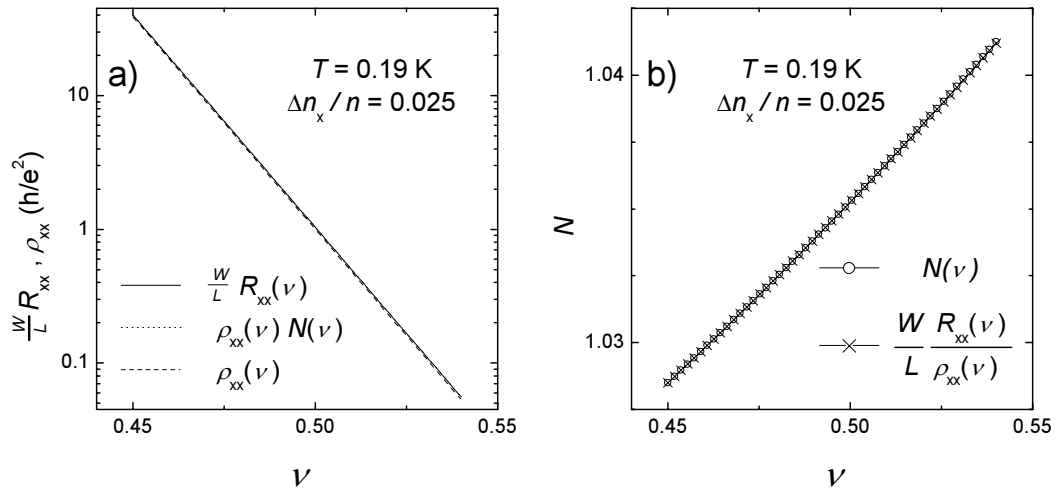

Figure 7.12: a) Comparison of the analytical solution for a homogeneous (dotted line) and an inhomogeneous (dashed line) sample, together with the results of simulations (solid line). The difference is hardly visible; b)Function $N(\nu)$ obtained in two different ways: according to Eq. (7.54) (open symbols) and from the numerical simulation (cross symbols). The density difference between the contacts is 2.5% along the x-axis. The two curves practically coincide.

In the last equations Δn_x is the density difference between the potential contacts along the sample, Δn_y is the density difference between the top and bottom edges of the sample, and n and ν are the averaged density and filling factor, respectively.

Since the analytical solution for the PI transition is already known, simulations can be used only to verify the obtained result, test the numerical method and study finite size effects. In order to compare the results of simulations with the analytical solution we plot on the same graph the normalized 4-point resistance $\frac{W}{L}R_{xx}(\nu)$ and the theoretical curves $\rho_{xx}(\nu)$ and $\rho_{xx}(\nu)N(\nu)$ (see Fig. 7.12a). However, for a gradient of a few percent the function $N(\nu)$ is close to unity even at the smallest value of $\nu_0(T)$, while $\rho_{xx}(\nu)$ changes by several orders of magnitude. Therefore, the difference between the curves shown in Fig. 7.12a is hardly visible on a logarithmic scale. From the one hand this is very good, because it implies that the critical exponent κ is not affected by a small gradient. On the other hand, from such a plot we can not conclude whether simulations give the same answer as the analytical formula. To verify the results of our simulations we compare in Fig. 7.12b the function $N(\nu)$ calculated with Eq. (7.54) and the normalized simulated resistance divided by the resistivity $\frac{W}{L}R_{xx}(\nu)/\rho_{xx}(\nu)$. According to Eq. (7.53) the two curves should be identical and, as one can see

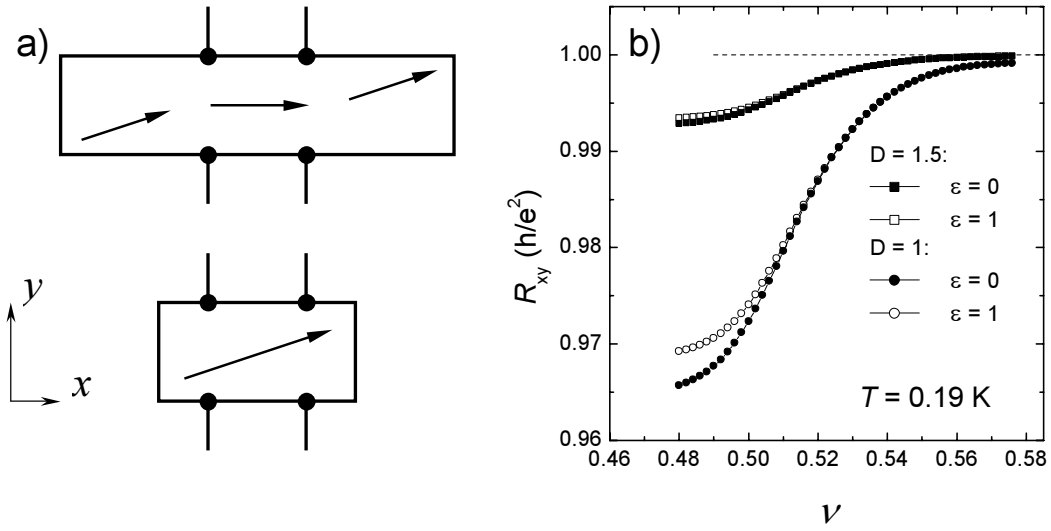

Figure 7.13: a) Top: schematic current flow in a long Hall bar, bottom: idem in a short Hall bar; b) Deviation of the Hall resistance from the quantized value h/e^2 (given by the dashed line) for two finite size samples. See text for meaning of the parameters D and ε.

from Fig. 7.12b this is indeed the case, indicating that simulations on a finite size sample agree with the analytical result for an infinitely long strip.

Another important finding obtained from simulations on finite size samples is the deviation of the Hall resistance from the quantized value $R_{xy} = h/e^2$ at the PI transition. This deviation becomes noticeable when the distance between the current and potential contacts is smaller than twice the sample width. Qualitatively the effect can be understood with help of Fig. 7.13a. In presence of a magnetic field the current enters and leaves the sample through opposite diagonal corners. If the sample is long enough (upper sketch), the current in the middle of the sample is homogeneous and parallel to the long edges. In this case, the electric field between the Hall contacts is entirely caused by the Hall effect: $E_y = \rho_{xy} j_x$. However, if the sample is short, then the current in the middle of the sample has a non-zero component along the y-axis (lower sketch), which contributes to E_y with negative sign: $E_y = \rho_{xy} j_x - \rho_{xx} j_y$. To make things more clear, we introduce a new parameter D:

$$D = \frac{x_0 - x_1}{2y_0} \tag{7.56}$$

which is the distance between the current and nearest potential contacts divided by the sample width. Fig. 7.13b shows the results of simulations for two values of D: $D = 1$ ($x_0 = 4$, $x_1 = 2$, $y_0 = 1$) and $D = 1.5$ ($x_0 = 5$, $x_1 = 2$, $y = 1$).

Since the boundaries play a crucial role in this effect, we have to use correct boundary conditions (7.34)-(7.35), which can be obtained from (7.36)-(7.37) at $\varepsilon = 0$. Stability of the solution, which was discussed in Section 7.5, is not a problem now, because deep in the insulating state the Hall angle is small. To make sure that the solution is stable on the metallic side as well, we show in the same plot simulations for $\varepsilon = 1$, which basically satisfy different boundary conditions. However, since both solutions are almost the same at $\nu > 0.51$ and the one for $\varepsilon = 1$ is definitely more stable, we conclude that stability is not an issue for $\varepsilon = 0$ through the PI transition as well.

The result obtained imposes restrictions on the sample design. It shows, that the sample should be reasonably long in order to properly study the PI transition and, particularly, corrections to scaling, which are all about measuring the deviations from the quantized value of R_{xy}.

Finite size simulations might (at least partially) explain the decrease of the Hall resistance observed in the PI experiments on sample HPW-#59 and shown in Fig 5.2. Although, the Hall bar is not perfectly defined (Fig. 5.1), the distance from the current contact to the nearest edge of the potential contacts is $\sim 1.5 \times W$ rendering a small decrease of R_{xy} in this case quite possible.

7.10. Conclusions

In summary, in this chapter we presented results of numerical simulations for one particular example of inhomogeneities in the 2DEG, namely, a gradient of the carrier density. Our interest was limited to gradients, because this case can be studied experimentally in transport measurements. Certainly, simple density gradients are not the only macroscopic inhomogeneity present in real samples. However, more complicated cases require a detailed knowledge of the density distribution, which can not be extracted from 4-point resistance measurements. Besides, significantly higher computational power is needed for such simulations. Nevertheless, we believe that our results for density gradients are a significant step forward in explaining the spread in values of critical exponents reported in the literature. Finally, our simulations reproduce a number of experimentally observed features not expected for homogeneous samples.

It has been shown that a gradient has qualitatively different effects on the PI and PP transitions. In case of the PI transition:

- simulations confirm the symmetries in the transport coefficients upon

field reversal or exchange of contacts $R_{xx}^{top}(B) = R_{xx}^{top}(-B) = R_{xx}^{bot}(B)$;

- for long enough samples the result of simulations coincide with the analytical solution given by Eqs. (7.52)-(7.53);
- in the experimentally accessible temperature range a gradient of a few percent does not affect the value of the critical exponent κ;
- if the distance between the current and potential contacts is smaller than twice the sample width, the Hall resistance R_{xy} deviates noticeably in the insulating phase from the quantized value h/e^2 towards smaller values.

In case of the PP transition:

- in general, longitudinal resistances measured from both sides of the Hall bar are different: $R_{xx}^{top}(B) \neq R_{xx}^{bot}(B)$;
- in the case of a gradient parallel to the Hall bar, the longitudinal resistances posses reflection symmetry $R_{xx}^{top}(\pm B) = R_{xx}^{bot}(\mp B)$; the Hall resistances from different pairs of contacts can be used to determine the value of the gradient according to Eq. (7.48);
- the gradient perpendicular to the long side of the Hall bar mainly affects the height of the R_{xx} peak, but not the width of the PP transition;
- a rather small density gradient is able to modify the temperature dependence of the transition width, masking true critical behavior of the quantum Hall system;
- the systematic error in the extracted value of the critical exponent κ depends on the temperature range and the density difference between the potential contacts, but in general the error is much larger for the PP than for the PI transition and the value of κ is underestimated;
- the higher Landau level index, the larger the systematic error in κ;
- simulations can qualitatively explain the temperature dependence of the maximum of the $R_{xx}(B)$ peak;
- a gradient, which is neither parallel nor perpendicular to a Hall bar, is responsible for an effective "contact misalignment": $R_{xy}(-B) \neq -R_{xy}(B)$.

REFERENCES

[1] K. VON KLITZING, G. DORDA, and M. PEPPER, *New Method for High-Accuracy Determination of the Fine-Structure Constant Based on Quantized Hall Resistance*, Phys. Rev. Lett. **45**, 494 (1980).

[2] B.N. TAYLOR, editor, *The International System of Units (SI)*, volume 330, NIST special publication, Gaithersburg (1991).

[3] M. BÜTTIKER, *Absence of backscattering in the quantum Hall effect in multi-probe conductors*, Phys. Rev. B **38**, 9375 (1988).

[4] R.B. LAUGHLIN, *Quantized Hall Conductivity in Two Dimensions*, Phys. Rev. B **23**, 5632 (1981).

[5] R. KUBO, J. Phys. Soc. Japan **12**, 570 (1957).

[6] H. AOKI and T. ANDO, Solid State Commun. **38**, 1079 (1981).

[7] S. DATTA, *Electronic Transport in Mesoscopic Systems*, Cambridge University Press, Cambridge (1995).

[8] M.A. PAALANEN, D.C. TSUI, and A.C. GOSSARD, *Quantized Hall Effect at Low Temperatures*, Phys. Rev. B **25**, 5566 (1982).

[9] H.E. STANLEY, *Scaling, universality, and renormalization: Three pillars of modern critical phenomena*, Rev. Mod. Phys. **71**, S358 (1999).

[10] A.M.M. PRUISKEN, *Universal Singularities in the Integral Quantum Hall Effect*, Phys. Rev. Lett. **61**, 1297 (1988).

[11] A.M.M. PRUISKEN, *Field Theory, Scaling and the Localization Problem*, in R.E. PRANGE and S.M. GIRVIN, editors, *The Quantum Hall Effect*, Springer-Verlag, Berlin (1987).

[12] A.M.M. PRUISKEN, Nucl. Phys. **B285**, 719 (1987).

[13] A.M.M. PRUISKEN, Nucl. Phys. **B290**, 61 (1987).

[14] H.P. WEI, D.C. TSUI, M.A. PAALANEN, and A.M.M. PRUISKEN, *Experiments on Delocalization and University in the Integral Quantum Hall Effect*, Phys. Rev. Lett. **61**, 1294 (1988).

[15] L.P. KADANOFF, in M. GREEN, editor, *Proc. Intern. School of Physics "Enrico Fermi"*, Academic Press, New York, Corso LI (1971).

[16] N. GOLDENFELD, *Lectures on the phase transitions and the renormalization group*, Addison-Wesley (1992).

[17] D.T.N. DE LANG, L. PONOMARENKO, A. DE VISSER, C. POSSANZINI, S.M. OLSTHOORN, and A.M.M. PRUISKEN, *Evidence for a quantum Hall insulator in an InGaAs/InP heterostructure*, Physica E **12**, 666 (2002).

[18] M.A. PAALANEN, D.C. TSUI, A.C. GOSSARD, and J.C.M. HWANG, *Disorder and the fractional quantum Hall effect*, Solid State Commun. **50**, 841 (1984).

[19] I. RUZIN and S. FENG, *Universal Relation between Longitudinal and Transverse Conductivities in Quantum Hall Effect*, Phys. Rev. Lett. **74**, 154 (1995).

[20] Y. HUO, R.E. HETZEL, and R.N. BHATT, *Universal conductance in the lowest Landau level*, Phys. Rev. Lett. **70**, 481 (1993).

[21] K. BAKKER, Master thesis, University of Amsterdam.

[22] F. POBELL, *Matters and Methods at Low Temperatures*, Springer-Verlag, Berlin (1992).

[23] G. K. WHITE, *Experimental Techniques in Low-Temperature Physics*, Oxford University Press, New-York, 3rd edition (1979).

[24] J.P. PEKOLA, K.P. HIRVI, J.P. KAUPPINEN, and M.A. PAALANEN, *Thermometry by Arrays of Tunnel Junctions*, Phys. Rev. Lett. **73**, 2903 (1994).

[25] J.P. PEKOLA, J.K. SUOKNUUTI, J.P. KAUPPINEN, M. WEISS, P. VAN DER LINDEN, and A.G.M. JANSEN, *Coulomb Blockade Thermometry in the milli-Kelvin Temperature Range in High Magnetic Fields*, J. Low Temp. Phys. **128**, 263 (2002).

[26] M. PRUDENZIATI, *Handbook of Sensors and Actuators*, Elsevier, Amsterdam (1994).

[27] H. DOI, Y. NARAHARA, Y. ODA, and H. NAGANO, in U. ECKERN,

A. SCHMID, W. WEBER, and H. WU, editors, *Proceedings of the 17th International Conference on Low Temperature Physics, LT-17*, 405, Elsevier Science (1984).

[28] J.W. PIERCE, D.W. KUTY, and J.R. LARRY, Solid State Technol. **25**, 85 (1982).

[29] I. BAT'KO, K. FLACHBART, M. SOMORA, and D. VANICKY, *Design of RuO_2-based thermometers for the millikelvin temperature range*, Cryogenics **35**, 105 (1995).

[30] J. ROMAN, V. PAVLIK, K. FLACHBART, C. J. ADKINS, and J. LEIB, J. Low Temp. Phys. **108**, 373 (1997).

[31] B.I. SHKLOVSKII and A.L. EFROS, *Electronic Properties of Doped Semiconductors*, Springer, Berlin (1984).

[32] M. AFFRONTE, M. CAMPANI, S. PICCININI, M. TAMBORIN, B. MORTEN, M. PRUDENZIATI, and O. LABORDE, *Low temperature electronic transport in RuO_2-based cermet resistors* , J. Low Temp. Phys. **109**, 461 (1997).

[33] Q. LI, C.H. WATSON, R.G. GOODRICH, D.G. HAASE, and H. LUKEFAHR, *Thick Film Chip Resistors for Use as Low Temperature Thermometers*, Cryogenics **26**, 467 (1986).

[34] B. NEPPERT and P. ESQUINAZI, *Temperature and Magnetic Field Dependence of Thick-Film Resistor Thermometers (Dale Type RC550)*, Cryogenics **36**, 231 (1996).

[35] R. W. WILLEKERS, F. MATHU, H.C. MEIJER, and H. POSTMA, *Thick-Film Thermometers with Predictable R-T Characteristics and Very Low Magnetoresistance Below 1-K*, Cryogenics **30**, 351 (1990).

[36] A. BRIGGS, *Characterization of Some Chip Resistors at Low Temperatures*, Cryogenics **31**, 932 (1991).

[37] M. WATANABE, M. MORISHITA, and Y. OOTUKA, *Magnetoresistance of RuO_2-based resistance thermometers below 0.3 K*, Cryogenics **41**, 143 (2001).

[38] M. AFFRONTE, M. CAMPANI, B. MORTEN, M. PRUDENZIATI, and O. LABORDE, *Magnetoresistance of RuO_2-based thick film resistors*, J. Low Temp. Phys. **112**, 355 (1998).

[39] E. PELED, D. SHAHAR, Y. CHEN, D.L. SIVCO, and A.Y. CHO, *Observation of a Quantized Hall Resistivity in the Presence of Mesoscopic Fluctuations*,

Phys. Rev. Lett. **90**, 246802 (2003).

[40] S.M. GIRVIN, editor, *The Quantum Hall Effect: Novel Excitations and Broken Symmetries*, Topological Aspects of Low Dimensional Systems, Springer-Verlag, Berlin, also available as cond-mat/9907002.

[41] J.T. CHALKER and P.D. CODDINGTON, *Percolation, quantum tunnelling and the integer Hall effect*, J. Phys. C **21**, 2665 (1988).

[42] B. HUCKENSTEIN and B. KRAMER, *One-parameter scaling in the lowest Landau band: Precise determination of the critical behavior of the localization length*, Phys. Rev. Lett. **64**, 1437 (1990).

[43] B. MIECK, *Nonuniversal Delocalization in a Strong Magnetic Field*, Europhys. Lett. **13**, 453 (1990).

[44] Y. HUO and R.N. BHATT, *Current carrying states in the lowest Landau level*, Phys. Rev. Lett. **68**, 1375 (1992).

[45] T. ANDO, *Edge and Bulk Landau States in Quantum Hall Regime*, J. Phys. Soc. Japan **61**, 415 (1992).

[46] D.-H. LEE, Z. WANG, and S. KIVELSON, *Quantum percolation and plateau transitions in the quantum Hall effect*, Phys. Rev. Lett. **70**, 4130 (1993).

[47] A.M.M. PRUISKEN and I.S. BURMISTROV, *The instanton vacuum of generalized CP^{N-1} models*, Annals of Physics **316**, 285 (2005).

[48] A.M.M. PRUISKEN and I.S. BURMISTROV, *Theta renormalization, electron-electron interactions and super universality in the quantum Hall regime*, cond-mat/0502488 .

[49] D.J. THOULESS, *Maximum Metallic Resistance in Thin Wires*, Phys. Rev. Lett. **39**, 1167 (1977).

[50] E. ABRAHAMS, P.W. ANDERSON, P.A. LEE, and T.V. RAMAKRISHNAN, *Quasiparticle lifetime in disordered two-dimensional metals*, Phys. Rev. B **24**, 6783 (1981).

[51] B.L. ALTSHULER, A.G. ARONOV, and D.E. KHMELNITSKY, *Effects of electronelectron collisions with small energy transfers on quantum localisation*, J. Phys. C **15**, 7367 (1982).

[52] A.M.M. PRUISKEN, D.T.N. DE LANG, L.A. PONOMARENKO, and A. DE VISSER, *Quantum criticality, particle-hole symmetry, and duality of the plateau-insulator transition in the quantum Hall regime*, cond-mat/0109043 .

[53] D.T.N. DE LANG, *Magneto-transport Studies on Critical Behavior in the Quantum Hall Regime*, PhD thesis, Universiteit van Amsterdam (2005).

[54] D.E. KHMEL'NITSKII, JETP Lett. **38**, 454 (1983).

[55] H.P. WEI, A.M. CHANG, D.C. TSUI, A.M.M. PRUISKEN, and M. RAZEGHI, Surf. Science **170**, 238 (1986).

[56] C.P. BURGESS, R. DIB, and B.P. DOLAN, *Derivation of the semicircle law from the law of corresponding states*, Phys. Rev. B **62**, 15359 (2000).

[57] S. KIVELSON, D.-H. LEE, and S.-C. ZHANG, *Global phase diagram in the quantum Hall effect*, Phys. Rev. B **46**, 2223 (1992).

[58] B.P. DOLAN, *Modular invariance, universality and crossover in the quantum Hall effect*, Nucl. Phys. **B554**, 487 (1999).

[59] S.C. ZHANG, *The Chern-Simons-Landau-Ginzburg Theory of the Fractional Quantum Hall Effect*, Int.J.Mod.Phys.B **6**, 25 (1992).

[60] M. HILKE, D. SHAHAR, S.H. SONG, D.C. TSUI, Y.H. XIE, and D. MONROE, *Experimental evidence for a two-dimensional quantizedHall insulator*, Nature **395**, 675 (1998).

[61] J. OSWALD, G. SPAN, and F. KUCHAR, *Universality in the Crossover Between Edge-Channel and Bulk Transport in the Quantum Hall Regime*, Phys. Rev. B **58**, 15401 (1998).

[62] S. WOLFRAM, *The Mathematica book*, Cambridge University Press, Cambridge (1999).

[63] A.M. CHANG and D.C. TSUI, *Experimental observation of a striking similarity between quantum hall transport coefficients*, Solid State Commun. **56**, 153 (1985).

[64] H.L. STORMER, K.W. BALDWIN, L.N. PFEIFFER, and K.W. WEST, *Strikingly linear magnetic field dependence of the magnetoresistivity in high quality two-dimensional electron systems*, Solid State Commun. **84**, 95 (1992).

[65] S.H. SIMON and B.I. HALPERIN, *Explanation for the Resistivity Law in Quantum Hall System*, Phys. Rev. B **73**, 3278 (1994).

[66] S.H. SIMON, *Inhomogeneous transport and derivative relations in the quantum Hall regime*, Physica B **258**, 23 (1998).

[67] R.F. WICK, *Solution of the Field Problem of the Germanium Gyrator*, J. Appl.

Phys. **25**, 741 (1954).

[68] H.J. VON LIPPMANN and F. KUHRT, *Der Geometrieenfluß auf den transversalen magnetischen Widerstandseffekt bei rechteckförmigen Halbleiterplatten*, Z. Naturforschg. **13a**, 462 (1958).

[69] H.J. VON LIPPMANN and F. KUHRT, *Der Geometrieenfluß auf den Hall-Effect bei rechteckigen Halbleiterplatten*, Z. Naturforschg. **13a**, 474 (1958).

[70] L.J. VAN DER PAUW, *A Method of Measuring Specific Resistivity and Hall Effect of Discs of Arbitrary Shape*, Philips Res. Repts. **13**, 1 (1958).

[71] B. KARMAKAR, M.R. GOKHALE, A.P. SHAH, B.M. ARORA, D.T.N. DE LANG, A. DE VISSER, L.A. PONOMARENKO, and A.M.M. PRUISKEN, *The effects of macroscopic inhomogeneities on the magnetotransport properties of the electron gas in two dimensions*, Physica E **24**, 187 (2004).

[72] S. KOCH, R.J. HAUG, K. VON KLITZING, and K. PLOOG, *Experiments on scaling in $Al_xGa_{1-x}As/GaAs$ heterostructures under quantum Hall conditions*, Phys. Rev. Lett. **43**, 68286831 (1991).

[73] R.B. DUNFORD, N. GRIFFIN, M. PEPPER, P.J. PHILLIPS, and T.E. WHALL, *Universality at a quantum Hall - Hall insulator transition in a $Si/Si_{0.87}Ge_{0.13}$ 2D hole system*, Physica E **6**, 297 (2000).

[74] J. WAKABAYASHI, A. FUKANO, S. KAWAJI, Y. KOIKE, and T. FUKASE, *Experiments on localization in Landau subbands with the Landau quantum number 0 and 1 of Si inversion layers* , Surf. Science **229**, 60 (1990).

[75] K.-H. YOO, H.C. KWON, and J.C. PARK, *Experiments on scaling and variable range hopping in the integral quantum Hall effect*, Solid State Commun. **92**, 821 (1994).

[76] R.J. HAUG, K. VON KLITZING, K. PLOOG, and P. STREDA, *Edge state transport in high magnetic fields in a two-dimensional electron gas*, Surf. Science **229**, 229 (1990).

[77] R.J. HAUG, *Edge-state transport and its experimental consequences in high magnetic fields*, Semicond. Sci. Technol. **8**, 131 (1993).

[78] K. VON KLITZING and G. EBERT, in G. BAUER, F. KUCHAR, and H. HEINRICH, editors, *Two-dimentional Systems, Heterostructures and Superlattices*, 243, Springer, Berlin (1984).

[79] F. HOHLS, U. ZEITLER, and R.J. HAUG, *Conductance fluctuations at the*

quantum Hall plateau transition, Phys. Rev. B **66**, 073304 (2002).

[80] P.T. COLERIDGE and P. ZAWADZKI, *On the thermal broadening of a quantum critical phase transition*, Solid State Commun. **112**, 241 (1999).

[81] M.E. RAIKH and T.V. SHAHBAZYAN, *High Landau levels in a smooth random potential for two-dimensional electrons*, Phys. Rev. B **47**, 1522 (1993).

[82] S.W. HWANG, H.P. WEI, L.W. ENGEL, and D.C. TSUI, *Scaling in spin-degenerate Landau levels in the integer quantum Hall effect*, Phys. Rev. B **48**, 11416 (1993).

[83] R.T.F. VAN SCHAIJK, A. DE VISSER, S.M. OLSTHOORN, H.P. WEI, and A.M.M. PRUISKEN, *Probing the Plateau-Insulator Quantum Phase Transition in the Quantum Hall Regime*, Phys. Rev. Lett. **84**, 1567 (2000).

[84] D. SHAHAR, D.C. TSUI, M. SHAYEGAN, E. SHIMSHONI, and S. L. SONDHI, *A Different View of the Quantum Hall Plateau-to-Plateau Transitions*, Phys. Rev. Lett. **79**, 479 (1997).

[85] H.P. WEI, S.W. HWANG, D.C. TSUI, and A.M.M. PRUISKEN, *New results on scaling in the integral quantum Hall effect*, Surf. Science **229**, 34 (1990).

[86] H.P. WEI, S.Y. LIN, D.C. TSUI, and A.M.M. PRUISKEN, *Effect of long-range potential fluctuations on scaling in the integer quantum Hall effect*, Phys. Rev. B **45**, 3926 (1992).

[87] H.P. WEI, L.W. ENGEL, and D.C. TSUI, *Current scaling in the integer quantum Hall effect*, Phys. Rev. B **50**, 14609 (1994).

[88] L.W. WONG, H.W. JIANG, N. TRIVEDI, and E. PALM, *Disorder-tuned transition between a quantum Hall liquid and Hall insulator*, Phys. Rev. B **51**, 18033 (1995).

[89] W. PAN, D. SHAHAR, D.C. TSUI, H.P. WEI, and M. RAZEGHI, *Quantum Hall liquid-to-insulator transition in $In_{1-x}Ga_xAs/InP$ heterostructures*, Phys. Rev. B **55**, 15431 (1997).

[90] P.T. COLERIDGE, *Universality in an integer quantum Hall transition*, Phys. Rev. B **60**, 4493 (1999).

[91] J. JAROSZYSKI, G. KARCZEWSKI, J. WROBELA, T. ANDREARCZYK, A. STRYCHARCZUK, T. WOJTOWICZ, G. GRABECKI, E. PAPIS, E. KAMISKA, A. PIOTROWSKA, and T. DIETLA, *Temperature and size scaling of the QHE resistance: the case of large spin splitting*, Physica E **6**, 790

(2000).

[92] C. POSSANZINI, L. PONOMARENKO, D. DE LANG, A. DE VISSER, S.M. OLSTHOORN, R. FLETCHER, Y. FENG, P.T. COLERIDGE, R.L. WILLIAMS, and J.C. MAAN, *Scaling behavior of metal-insulator transitions in a Si/SiGe two dimensional hole gas*, Physica E **12**, 600 (2002).

[93] R.B. DUNFORD, N. GRIFFIN, P.J. PHILLIPS, and T.E. WHALL, *Weak localisation and inter-quantum Hall effect transitions in a 2D Si/SiGe hole system*, Physica B **298**, 496 (2001).

[94] D. SHAHAR, M. HILKE, C.C. LI, D.C. TSUI, S.L. SONDHI, J.E. CUNNINGHAM, and M. RAZEGHI, *A new transport regime in the quantum Hall effect*, Solid State Commun. **107**, 19 (1998).

[95] N.Q. BALABAN, U. MEIRAV, and I. BAR-JOSEPH, *Absence of Scaling in the Integer Quantum Hall Effect*, Phys. Rev. Lett. **81**, 4967 (1998).

[96] E. SHIMSHONI and A. AUERBACH, *Quantized Hall insulator: Transverse and longitudinal transport*, Phys. Rev. B **55**, 9817 (1997).

[97] L.P. PRYADKO and A. AUERBACH, *Hall Resistivity and Dephasing in the Quantum Hall Insulator*, Phys. Rev. Lett. **82**, 1253 (1999).

[98] L.A. PONOMARENKO, D.T.N. DE LANG, A. DE VISSER, D. MAUDE, B.N. ZVONKOV, R.A. LUNIN, and A.M.M. PRUISKEN, *New insights into the plateauinsulator transition in the quantum Hall regime*, Physica E **22**, 236 (2004).

[99] N.R. COOPER, B.I. HALPERIN, C.K. HU, and I.M. RUZIN, *Statistical Properties of the Low-Temperature Conductance Peak Heights for Corbino Disks in the Quantum Hall Regime*, Phys. Rev. B **55**, 4551 (1997).

[100] W.H. PRESS, S.A. TEUKOLSKY, W.T. VETTERLING, and B.P. FLANNERY, *Numerical Recipes in C*, Cambridge University Press, Cambridge (1992).

[101] L.A. PONOMARENKO, D.T.N. DE LANG, A. DE VISSER, V.A. KULBACHINSKII, G.B. GALIEV, H. KUNZEL, and A.M.M. PRUISKEN, *The Effect of Carrier Density Gradients on Magnetotransport Data Measured in Hall Bar Geometry*, Solid State Commun. **130**, 705 (2004).

[102] E. KREYSZIG, *Advanced Engineering Mathematics*, Wiley, New York, 7 edition (1993).

[103] M. ABRAMOVITZ and I. STEGUN, editors, *Handbook of Mathematical Func-*

tions, Dover Publications Inc, New York (1972).

SUMMARY

This thesis is devoted to an experimental investigation of the critical behavior of integer quantum Hall transitions in two-dimensional electron systems at low temperatures. One of the main goals of this work is to experimentally verify the concept of universality of the quantum Hall transitions. We especially focus on how macroscopic sample inhomogeneities influence the magnetotransport data. Values of the critical exponents extracted from the experimental transport data are compared to those obtained by numerical calculations for samples with small carrier density gradients.

The critical behavior of the integer quantum Hall effect has been a subject of debate for more than 15 years now. Although the critical indices are predicted to be universal, experimental results reported in the literature often contradict the concept of universality. In the course of this work, we recognized that in our samples the only transition which gives proper access to the critical behavior is the plateau-insulator (PI) transition, which take place when the Fermi level crosses the lowest Landau level. Data taken at the transitions between adjacent plateaus most of the time are not suitable for studying critical behavior as they are strongly affected by inhomogeneities present in the samples.

Before presenting our principal results, we focus our attention on sample selection and on certain important features of the experimental setup (Chapter 2). Since most of our experiments are carried out in strong magnetic fields, the magnetic field dependence of the thermometers was investigated thoroughly, as to avoid systematic errors in the extracted values of the critical exponents. In Chapter 3 we present some selected theoretical aspects of quantum critical behavior in the quantum Hall regime.

The key experiment for understanding the role of inhomogeneities is the observation of reflection symmetry in the longitudinal resistance at the plateau-plateau (PP) transitions (Chapter 4). Such a symmetry is accounted for by a small gradient in the electron density, which can be considered as an inhomogeneity on a length scale larger than the sample size. In some samples, the density gradient can be controlled by simultaneous measurements of the Hall

resistance from two pairs of potential contacts, combined with pulse illumination at low temperatures. By decreasing the density gradient to a very small value, we are able to reveal another aspect of universality - the semicircle law. We show that for a homogeneous sample the components of the conductivity tensor obey the semicircle relation for all resolved PP transitions (thus not only for the PI transition as previously perceived).

Despite the significant progress made in understanding the effect of inhomogeneities in Chapter 4, our semiconductor structures were found to be not suitable for studying critical behavior of the PP transitions. Therefore, in Chapters 5 and 6, we focus on the PI transitions. For two different semiconductor structures we observe proper scaling behavior with very similar values of the critical exponents. The extracted critical exponent $\kappa \approx 0.58$ is significantly larger than the Fermi-liquid value $\kappa = 0.42$, which suggests that Coulomb interactions play an important role in the integer quantum Hall phase transitions. The sample studied in Chapter 5 is the same as in the pioneering work of Wei *et al.*, where the value $\kappa \approx 0.42$ was reported for the first time. With the PI data at hand, we can assert now that the "universal" value reported by Wei *et al.* is largely affected by inhomogeneities and does not represent the true critical exponent. In Chapter 6 we report experiments on a sample with a tunable electron density n_e. The critical exponent κ does practically not depend on the carrier concentration. The tiny increase of κ with increasing n_e is attributed to the overlap of Landau levels at lower electron densities. We also report in Chapter 6 a new way of presenting scaling behavior. This method has a number of advantages compared to the traditional method.

A substantial contribution to this thesis is the numerical simulation of the influence of sample inhomogeneities on the transport properties, described in Chapter 7. Assuming universality of κ for the local resistivity tensor and a constant carrier density gradient, we are able to calculate the 4-point resistances for different temperatures, filling factors and density gradients (directions and magnitude). The results of our simulations are in a good qualitative agreement with experiments. Inhomogeneities strongly affect the width of the PP transitions at low temperatures and result in an underestimated value of the critical exponent κ. Our simulations also reproduce and explain the hitherto not quite understood T-dependence of the maximum of the longitudinal resistance. At the same time, we confirm that the PI transition is robust and insensitive to small gradients in the carrier concentration.

SAMENVATTING

Dit proefschrift is gewijd aan een experimentele studie van het kritiek gedrag van faseovergangen in het heeltallige quantum Hall effect (QHE). Het quantum Hall effect treedt op in twee-dimensionale electronengassen (2DEGs) bij lage temperatuur onder invloed van een sterk magneetveld. Een van de belangrijkste doelen van dit onderzoek is de experimentele verificatie van het concept universaliteit van de faseovergangen in het QHE. In dit proefschrift wordt met name onderzocht in hoeverre macroscopische inhomogeniteiten in het preparaat de magnetotransport data benvloeden. De waarden van de kritieke exponenten verkregen uit magnetotransport data, worden vergeleken met waarden verkregen door numerieke berekeningen aan preparaten met een kleine gradint van de ladingsdragersdichtheid.

Het kritiek gedrag van het heeltallige QHE is al meer dan vijftien jaar een onderwerp van flinke discussie. Alhoewel voorspeld is dat de kritieke exponenten universeel zijn, zijn de experimentele resultaten vaak in tegenspraak hiermee. In dit proefschrift wordt aangetoond dat in onze preparaten de enige overgang die een juiste toegang geeft tot het quantum kritisch gedrag de plateau-isolator (PI) overgang is. De PI overgang treedt op wanneer het Fermi niveau het laagste Landau niveau kruist. De transportmetingen aan plateau-plateau (PP) overgangen zijn meestal niet geschikt voor het bestuderen van kritiek gedrag, aangezien de data sterk benvloed worden door inhomogeniteiten in het 2DEG.

Alvorens de experimentele resultaten gepresenteerd worden (Hoofdstukken 4-6) wordt in Hoofdstuk 2 aandacht geschonken aan de criteria om een goed preparaat te selecteren. Daarnaast komen in Hoofdstuk 2 diverse belangrijke aspecten van de experimentele opstellingen aan de orde. Omdat de meeste van onze experimenten uitgevoerd zijn in een sterk magneetveld, is de veldafhankelijkheid van de thermometer onderzocht om systematische fouten in de waarden van de gemeten kritieke exponenten te vermijden. In Hoofdstuk 3 presenteren we enkele relevante aspecten van de theorie van quantum kritisch gedrag in het QHE.

De sleutel tot het begrijpen van de rol van inhomogeniteiten in onze

2DEGs is de observatie, in magnetotransportdata gemeten aan diverse halfgeleiderstukturen, van reflectie symmetrie in de longitudinale weerstand bij de plateau-plateau overgangen (Hoofdstuk 4). Deze symmetrie kan verklaard worden met behulp van een kleine gradint in de elektronendichtheid. Deze gradint is in feite een inhomogeniteit op een lengteschaal groter dan lengte van het preparaat zelf. In sommige preparaten kan de dichtheidsgradint gecontroleerd worden door de gelijktijdige meting van de Hall weerstand aan twee paar potentiaal-contacten, in combinatie met gepulste belichting bij lage temperatuur. Door de gradint zeer klein te maken wordt een ander aspect van universaliteit aangetoond, nl. de semi-cirkel relatie. We laten zien dat voor een homogeen 2DEG de componenten van de geleidingstensor de semi-cirkel relatie volgen voor alle PP overgangen (dus niet alleen voor de PI overgang zoals vroeger gedacht werd).

Ondanks de belangrijke vorderingen die we geboekt hebben in Hoofdstuk 4 met het begrijpen van inhomogeniteiten, moeten we concluderen dat onze halfgeleiderstructuren niet geschikt zijn voor het meten van correct kritiek gedrag van PP overgangen. Daarom richten we ons in de twee volgende hoofdstukken (Hoofdstukken 5 en 6) op de PI overgang. De analyse van magnetotransportmetingen aan twee verschillende halfgeleiderstructuren laat een correct schalingsgedrag zien, met vrijwel dezelfde waarde voor de kritieke exponenten. De gemeten kritieke waarde $\kappa \approx 0.58$ is aanzienlijk groter dan de Fermi-vloeistof waarde $\kappa = 0.42$, hetgeen suggereert dat Coulomb wisselwerking een belangrijke rol speelt in de heeltallig quantum Hall faseovergangen. Het preparaat waaraan wij gemeten hebben en waarvan de resultaten beschreven worden in Hoofdstuk 5, is hetzelfde als dat in de allereerste publicatie over schaling van het QHE van Wei *et al.* In dit werk werd $\kappa \approx 0.42$ bepaald voor de PP overgangen. Met de nieuwe gegevens voor de PI overgang kunnen we nu met zekerheid stellen dat de "universele" waarde gerapporteerd door Wei *et al.* grotendeels het resultaat is van preparaatinhomogeniteiten en derhalve geen correct schaalgedrag weergeeft. In Hoofdstuk 6 worden transportmetingen beschreven aan een preparaat waarvan de ladingsdragersdichtheid n_e gevarieerd kan worden. Het blijkt dat de kritieke exponent κ praktisch niet af hangt van de dichtheid n_e. De geringe toename van κ met n_e kan toegeschreven worden aan een toenemende overlap van de Landau levels bij lagere dichtheden. In Hoofdstuk 6 presenteren we ook een nieuwe methode om schaling zichtbaar te maken. Deze methode heeft een aantal voordelen t.o.v. de traditionele methode.

Een belangrijk onderdeel van dit proefschrift wordt gevormd door numerieke simulaties van de invloed van preparaatinhomogeniteiten op de transporteigenschappen. Dit is het onderwerp van Hoofdstuk 7. Aannemende dat κ universeel is voor de lokale weerstandstensor en dat de gradint van de ladingsdragersdichtheid constant is, rekenen we de vierpunts weerstand uit voor verschillende temperaturen, vulfactoren en dichtheidsgradinten (zowel wat richting als grootte betreft). De resultaten van onze simulaties zijn in goede kwalitatieve overeenstemming met de experimenten. Inhomogeniteiten hebben een sterke invloed op de breedte van de PP overgangen bij lage temperatuur, hetgeen resulteert in een te lage waarde van de kritische exponent κ. Onze simulaties reproduceren en verklaren ook de tot nu toe niet goed begrepen temperatuurafhankelijkheid van het maximum van de longitudinale weerstand. Ook bevestigen we dat de PI overgang robuust is en ongevoelig voor kleine gradinten in de ladingsdragersdichtheid.

Acknowledgements

Many people have contributed directly or indirectly to the completion of this thesis. Without having the option of including all of them as co-authors, I would at least like to use the last pages of this book to express my gratitude to those who contributed most.

I am sincerely indebted to my co-promotor Anne de Visser for revealing to me the magic of low-temperature physics, his daily guidance and support, and his careful reading and intensive correction of this thesis. Anne, it was a big pleasure to be part of your group for the last five years. I would like to thank my promotor Aad Pruisken for his valuable theoretical contributions and for teaching me the basics of scaling theory. Perhaps our meetings weren't always easy-going, but the salt and pepper in our discussions added much spice and flavor to my memories about them. I am very grateful to my colleague, friend and "brother in arms" Dennis de Lang, who was always around from the first to the last day of my Ph.D., ready to help, teach, and share my joys and problems. Dennis, it was a great pleasure to be on the road with you to exotic places such as Corsica, Nara, Oxford and Grenoble.

Significant part of the experimental work was carried out outside of the Van der Waals - Zeeman Institute. I owe much gratitude to Uli Zeitler, Stef Olsthoorn, Cecilia Possanzini, Kostya Novoselov and Jaan-Kees Maan for their valuable help during the series of experiments at the High Field Magnet Laboratory in Nijmegen. Success of our experiments in Grenoble would not have been possible without the help and guidance of Duncan Maude and Louis Jansen. And, of course, nothing could be done without samples that were generously given to us by G.B.Galiev, H. Kunzel, B.N.Zvonkov and P.Nouwens.

Many thanks to Paul Koenraad from the Technical University of Eindhoven and to Vladimir Kulbachinskii from Moscow State University for sharing with me their practical knowledge and experience of two-dimensional semiconductor systems. I've also learned a lot from our visitors Biswajit Karmakar, Vladimir Neverov and Takashi Naka. Special thanks to all technicians from the mechanical and electronic workshop, which were always ready to help solve

numerous problems: H. Beukers, J. Overtoom, E. Baaij, B. Zwart, P. Sannes. I am grateful to J. Klaasse for his participation in the experiments with the 17 T magnet. Many thanks to Marc Brugman for his quick reactions to my computer related demands and to Mariet Bos and Rita Vinig for all the paper work they have done to make my life easier.

I'll never forget the pleasant atmosphere of the WZI created by all staff members and PhD students. Joost, Jeroen, Jaime, Pedro, Manuel, Macek, Michel, Yuri, Mark, Lian, you left the institute earlier than I did, but I still remember all of you. Gianni, Tracy, Huy, Stan, Sara, Asmae, Alessia, Vlad, pleasant memories about you I take to Manchester. Mark, Jeroen, Tom, Ekkes, Gerard, you are the "skeleton" of this institute and I very much like the way it is.

Life in Amsterdam does not stop outside of the WZI. My dear friends Jorge, Miriam, Nacho, Salvo, Ruben, Maria, Annemarieke, Jordi, Diego, Timi, Aki, Viney, Misha, Manu, Juan, Javier, Silke, Paulina, Silva, Rocio, Laura, Simone, Thai, Nelson and Damian your role in this thesis is much bigger that it seems. Many thanks to my Russian-speaking friends from Nijmegen: Igor, Masha, Vadik and Olya for warm welcome whenever I visited HFML.

I am grateful to my friends from Moscow, who kept in touch with me all these years, especially to Misha Mikheev, Ira Koteiko and Yurko Koshelyuk.

I cannot describe in words how much I adore two wonderful women, my mama Nelli Ponomarenko and my wife Lilia, for their love, support, inspiration, faith and patience. I love you.

I love you all, guys.